Doctoral Dissertation

THE DEVELOPMENT OF HIGH-PERFORMANCE NON-PRECIOUS-METAL ELECTRODES/CATALYSTS FOR HYDROGEN-RELATED AND ENERGY STORAGE DEVICES

Chaehyun Lim

Department of Energy Engineering

(Energy Engineering)

Graduate School of UNIST

2020

THE DEVELOPMENT OF HIGH-PERFORMANCE NON-PRECIOUS-METAL ELECTRODES/CATALYSTS FOR HYDROGEN-RELATED AND ENERGY STORAGE DEVICES

Chaehyun Lim

Department of Energy Engineering

(Energy Engineering)

Graduate School of UNIST

THE DEVELOPMENT OF HIGH-PERFORMANCE NON-PRECIOUS-METAL ELECTRODES/CATALYSTS FOR HYDROGEN-RELATED AND ENERGY STORAGE DEVICES

A dissertation
submitted to the Graduate School of UNIST
in partial fulfillment of the
requirements for the degree of
Doctor of Philosophy

Chaehyun Lim

11/22/2019

Approved by

Advisor
Guntae Kim

THE DEVELOPMENT OF HIGH-PERFORMANCE NON-PRECIOUS-METAL ELECTRODES/CATALYSTS FOR HYDROGEN-RELATED AND ENERGY STORAGE DEVICES

Chaehyun Lim

This certifies that the dissertation of Chaehyun Lim is approved.

11/22/2019

signature

Advisor: Guntae Kim

signature

Jong-Beom Baek

signature

Hu Young Jeong

signature

Ikwhang Chang

signature

Sihyuk Choi

Abstract

Various clean and renewable energy devices/sources such as solar cells, wind power, geothermal, and tidal power have been suggested to solve global warming and energy depletion. Among suggested energy sources, hydrogen energy is considered as a promising alternative to replace conventional combustion systems due to its feasibility and sustainability. Moreover, the hydrogen can act as a clean and efficient energy source as well as an energy carrier which can save the energy from renewable energy sources. The most hydrogen devices work with several electrochemical reactions including oxygen reduction reaction (ORR), oxygen evolution reaction, (OER), hydrogen oxidation reaction (HOR), and hydrogen evolution reaction (HER). The development of effective electrochemical catalysts is required because those electrochemical reactions have a slow reaction rate. Therefore, I focus on the development of hydrogen-related catalysts and electrodes having outstanding and robust electrical, electrochemical and thermal properties to properly demonstrate various hydrogen-related energy devices, in this study. Moreover, I introduce several researching achievements with fundamental knowledge including operating principles and theoretical backgrounds as presented as follows.

1. Materials for Energy conversion device (cathode of the solid oxide fuel cell)

- Influence of Ca-doping in layered perovskite $PrBaCo_2O_{5+\delta}$ on the phase transition and cathodic performance of a solid oxide fuel cell
- Investigation of the Fe doping effect on the B-site of the layered perovskite $PrBa_{0.8}Ca_{0.2}Co_2O_{5+\delta}$ for a promising cathode material of the intermediate temperature solid oxide fuel cells
- Ca and Ni-doped $Pr_{0.5}Ba_{0.5}FeO_{3-\delta}$ as a highly active and robust cathode for high-temperature solid oxide fuel cell

2. A catalyst for energy storage devices: Nano-perovskite oxide prepared via inverse microemulsion mediated synthesis for the catalyst of lithium-air batteries

Context

List of Figures

List of Tables

Chapter 1. General introduction

1.1 Motivation and Research topic

As an increased global population and progressed industrialization, energy consumption and environmental contamination have been rapidly increased day by day, and it is assumed that a million terajoules of energy are consumed every day. Over the past century, more than half of the energy has been supplied by fossil fuel which accompanies severe air pollution emission gas including green-house gases -mainly carbon dioxide (CO_2). As shown in Fig. 1-1, the atmospheric CO_2 concentration has been continuously increased over the past years and is expected to rapidly increase in the future.

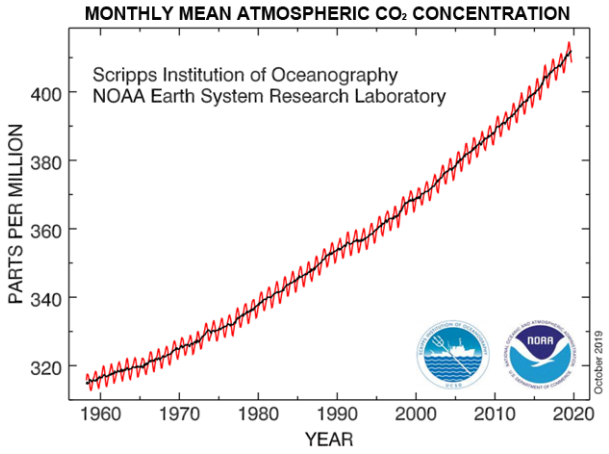

Fig. 1-1. Global monthly atmospheric CO_2 concentration change (Source: National Oceanic and Atmospheric Administration, NOAA)

In order to suppress the CO_2 emission, significant efforts should be made from the individual level to the international level. A representative effort at an international level is the Paris Climate Agreement, which promises to phase out fossil fuels by 2050. The long-term goal of the Paris Climate Agreement is to keep the temperature increase in global average temperature to well below 2 ^{o}C above pre-industrial levels. The CO_2 emission is mandatory to support human activity, thus, the main solution to compensate for the CO_2 emission is the development of clean and renewable energy systems. Among various clean

and renewable systems, the hydrogen energy system has been received much attention due to its cleanness, abundance, and efficiency. The hydrogen energy system efficiently operates using the electrochemical reaction with hydrogen, oxygen, and water. Herein, several electrodes and catalysts were studied and investigated for electrochemical and thermal devices for hydrogen including solid oxide fuel cell (conversion), metal-air battery (electrical energy storage), dry reforming of methane (generation), and metal-CO_2 system (generation).

1.2 Efficient energy conversion device: Solid oxide fuel cell

1.2.1. Overview

Solid oxide fuel cell (SOFC) is one of the most efficient energy conversion devices which directly converts the chemical energy (fuel) into electrical energy.[1–3] The SOFC provides more than 50 % high efficiency because it SOFC generates electricity electrochemically and is not limited by the Carnot cycle, unlike combustion engines.[4] Moreover, the high operating temperature (> 500 ^{o}C) of the SOFC allows using various fuels such as hydrogen, hydrocarbon, gasified carbon, and carbon mono-oxide directly without additional reforming process.[5] Moreover, electrochemically reacted SOFC emits much less polluting emissions such as NO_x, and SO_x, and CO_2 as compared to the combustion system. In this regard, the SOFCs are well suited for large-scale station system with cogeneration of heat and power due to their unique operating and performance characteristics.

1.2.2. Operating Principle of SOFC

The SOFC consists of 3 main components: a dense electrolyte and 2 porous electrodes exposed to fuel and oxidant (air). Fig. 1-2 illustrates a schematic image for the operating principle of SOFC. During operation, an electrode in the fuel-side (fuel electrode/anode) faces a highly reduced atmosphere, while another electrode is exposed in highly oxidizing conditions. These atmospheres are an important factor closely related to the chemical, structural, and thermal stability in the design of electrodes.

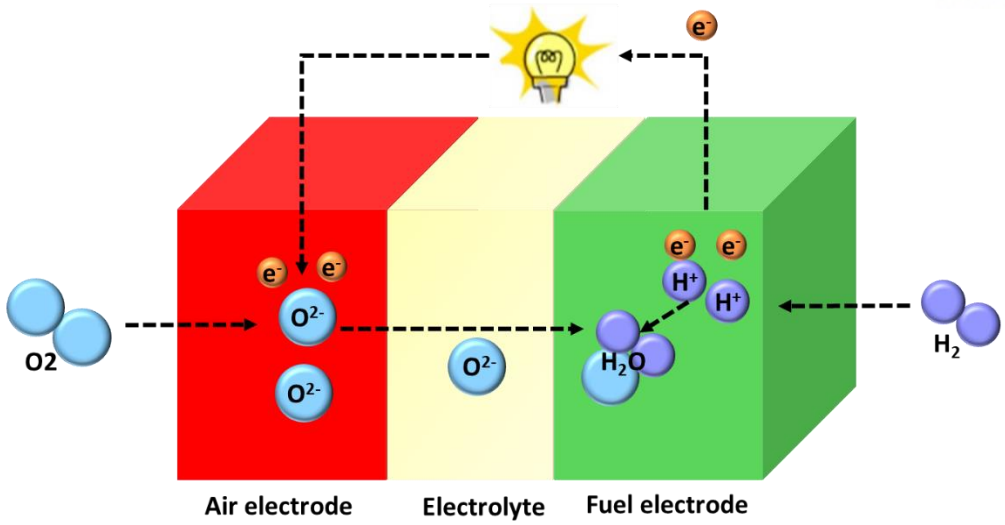

Fig. 1-2. Scheme of operation of SOFC

In the cathode, oxygen reduction reaction (ORR) occurs with electrons from anode to produce oxygen ions as shown in Eq. 1-1 as followed.

$$O_2 + 4e^- \rightarrow 2O^{2-} \quad \text{Eq. 1-1}$$

The generated oxygen ions are then transported to the anode through oxygen ion conductive electrolyte. In the anode, the hydrogen molecule oxidized into protons and electrons by the hydrogen oxidation reaction (HOR), as shown in the followed equation (Eq. 1-2).

$$H_2 \rightarrow 2H^+ + 2e^- \quad \text{Eq. 1-2}$$

And the overall equation of SOFC can be written by the following equation (Eq. 1-3).

$$H_2 + \frac{1}{2}O_2 \rightarrow H_2O \quad \text{Eq. 1-3}$$

The transported oxygen ions from cathode and proton produce the water and flowing electron through an external circuit generates the electricity. As shown in the equations, both ORR and HOR are valid where co-exist of electronic (e^-), ionic (O^{2-}/H^+), and gas phase (O_2/H_2) called triple-phase boundary (TPB). [6–8]

1.2.3. Challenges of SOFCs

The components of SOFCs are composed of ceramic and metal because of its high operating

temperature over 350 ºC.[9] Even though this high operating temperature provides several advantages such as high efficiency, corrosion tolerance, fuel/catalyst selectivity, it also causes several thermal/chemical degradation problems.[10–12] Reducing operating temperature can be a solution to overcome these drawbacks, but lowering temperature leads deteriorate of electrochemical performance by decreasing catalytic activity especially, the oxygen reduction reaction.[13,14]

1.2.4. Theoretical Background

1.2.4.1. Thermodynamics

For the overall reaction of SOFC, the Eq. 1-4 and Eq. 1-5 are given by the 1st and 2nd laws of thermodynamics since the SOFCs convert the Gibbs free enthalpy of the electrochemical reactions directly into electricity. [15] The equation assumes that the reversibility of the transport proves is governed by the 2nd law of thermodynamics.

$$\mathrm{Q} + \mathrm{w} \rightarrow \Delta\mathrm{H} \qquad \text{Eq. 1-4}$$

The molar reaction enthalpy (ΔH) of the oxidation is composed of work and heat energy.

$$\oint \Delta\mathrm{S} = 0 \rightarrow \mathrm{q} = q_{rev} = T\Delta S \qquad \text{Eq. 1-5}$$

The enthalpy can be described by following Eq. 1-6

$$q_{rev} + w_{rev} = \Delta H \qquad \text{Eq. 1-6}$$

, where the reversible heat exchange with the environment equalizes the created reaction entropy. The reaction entropy is a result of the different opportunities of the species to save thermal energy between the absolute zero levels of temperature and the level of temperature of the reactor. Considering the Eq. 1-3 and Eq. 1-4, the molar reversible work (w_{rev})can be calculated as shown in Eq. 1-7.

$$w_{rev} = \Delta H - T\Delta S \qquad \text{Eq. 1-7}$$

With the ambient temperature as a reference for the calculation of the Gibbs free enthalpy (ΔG), the reversible work of the reaction is equal to the Gibbs free enthalpy of the reaction.

$$w_{rev} = \Delta G = \Delta H - T\Delta S \qquad \text{Eq. 1-8}$$

According to the 1st law and the 2nd law of thermodynamics, the energy transfer from one form to

another form can be identified by thermodynamic potentials. An equation of internal energy (U) is based on the variation of 2 independent variables of entropy S and volume V, based on the 1st law and 2nd law of thermodynamic

$$dU = T\,dS - p\,dV \qquad \text{Eq. 1-9}$$

, where p is the pressure and T is temperature. $T\,dS$ represents the reversible heat transfer and $p\,dV$ is the mechanical work. The relation between dependent variables (T and p) with variations in the independent variables is shown in the following equation (Eq. 1-10 and 1-11).

$$\left(\frac{dU}{dS}\right)_v = T \qquad \text{Eq. 1-10}$$

$$\left(\frac{dU}{dS}\right)_s = -p \qquad \text{Eq. 1-11}$$

A conversion of U using the Legendre transformation defines a thermodynamic potential G (T, p) as follows.

$$G = U - \left(\frac{dU}{dS}\right)_v S - \left(\frac{dU}{dS}\right)_s V \qquad \text{Eq. 1-12}$$

From Eq. 1-10 and 1-11, Eq. 1-13 can be obtained as followed.

$$G = U - TS - pV \qquad \text{Eq. 1-13}$$

The Variation of G becomes as followed.

$$dG = dU - T\,dS - S\,dT + p\,dV - V\,dp \qquad \text{Eq. 1-14}$$

With the Eq 1-9, it can be changed.

$$dG = -S\,dT - V\,dp \qquad \text{Eq. 1-15}$$

The new thermodynamic potential (enthalpy, H) can be defined as

$$H = -U - \left(\frac{dU}{dS}\right)_v \qquad \text{Eq. 1-16}$$

From Eq. 1-5

$$H = U + pV \qquad \text{Eq. 1-17}$$

H can be re-written as a function of S and p

$$dH = dU + p\,dV + V\,dp \qquad \text{Eq. 1-18}$$

$$dH = T\,dS + V\,dp \qquad \text{Eq. 1-19}$$

For the overall reaction of SOFC (Eq. 1-3), the difference of Gibbs free energy (ΔG) is written as

$$\Delta G = \Delta G_{H_2O} - \Delta G_{H_2} - \frac{1}{2}\Delta G_{H_2} \quad \text{Eq. 1-20}$$

If all Gibbs free energy is consumed to electrical work

$$\Delta G = -nFE \quad \text{Eq. 1-21}$$

, where n and F represent the number of participated electrons in the chemical reaction and the Faraday constant, respectively. Assumed that the reactant and products are all in the standard conditions, the reversible standard potential (E^0) of the electrochemical reaction is defined following equation (Eq. 1-22).

$$E^0 = -\frac{\Delta G^0}{nF} \quad \text{Eq. 1-22}$$

Since the Gibbs free energy is dependent on the temperature, the equation can be changed by this.

$$\Delta G = \Delta H - T\,\Delta S \quad \text{Eq. 1-23}$$

Adopting standard values of T (273.15K) and p (1atm)

$$E^0 = \frac{237900\ J \cdot mol^{-1}}{2 \times 96485\ C \cdot mol^{-1}} = 1.23\ V \quad \text{Eq. 1-24}$$

The theoretical reversible potential (E) is derived from the Nernst equation (Eq. 1-25)

$$E = E^0 - \left(\frac{RT}{2F}\right) \ln\left(\frac{p_{H_2O}}{p_{H_2} \cdot p_{O_2}^{\frac{1}{2}}}\right) \quad \text{Eq. 1-25}$$

, where R is the ideal gas constant, T is the absolute temperature, p is the partial pressure of each gas.

transported oxygen ions from cathode and proton produce the water and flowing electron through an external circuit generates the electricity. As shown in the equations, both ORR and HOR are valid where co-exist

1.2.4.2. Electrochemistry

The electrochemical activity of SOFC reflects in the current-voltage (i-V) curves. The typical i-V curve of fuel cells is illustrated in Fig. 1-3. An ideal can supply any current with constant voltages which are determined by thermodynamics. However, in the real fuel cells, the actual voltage is much less than the

ideal fuel cell.[16] The difference between ideal voltage and the actual voltage is caused by several factors; (1) the lower open-circuit voltage compared to the theoretical value, (2) the rapid initial drop in voltage by activation polarization (activation loss), (3) the slow and linear voltage drop in the intermediate current region, which originates from ohmic resistance (ohmic resistance loss), and (4) the fast voltage drop at higher current density attributed to insufficient gas feeding (concentration loss).

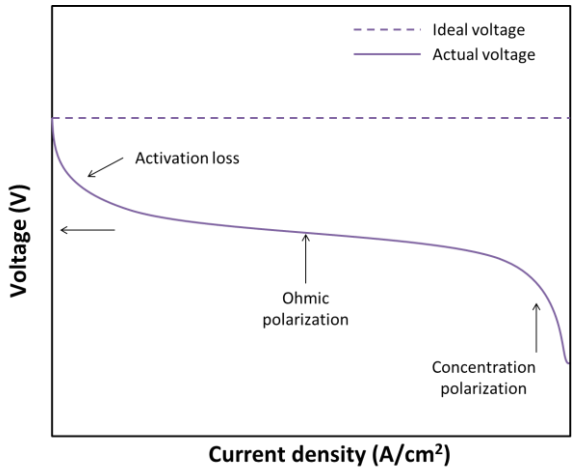

Fig. 1-3. Ideal and actual voltage trend of a fuel cell

The total polarization in the fuel cell can be express as followed equation

$$\eta_{total} = \eta_{act} + \eta_{ohmic} + \eta_{conc} \qquad \text{Eq. 1-26}$$

, where η_{total} is total polarization, η_{act} is activation polarization, η_{ohmic} is total polarization, and η_{conc} is concentration polarization.[17]

1. Kinetics of the electrochemical reaction (activation polarization, η_{act})

The activation polarization is related to the charge transfer reaction, which is directly associated with the rate-determining step. The activation polarization is considered as the over-potential consumed to the activation energy for the reaction at the electrode. The correlation between current density and activation polarization is expressed by the Butler-Vomer equation.

$$i = i_0 \left[\exp\left(\frac{(1-\alpha)nF\eta_{act}}{RT}\right) - \exp\left(\frac{-\alpha nF\eta_{act}}{RT}\right)\right] \qquad \text{Eq. 1-27}$$

The large η can make one of the bracketed terms in Eq. 1-27 negligible, so the equation can be changed as the Tafel equation (Eq. 1-28).

$$\eta_{act} = a \pm blogi = (a_A + b_A lnj) + (a_C + b_C lnj) \quad \text{Eq. 1-28}$$

Parameters a and b are constants related to the applied electrode materials, type of electrode reaction, and temperature.

2. Internal electrical and ionic resistance (ohmic polarization, η_{ohmic})

Major ohmic losses are attributed to impedance to the flows of ions in the electrolyte and electrons at the electrodes. So, the ohmic losses can be reduced by decreasing the electrode separation and ionic resistance of electrolyte.

$$\eta_{ohmic} = jASR_{ohmic} \quad \text{Eq. 1-29}$$

3. Limitations in mass transport (concentration polarization)

The potential is dropped faster at the higher current density because the consuming reactants at the electrode by the electrochemical reaction is much faster than supply. There are some processes with may contribute to these imbalanced reactants supply; 1) diffusion of the gas phases and products through pores of electrodes, 2) surface exchange including adsorption of the fuel/oxidant gas and desorption of the products (mostly water), 3) diffusion of reactants and products into the electrochemical reaction through the electrolyte. At practical current densities, slow transport of reactants and products to and from electrochemical reaction sites is a major contribution to concentration polarization.

$$\eta_{conc} = c\ ln\frac{j_L}{j_L - j} \quad \text{Eq. 1-30}$$

In this regard, the total polarization in the fuel cell can be a sum of these three polarizations as followed equation

$$E = E_{th} - (a_A + b_A lnj) - (a_C + b_C\ lnj) - (j\ ASR_{ohmic}) - (c\ ln\frac{j_L}{j_L - j}) \quad \text{Eq. 1-31}$$

1.3. Large scale energy storage device: Metal-air batteries (MABs)

1.3.1. Overview

Since the interest for renewable energy has been increased in recent, the requirement for large scale energy storage system has been increased. The metal-air batteries have been received much attention due to their extremely high theoretical energy densities as compared with other storage systems as shown in Fig. 1-4.[18]

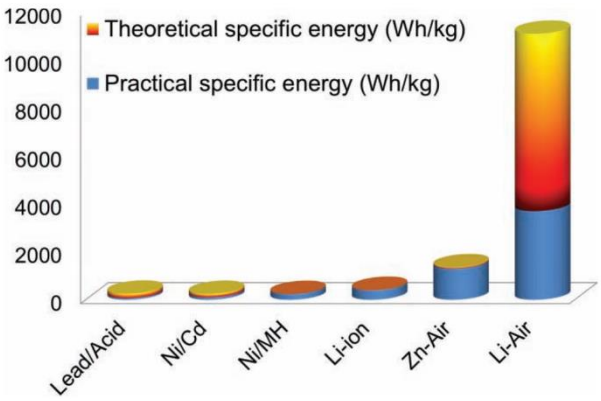

Fig. 1-4. Theoretical densities of various energy storage systems

While conventional secondary battery systems have limited energy density by saving reagents in the cell, the metal-air batteries extend energy density using oxygen (O_2) in the atmosphere as a cathode. The rechargeable metal-air batteries can be used in various electronic devices which need large scale energy such as electrical vehicles, fixed storage, and defense industries due to extremely higher specific energy (energy per unit weight). For example, the theoretical specific energies of aqueous and non-aqueous Li-air batteries are 3582 Wh kg^{-1} and 3505 Wh kg^{-1}, respectively, which are approximately 9 times larger than of Li-ion battery (387 Wh kg^{-1}). [18–24] In general, there are 3 major components of MABs; a metal anode, an electrolyte (aqueous, organic, and/or solid), an air electrode (cathode). The various metals such as Li, Na, Mg, Al, Ca, Fe, Zn, and their alloys can be considered as suitable candidates. Among them, the Li (Li-air batteries) and Zn (Zn-air batteries) have received attention. The basic reaction of anode for these two MABs can be written, respectively,

$$2\mathrm{Li} + O_2 \leftrightarrow Li_2O_2 \qquad \text{Eq. 1-32}$$

$$2\mathrm{Zn} + O_2 \leftrightarrow 2ZnO \qquad \text{Eq. 1-33}$$

Regardless of kinds of electrolytes and configuration of MABs, two important electrochemical reactions at the cathode are issued for MABs; oxygen reduction reaction (ORR) for discharge process and oxygen evolution reaction (OER) for charge process.

In alkaline media, ORR is used at the cathode for the discharge process

$$O_2 + 2H_2O + 4e^- \rightarrow 4OH^- \qquad \text{Eq. 1-34}$$

On the contrary, the OER occurs at the cathode during charge

$$4OH^- \rightarrow O_2 + 2H_2O + 4e^- \qquad \text{Eq. 1-35}$$

The sluggish kinetics of these reactions lead to a limited practical specific energy of MABs. In order to solve this problem, it is necessary to use a highly active catalyst to accelerate the rate of the process. Precious metal-based catalysts have been generally used because of their fast catalytic activity, but they are difficult to use widely due to their mono-functionality and high cost. Therefore, considering the cost and bifunctionality of (ORR) and charge (OER), the development of inexpensive and bifunctional catalyst is required.

1.3.2. Theoretical background

1.3.2.1. Cyclic voltammetry (CV)

Cyclic voltammetry (CV) is a general technique for studying the properties of electrochemical systems, in which a current output is recorded with the corresponding applied periodic linear potential sweep. Several kinds of information can be obtained by analyzing the CV profiles such as 1) the presence of intermediates in a redox reaction, 2) electron transfer kinetics, and 3) the reversibility of a reaction.[25] This reversible reaction is expressed as

$$O_x + ne^- \leftrightarrow Red \qquad \text{Eq. 1-36}$$

The diffusion equation can be solved under a linear voltage sweep condition to give a relationship between peak current (i_p) and diffusion constant (D)

$$i_p = 0.4463F(\frac{F}{RT})^{\frac{1}{2}}C^*\nu^{\frac{1}{2}}AD^{\frac{1}{2}} \qquad \text{Eq. 1-37}$$

, where i_p is the peak current density in ampere, F is the Faraday constant, C^* is the initial concentration in mol cm^{-3}, ν is scan rate in V s^{-1}, A is electrode area in cm^2, and D is the diffusion constant in cm^2 s^{-1}. The concentration of the unknown solution can be determined by generating a calibration curve of current versus concentration because the concentration is propositional to the current in a reverse system.

1.3.2.2. Tafel slope

In order to compare the electrocatalytic activity and to reveal the reaction mechanism of the electrocatalyst, Tafel analysis is generally used. This analysis method provides information about related rate-determination step by evaluation of the sensitivity of the current response to the applied potential. The experimentally obtained Tafel slope is considered to be compared to the theoretically derived one assuming different rate-determining steps based on the kinetics model. To simplify the derivation process, the surface coverage of the intermediate species is assumed as constant either $\theta \approx 0$ or $\theta \approx 1$.[26]

1.4. Efficient electrode materials and catalysts

1.4.1 Perovskite (ABO_3)

Most ABO3-type perovskite oxides form a closely related structure of CaTiO3 perovskite.

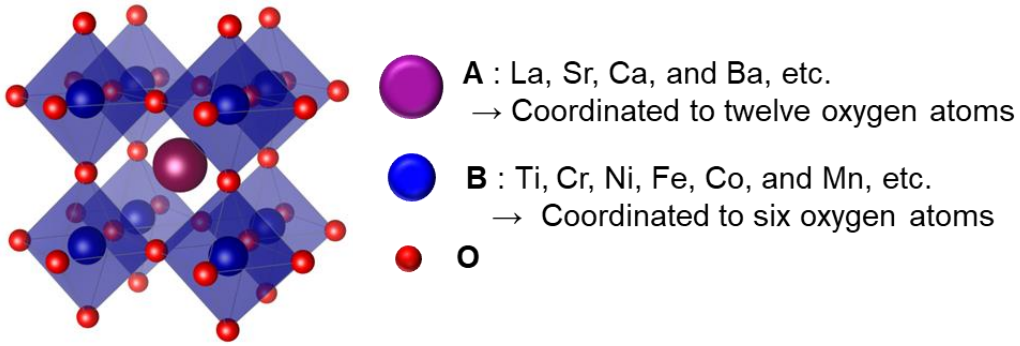

Fig. 1-5. Unit-cell of perovskite oxide

These materials are capable of adopting a wide range type and amount of cation because of their flexible structure. The unit cell of the perovskite structure is presented in Fig. 1-8. The ideal structure of perovskite without defects can be described as the cubic stacking (ABC) sequence with all BO6 octahedral sharing corners within the ccc(=3C) framework, where c refers to the cubic layer.[27] A-site cations of perovskite consist of the larger cation with 12-fold oxygen coordination while B-site cations are the smaller size with 6-fold oxygen coordination. The oxygen anions are linked to six cations (4A + 2B). The ionic radiuses of the A/B-site cations are known to play an important role in determining crystal structure, which called "Goldschmidt tolerance factor (*t*)".[13,28] This factor represents the deviation of the perovskite from the ideal cubic symmetry. The *t* is defined as

$$t = \frac{(r_A + r_O)}{\sqrt{2}(r_B + r_O)} \qquad \text{Eq. 1-40}$$

, where r_A, r_B, and r_O are the mean ionic radii of A, B, and O ions, respectively.

1.4.2 Cation ordered layered perovskite ($AA`B_2O_{5+\delta}$)

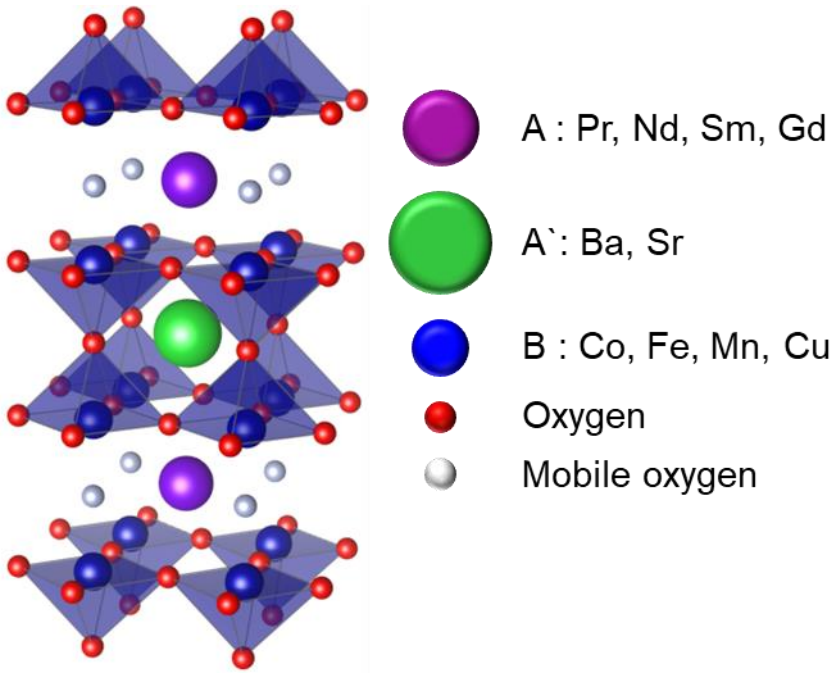

Fig. 1-6. Unit-cell of layered perovskite oxide

The layered perovskite structures have a chemical formula of $AA`B_2O_{5+\delta}$, where A is a trivalent lanthanide (*Ln* = Pr, Nd, Sm, Ho, Gd, and etc.), A` is a relatively large size Ba, and B usually composes with usually transition metal, as described in Fig. 1-9.[10,29-31]

The large ionic radius differences between A and A` facilitates to generate a two-layer alternated stacking sequence of $[BaO][BO_2][LnO_\delta][BO_2]$ along with c-axis with localized excess oxygen ions at the ln-O plane, and excess oxygen ions thereupon provide a disorder-free channel for ion motion that enhances the oxygen ion diffusion.[32] The layered perovskites have received attention due to their excellent chemical diffusivity and superior surface exchange coefficient.

1.5. Nanostructure

1.5.1. Catalyst

Catalysts are materials that do not participate in the reaction but accelerate the chemical reaction by reducing activation energy, as shown in Fig. 1-10. The activation energy (E_a) is a barrier to chemical reactions, and reactants with energy lower than E_a cannot pass through the transition state and cannot become a product. The catalyst may have other intermediates, such as bond relocation, which is needed to convert the reactants into the product, to provide a new pathway with low activation energy.

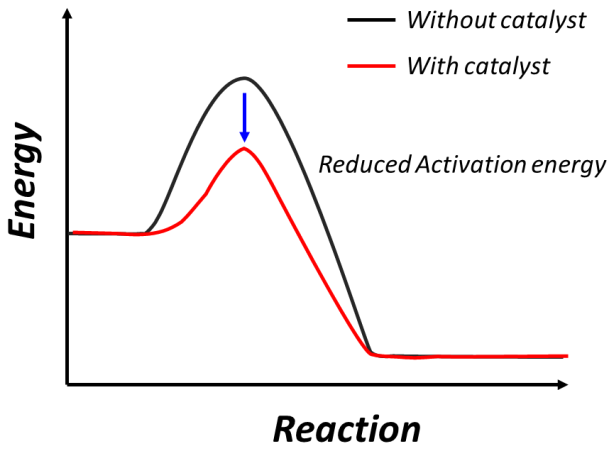

Fig. 1-7. Schematic of energy paths with/without catalyst

1.5.2. Nanostructured catalysts

Nanostructured materials have attracted a great deal of attention for electrochemical energy devices due to their unique mechanical, electrical, electrochemical, and optical properties imparted by confining the dimensions. Nanoscience is a universally adopted strategy for material research because it understands the physical and chemical processes at the most fundamental level. Thus, many researchers have developed the synthesis and analyzed the properties in order to appreciate the advantages and disadvantages of the nanomaterials. [7,39-42]

Advantages;

Nanoparticles less than 10 nm in diameter have high potential in areas such as sensors nanoelectronics, catalysts, and optics. The catalytic activity of nanoparticles is affected by their size. Thus, the relative proportions of surface atomic types change dramatically with various particles size. In many cases, the beneficial change in the electronic properties of the surface atoms that are predominantly located at the corners and corners of the small particles increase their activity as the particle size decreases. On the other hand, the reactivity and selectivity of metal nanocatalysts are highly dependent on the different crystallographic planes present on the nanoparticles and can be achieved by controlling the morphology of these nanoparticles. The size and surface of nanocatalysts play an important role due to their selectivity and responsiveness.

Disadvantages:

In principle, the study for nanomaterials must help to improve and optimize the system under investigation. But despite these fundamental advances, nanotechnology is facing two problems.

1. The properties of materials changes as they scale up as they are reduced to the nanoscale. In particular, the level of control that can act at the nanoscale or single object level tends to be weaker on the medium and macroscopic scale or when handling large numbers of objects.

2. the industry is reluctant to invest money in developing new large-scale processes for manufacturing

nanomaterials unless it is guaranteed a profitable profit.

1.5.3. Microemulsion

The efforts to construct nanostructures have been widely studied for a long time. The way of wet chemistry is one of the famous methods of synthesis nanoparticles because mixed cations in the atomic level decrease the synthesis temperature and time by increasing reactivity. The microemulsion method is one of the wet chemistry methods to construct nano-structure using dispersity of precursors by proper surfactant. [43]

The emulsion consists of 3 major parts, an aqueous phase, an oil phase, and an amphipathic surfactant. The major oil or aqueous phase surrounding minor phase using a surfactant. Constructing nanostructure by emulsion is performed as followed description and Fig. 1-11.

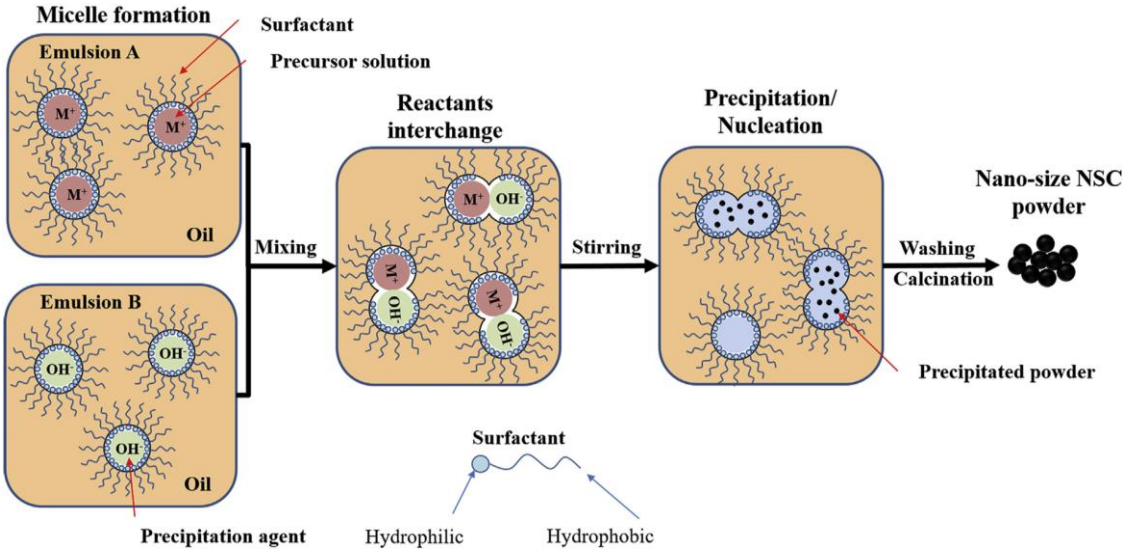

Fig. 1-8. Schematic of microemulsion (water-in-oil)

The cation is dissolved into a minor phase (in this case aqueous part). The hydrophilic part of the amphipathic surfactant surrounds the aqueous solution and the hydrophobic part combines with the oil phase to form spherical micelles. [44,45] Since these micelles act as nano-size reactors and the precipitation reaction occurs only in the micelles. The primary particle size is limited by the size of the

micelles. Because charged micelles (depend on surfactant and micelles) increases the distance between micelles by repulsive force between micelles, further inhibiting direct contact between precursor droplets.[46] Due to these limited sizes and increased distance of precursor droplets, the primary particle size should be reduced.

References

[1] N. Q. Minh, C. Singhal, and M. Williams, *ECS Transactions*, **17** (2009) 211-219.

[2] S. Yoo, A. Jun, Y. -W. Ju, D. Odkhuu, J. Hyodo, H. Y. Jeong, N. Park, J. Shin, T. Ishihara, and G. Kim, *Angew*. *Chemie. Int*. *Ed*., **53** (2014) 13064-13067.

[3] S. Sengodan, S. Choi, A. Jun, T. H. Shin, Y. -W. Ju, H. Y. Jeong, J. Shin, J. T. S. Irvine, and G. Kim, *Nat. Mater*.,**14** (2014) 205-209.

[4] R. J. Gorte and J. M. Vohs, *J. Catal*, **216** (2003) 477-486.

[5] N. Q. Minh, *Solid State Ionics*, **174** (2004) 271-277.

[6] J. Nielsen and T. Jacobsen, *Solid State Ionics*, **179** (2008) 1314-1319.

[7] S. Kim, A. Jun, O. Kwon, J. Kim, S. Yoo, H. Y. Jeong, J. Shin, and G. Kim, *ChemSusChem*, **8** (2015) 3153-3158.

[8] J. Kim, W. Seo, J. Shin, M. Liu, and G. Kim, *J. Mater. Chem. A.*, **1** (2013) 515-519.

[9] T. Hibino, A. Hashimoto, T. Inoue, J. I. Tokuno, S. I. Yoshida, and M. Sano, *Science*, **288** (2000) 2031-2033.

[10] S. Choi, S. Yoo, J. Kim, S. Park, A. Jun, S. Sengodan, J. Kim, J. Shin, H. Y. Jeong, Y. Choi, G. Kim, and M. Liu, *Sci. Rep*., **3** (2013) 2426.

[11] A. Jun, S. Yoo, O. Gwon, J. Shin, and G. Kim, *Electrochim. Acta*., **89** (2013) 372-376.

[12] C. Kim, J. Kim, J. Shin, and G. Kim, *Int. J. Hydrogen Energy*., **39** (2014) 20812-20818.

[13] J. Kim, A. Jun, J. Shin, and G. Kim, *J. Am. Ceram. Soc*., **97** (2014) 651-656.

[14] S. Yoo, T. -H. Lim, J. Shin, and G. Kim, *J. Power Sources*., **226** (2012) 1-7.

[15] S. Sengodan, S. Ahn, J. Shin, and G. Kim, *Solid State Ionics*., **228** (2012) 25-31.

[16] R. P. O'Hayre, F. B. Prinz, S. -W. Cha, and W. Colella, Fuelcell Fundamentals, Wiley. 2nd edition (2008).

[17] N. Q. Minh and T. Takahashi, Electrical conduction in ceramics, Sci. Technol. Ceram. Fuel Cells, (1995) 41-68.

[18] J. Lee, S. T. Kim, R. Cao, N. Choi, M. Liu, and K. T. Lee, *Adv. Energy Mater.*, **1** (2011) 34-50.

[19] F. Cheng and J. Chen, *Chem. Soc. Rev*., **41** (2012) 2172-2192.

[20] G. Girishkumar, B. McCloskey, A. C. Luntz, S. Swanson, and W. Wilcke, *J. Phys. Chem. Lett.*, **1** (2010) 2193-2203.

[21] K. M. Abraham and Z. Jiang, *J. Electrochem. Soc.*, **143** (1996) 15.

[22] B. Kumar, J. Kumar, R. Leese, J. P. Fellner, S. J. Rodrigues, and K. M. Abraham, *J. Electrochem. Soc*., **157** (2010) A50-A54.

[23] W. G. Hardin, D. A. Slanac, X. Wang, S. Dai, K. P. Johnston, and K. J. Stevenson, *J. Phys. Chem. Lett*., **4** (2013) 1254-1259.

[24] Y. Li, M. Gong, Y. Liang, J. Feng, J. E. Kim, H. Wang, G. Hong, B. Zhang, and H. Dai, *Nat. Commun*., **4** (2013) 1-7.

[25] K. Lee, L. Zhang, H. Lui, R. Hui, Z. Shi, and J. Zhang, *Electrochim. Acta*., **54** (2009) 4704-4711.

[26] S. Kim, O. Kwon, C. Kim, O. Gwon, H. Y. Jeong, K. H. Kim, J. Shin, and G. Kim, *Adv. Mater. Interfaces*. **5** (2018) 1-9.

[27] T. Ishihara, Perovskite Oxide for Solid Oxide Fuel Cells, Springer, 2009.

[28] T. Sato, S. Takagi, S. Deledda, B. C. Hauback, and S. I. Orimo, *Sci. Rep.*, **6** (2016) 1-10.

[29] A. A. Taskin, A. N. Lavrov, and Y. Ando, *Appl. Phys. Lett.*, **86** (2005) 1-3.

[30] G. Kim, S. Wang, A. J. Jacobson, L. Reimus, P. Brodersen, and C. A. Mims, *J. Mater. Chem.*, **17** (2007) 2500-2505.

[31] S. Yoo, J. Shin, and G. Kim, *J. Mater. Chem*., **21** (2011) 439-443.

[32] C. Lim, A. Jun, H. Jo, K. M. Ok, J. Shin, Y. -W. Ju, and G. Kim, *J. Mater. Chem. A.* (2016) 6479-6486.

[33] J. Guo, H. Lou, H. Zhao, D. Chai, and X. Zheng, *Appl. Catal. A Gen.*, **273** (2004) 75-82.

[34] J. H. Montoya, C. Tsai, A. Vojvodic, and J. K. Nørskov, *ChemSusChem,* **8** (2015) 2180-2186.

[35] A. J. Medford, A. Vojvodic, J. S. Hummelshøj, J. Voss, F. Abild-Pedersen, F. Studt, T. Bligaard, A. Nilsson, and J. K. Nørskov, *J. Catal.*, **328** (2015) 36-42.

[36] H. Ezaki, M. Morinaga, and S. Watanabe, *Electrochim. Acta*, **38** (1993) 557-564.

[37] E. Navarro-Flores, Z. Chong, and S. Omanovic, *J. Mol. Catal. A: Chem.*, **226** (2005) 179-197.

[38] C. Fan, D. L. Piron, A. Sleb, and P. Paradis, *J. Electrochem. Soc.*, **141** (2006) 382-387.

[39] Z. Jiang, C. Xia, and F. Chen, *Electrochimica Acta*, **55**, 2010, 3595-3605.

[40] K. D. Yang, C. W. Lee, J. H. Jang, T. R. Ha, and K. T. Nam, *Nanotechnology*, **28**, 2017 352001.

[41] D. Neagu, G. Tsekouras, D. N. Miller, H. Menard, J. T. S. Irvine, *Nat. Chem.*, 5, 2013, 916-923.

[42] S. P. Jiang, *Int. J. Hydrogen Energy*, **37**, 2012, 449-470.

[43] C. Lim, C. Kim, O. Gwon, H. Y. Jeong, H. K. Song, Y. -W. Ju, J. Shin, and G. Kim, *Electrochimica Acta*, **275**, 2018, 248-255.

[44] W. H. Wu and D. H. Chen, *J. Colloid Interface Sci*, **273**, 2004, 165-169.

[45] H. Watarai, *Chem. Lett*. **20**, 1991, 391-394.

[46] A. K. Ganguli, T. Ahmad, S. Vaidya, and J. Ahmed, *Pure Appl. Nanoparticles*, *80*, 2008, 2451-2477.

Chapter 2. Energy conversion (1): Influence of Ca-doping in layered perovskite $PrBaCo_2O_{5+\delta}$ on the phase transition and cathodic performance of a solid oxide fuel cell

2.1. Introduction

Solid oxide fuel cells (SOFCs) are prospective energy devices that convert chemical energy to electricity with low carbon emissions, high efficiency, and long-term stability in a wide range of fuels. Conventional SOFCs at high operating temperatures (~1273 K), however, suffer from considerable problems, such as thermal stress from thermal expansion coefficient (TEC) mismatch and chemical instability from undesirable reactions between the electrode and electrolyte. Due to these reasons, many researchers have attempted to decrease the operating temperature in an intermediate-range (773–973 K) for providing long-term stability and reducing the costs of components. Decreasing the operating temperature, on the other hand, leads to serious problems associated with a decrease of the electro-catalytic activity for the oxygen reduction reaction (ORR) over the cathode.[1] In this respect, intensive efforts have been devoted to developing alternative cathode materials that can achieve superior and stable electrochemical performance at lower temperatures. Mixed ionic and electronic conductors (MIECs) have been introduced as cathode materials because extended reaction sites can be achieved at not only the triple-phase boundary (gas, ionic conductor, and electronic conductor) but also at the two-phase boundary (electrode and gas phase).[2,3] Among them, cobalt and/or iron-based simple and layered perovskite MIECs have been proposed as cathode materials for SOFCs due to their excellent electrochemical performance at intermediate temperatures.[4-10] In particular, layered perovskite MIEC oxides have received attention because of their rapid oxygen kinetics such as high oxygen diffusion (D) and surface-exchange coefficients (k), as compared with those of ABO_3-type simple perovskite oxides.[11-13] Generally, the structure of the cation ordered layered perovskite family has a

chemical formula of $AA`B_2O_{5+\delta}$, where A is a trivalent lanthanide (*Ln* = Pr, Nd, Sm, Ho, and Gd), A` is a relatively large size Ba, and B is transition metal ions or a mixture of these ions.[3,12,14-18] The ionic radius difference between large size Ba and relatively smaller size lanthanide generates a two-layer alternating stacking sequence of $[BaO][CoO_2][LnO_\delta][CoO_2]$ along the c-axis with localized excess oxygen ions at the *Ln*-O plane, and localized excess oxygen ions thereupon provide a disorder-free channel for ion motion that enhances the oxygen ion diffusivity.[16,19] Among the various kinds of layered perovskites, cobalt-containing $PrBaCo_2O_{5+\delta}$ exhibits a low area-specific resistance (ASR) and excellent single cell performance.[12,16] Furthermore, it is confirmed that strontium doping into the Ba site of $PrBaCo_2O_{5+\delta}$ enhances the electrical conductivity and the electrochemical properties.[20] However, there are some drawbacks such as redox and chemical instability originating from the formation of a secondary phase, e.g., $BaCO_3$ or $SrCO_3$, from the reaction with CO_2 in the atmosphere and Sr segregation on the surface.[12,21,22] Lee *et al.* reported the effect of a smaller size mismatch between the host and dopant in order to reduce Sr segregation, consequently leading to a more stable cathode surface.[23] Recently, Yoo *et al*. observed enhanced stability and electrochemical performance with the substitution of smaller Ca instead of Sr into the Ba site of $NdBaCo_2O_{5+\delta}$ and first-principles density functional theory (DFT) calculations confirmed these favorable properties according to the thermodynamic behavior of mobile oxygen species.[13]

In this regard, we systematically studied the effect of calcium substitution on Ba site of $PrBa_{1-x}Ca_xCo_2O_{5+\delta}$ (x = 0, 0.1, 0.2, 0.3, and 0.4) with increasing Ca amounts on the structural, physicochemical, electrical, and electrochemical properties. Interestingly, we observed a phase transition from a layered perovskite to a simple perovskite structure with increasing Ca content. In addition, we studied the correlation of the phase transition between electrical, electrochemical, and thermal expansion behaviors, respectively.

2.2. Experimental procedure

2.2.1 Synthesis of electrode and electrolyte powder

$PrBa_{1-x}Ca_xCo_2O_{5+\delta}$ (x = 0, 0.1, 0.2, 0.3, and 0.4) powders were synthesized by the conventional Pechini method. Calculated amounts of $Pr(NO_3)_3 \cdot 6H_2O$ (Aldrich, 99.9%, metal basis), $Ba(NO_3)_2$ (Aldrich, 99+%), $Ca(NO_3)_2 \cdot 4H_2O$ (Alfa Aesar, 99.98%), and $Co(NO_3)_2 \cdot 6H_2O$ (Aldrich, 98+%) were dissolved in deionized water to form an aqueous solution with a suitable amount of citric acid and ethylene glycol. After a viscous resin was formed, the mixture was heated to 523 K, followed by combustion. The combusted powders were calcined at 873 K for 4 hours to remove the residue and then ball-milled in acetone for 24 hours. The ball-milled powders were uniaxially pressed into pellets and sintered at various temperatures for 12 hours in the air. The chemical composition of the synthesized powders and their abbreviations are summarized in Table 2-1. The oxide anode $PrBaMn_2O_{5+\delta}$ (PBM), which has received attention recently, was used as an anode for single-cell measurements. As described in a previous report, the powder of PBM was prepared by the Pechini method.[24] The electrolyte $La_{0.9}Sr_{0.1}Ga_{0.8}Mg_{0.2}O_{2.85}$ powder was synthesized via the conventional solid-state reaction route. The starting materials of La_2O_3 (Aldrich, ≥99.9%), $SrCO_3$ (Aldrich, ≥99.9% trace metal basis), Ga_2O_3 (Aldrich, ≥99.99% trace metal basis), and MgO (Aldrich, ≥99.9% trace metal basis) powders were mixed by ball-milling with ethanol for 24 hours and then dried for 2 hours in an oven. The dried powder was pre-calcined at 1273 K for 6 hours and then ground with a pestle and mortar. The pre-calcined powder was uniaxially pressed into pellets and sintered at 1748 K for 5 hours and then polished to 250 mm thickness.

Table 2-1 Chemical compositions and abbreviations of samples

Amount of Ca (x)	chemical composition	Abbreviations
0	$PrBaCo_2O_{5+\delta}$	PBCO
0.1	$PrBa0.9Ca0.1Co_2O_{5+\delta}$	PBCCO10
0.2	$PrBa0.8Ca0.2Co_2O_{5+\delta}$	PBCCO20
0.3	$PrBa0.7Ca0.3Co_2O_{5+\delta}$	PBCCO30
0.4	$PrBa0.6Ca0.4Co_2O_{5+\delta}$	PBCCO40

2.2.2. Characterization

X-ray powder diffraction (XRD, Rigaku-diffractometer, Cu Kα radiation) was carried out to identify the phase of $PrBa_{1-x}Ca_xCo_2O_{5+\delta}$ (x = 0, 0.1, 0.2, 0.3, and 0.4) with a scanning rate of 0.5 ° min^{-1} in the

2θ range of 20 to 100 °. The diffraction patterns of $PrBa_{1-x}Ca_xCo_2O_{5+\delta}$ were refined using the Rietveld method with the general structure analysis system (GSAS) program.[25] Refinements were performed in the space group *P4/mmm* (ICSD 189052) [26] for the layered perovskite structures and in the space group $Pm\bar{3}m$ for the simple perovskite structures with a starting model based on the reported data of $La_{0.4}Sr_{0.6}CoO_3$ (ICSD 184074).[27] Asymmetric corrections were applied to the low-angle reflections. The scale factors, zero-point errors, unit-cell parameters, peak shapes, and isotropic displacement parameters were subsequently refined. Since no crystallographic ordering between Ba^{2+} and Ca^{2+} cations was monitored, the occupancies of Pr : Ba: Ca were fixed to 1 : (1 - *x*): *x* and the 0.5 : [(1 - *x*)/2]: *x*/2 for layered perovskites and simple perovskite, respectively. The crystallographic data and refinement results of $PrBa_{1-x}Ca_xCo_2O_{5+\delta}$ are summarized in Table 2-2. *In-situ* XRD of $PrBa_{1-x}Ca_xCo_2O_{5+\delta}$ was carried out in a temperature range of 303 to 1073 K and a 2θ range of 20 to 60 ° to identify the thermal stability and calculate the thermal expansion. The microstructure of the sintered composite cathodes of $PrBa_{1-x}Ca_xCo_2O_{5+\delta}$ was observed by using a field emission scanning microscope (FE-SEM, Nova SEM, FEI, USA). The oxygen content value δ of the samples was measured by thermogravimetric analysis (TGA) (SDT-Q600, TA Instruments, USA) from 373 to 1173 K with a heating/cooling rate of 1 K min^{-1} in the air with the sufficient relaxation time. The initial oxygen content values of the $PrBa_{1-x}Ca_xCo_2O_{5+\delta}$ at room temperature were determined by iodometric titration. The electrical conductivities of the $PrBa_{1-x}Ca_xCo_2O_{5+\delta}$ were measured by 4-probe DC measurements at temperatures ranging from 373 to 1023 K at intervals of 50 K.

2.2.3. Fabrication and testing of fuel cells

The electrochemical performance test was performed with composite cathodes of $PrBa_{1-x}Ca_xCo_2O_{5+\delta}$ – GDC that consisted of $PrBa_{1-x}Ca_xCo_2O_{5+\delta}$ powders, $Gd_{0.1}Ce_{0.9}O_{1.95}$ (GDC), and an organic binder (Heraeus V006) with a weight ratio of 6: 4: 12. An LSGM pellet with 250 μm thickness was used as an electrolyte. An LDC buffer layer was used to prevent chemical reactions between the composite cathode and LSGM electrolyte. Symmetrical half cells of $PrBa_{1-x}Ca_xCo_2O_{5+\delta}$ - GDC were applied for the

impedance studies. The composite cathode slurries were painted onto both sides (geometrical area of 0.36 cm^2) of the dense LSGM electrolyte symmetrically and then sintered at 1223 K for 4 hours in the air. The LSGM electrolyte supported single cells with a configuration of PBM anode|LDC|LSGM|LDC|composite cathode was fabricated using the screen-printing method to conduct single cell tests. The LDC buffer layer and PBM anode were screen-printed onto the sintered LSGM pellets (geometrical area of 0.36 cm^2) and the LDC buffer and composite cathode were screen-printed on the other side of the LSGM electrolyte and then the printed cells were sintered at 1223 K for 4 hours in the air. As described in a previous report, a Co–Fe catalyst (15 wt% of PBM) was added to enhance the catalytic activity of the oxide anode for fuel oxidation.[24]

Table 2-2 Summary of crystallographic data and refinement results for $PrBa_{1-x}Ca_xCo_2O_{5+\delta}$ (x = 0, 0.1, 0.2, 0.3 and 0.4)s

Sample	PBCO	PBCCO10	PBCCO20	PBCCO30		PBCCO40
	Double	Double	Double	Double (57 %)	Simple (43%)	Simple
Space group	*P4/mmm*	*P4/mmm*	*P4/mmm*	*P4/mmm*	*Pm-3m*	*Pm-3m*
***a* = *b* (Å)**	3.9010(2)	3.8915(2)	3.8913(5)	3.8891(7)	3.8423(3)	3.8426(2)
***c* (Å)**	7.6392(4)	7.6366(4)	7.6285(9)	7.6323(14)	3.8423(3)	3.8426(2)
***V* (Å^3)**	116.32(2)	115.62(2)	115.51(4)	115.44(6)	56.72(1)	56.74(1)
λ (Å)	1.5406	1.5406	1.5406	1.5406	1.5406	1.5406
R_p[a]	0.0800	0.0113	0.0183	0.0114		0.0821
R_{wp}[b]	0.1084	0.0158	0.0269	0.0161		0.1324

$R_p = \Sigma|I_o - I_c|/\Sigma I_o$

$R_{wp} = \left[\Sigma w|I_o - I_c|^2/\Sigma w{I_o}^2\right]^{1/2}$

Ag wires were attached to both anode and cathode electrodes of single cells using Ag paste as a current collector. The prepared single cell was attached to an alumina tube by using a ceramic adhesive (Aremco, Ceramabond 552). Humidified hydrogen (3% H_2O) was fed into the anode side as fuel, and the air was

fed into the cathode side as an oxidant during the single-cell test. I–V curves were examined using a BioLogic potentiostat at operating temperatures from 873 to 1073 K.

2.3. Results and discussion

The crystal structures of $PrBa_{1-x}Ca_xCo_2O_{5+\delta}$ (x = 0, 0.1, 0.2, 0.3, and 0.4) were determined by powder X-ray diffraction, as presented in the XRD patterns in Fig. 2-1 (a). Fig. 2-1 (b) presents magnified XRD patterns of $PrBa_{1-x}Ca_xCo_2O_{5+\delta}$ (x = 0, 0.1, 0.2, 0.3, and 0.4) from 45 º to 50 º, showing a phase transition. While PBCO, PBCCO10, and PBCCO20 crystallize in the tetragonal space group, *P4/mmm*, with a layered perovskite structure, PBCCO40 crystallizes in a simple cubic perovskite structure, $Pm\bar{3}m$.[13,20,25,28] In the case of PBCCO30, a new peak considered to represent a simple perovskite appears at 47.5 º, indicating the existence of both simple and layered perovskites. Further substitution of Ca (PBCCO40) results in a structural change of layered perovskite to simple perovskite; *i.e.*, the two peaks indexed as (2 0 0) and (0 0 4) disappeared and only a new peak (2 0 0) of a higher simple cubic symmetry perovskite appeared. Generally, the layered perovskite structure originates from the ionic radius difference between the large size Ba (1.49 Å) and the relatively smaller size *Ln* (Pr: 1.13 Å).[16] However, the relatively smaller size Ca (1.14 Å) can initiate the collapse of the layered structure through a reduction of the difference between the host (Pr) and dopants (Ba and Ca), resulting in a simple perovskite structure.[27,29] Furthermore, the co-existence of the phases between simple and double perovskites may be observed as an intermediate state of the phase transition. Kim *et al*. reported similar results on the co-existence of a layered perovskite (tetragonal) and a simple perovskite (orthorhombic).[11]

Rietveld refinements were performed to determine the detailed crystalline structures. PBCCO20 and PBCCO40 phases are successfully refined with pure layered and simple perovskite structures, respectively. In the case of the PBCCO30 phase, however, a mixture of phases of the layered and simple perovskites in a ratio of 57 : 43 in the product was identi?ed on the basis of the calculation results of the fractional scale factors (see Table 2-2 and Fig. 2-2). Fig. 2-3 displays the oxygen non-stoichiometry

of the $PrBa_{1-x}Ca_xCo_2O_{5+\delta}$ as a function of temperature in air. These curves were derived from a thermal gravimetric analysis (TGA) with the initial oxygen content values determined by iodometric titration.

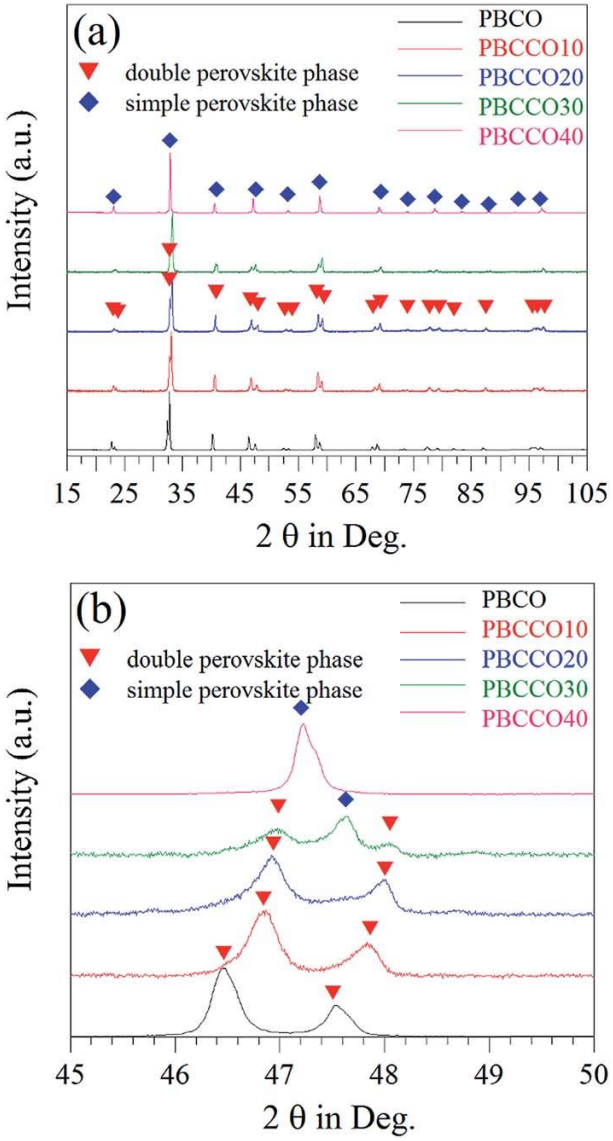

Fig. 2-1. X-ray diffraction patterns of $PrBa_{1-x}Ca_xCo_2O_{5+\delta}$ powders sintered at 1373 K for 12 h in the air in the 2θ range of (a) 15° to 105° (b) 45° to 50°

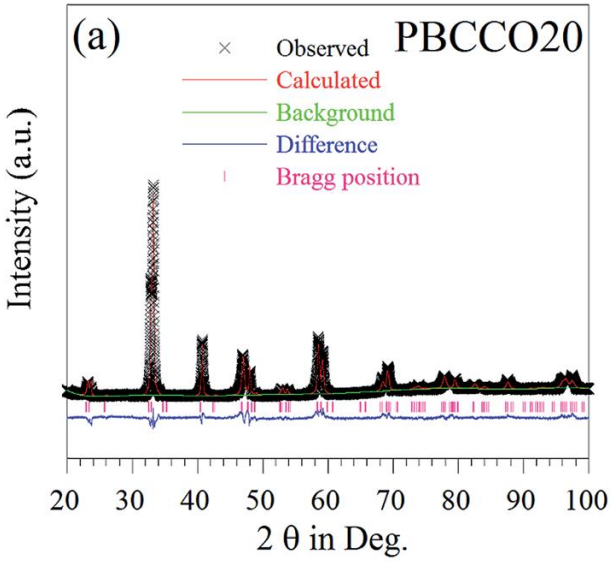

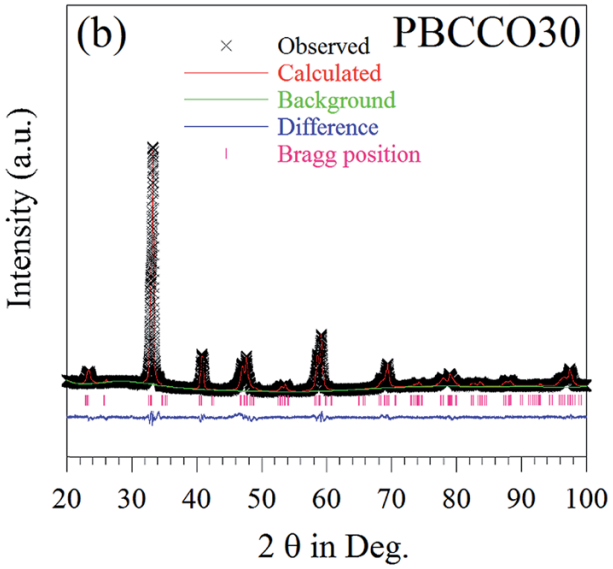

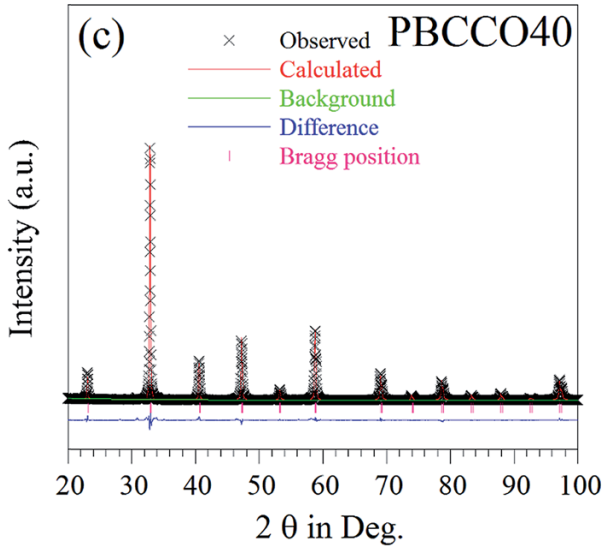

Fig. 2-2. Final Rietveld plots of $PrBa_{1-x}Ca_xCo_2O_{5+\delta}$ (x = 0.2, 0.3, and 0.4). The calculated pattern (red solid line) is compared with the observed data (×). The positions of reflections are indicated by magenta and vertical bars. The difference between the observed and calculated profiles is shown at the bottom (blue solid line).

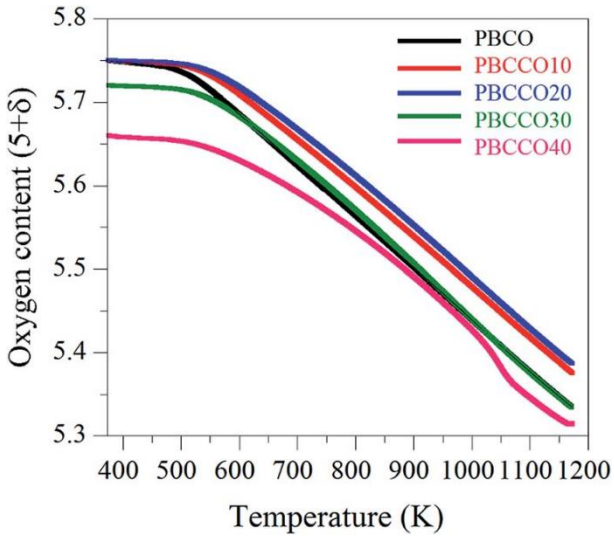

Fig. 2-3. Variation in oxygen contents with temperature in air for $PrBa_{1-x}Ca_xCo_2O_{5+\delta}$ (x = 0, 0.1, 0.2, 0.3 and 0.4) powders.

All samples dramatically lose weight above 573 K due to the loss of the lattice oxygen accompanied

by the reduction of Co^{4+} to Co^{3+}.[11] The amount of oxygen loss decreases with increasing Ca content in the layered perovskite structures (PBCO, PBCCO10, and PBCCO20). This shows that Ca doping into the Ba site can suppress the mobile oxygen losses from the lattice in the high-temperature range. Choi et al. reported that the smaller size difference between Ca^{2+} and Pr^{3+} ions perturbs the ordering between Ba and Pr layers, resulting in an increased coordination number of Pr^{3+} and oxygen concentration.[11,13,30] Moreover, the bonding strength of oxygen increases with Ca doping into the Ba site of PBCO.[13] The higher oxygen content of the Ca doped layered perovskite structures can explain the enhanced surface activity toward the ORR, which is responsible for the high diffusion of oxygen ions and high electrical conductivity in the bulk.[14,26]

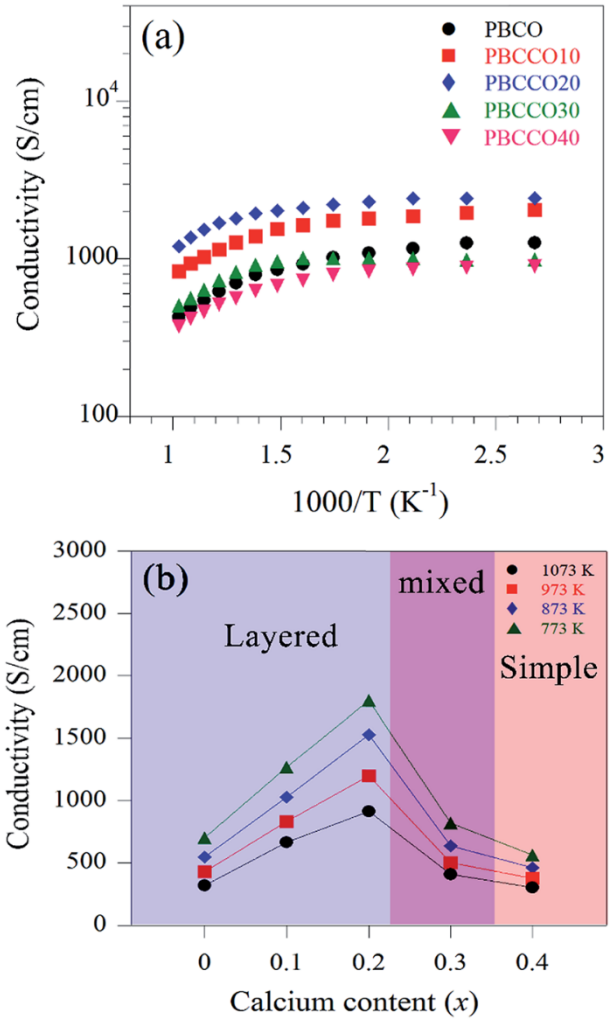

Fig. 2-4. (a) The electrical conductivity of $PrBa_{1-x}Ca_xCo_2O_{5+\delta}$ and (b) the relationship between conductivity and Ca doping contents.

The simple perovskite structure PBCCO40 shows a lower oxygen content than the layered perovskite structures (PBCO, PBCCO10, and PBCCO20). The mixed-phase PBCCO30 displays an intermediate value between the layered perovskite structures (PBCO, PBCCO10, and PBCCO20) and the simple perovskite structure, PBCCO40. The electrical conductivity of the $PrBa_{1-x}Ca_xCo_2O_{5+\delta}$ is described by an Arrhenius plot in Fig. 2-4(a). The electrical conductivity of all samples decreases with increasing temperature, showing typical metallic behavior because of the decrease in charge carrier concentration accompanied by the loss of oxygen, as mentioned with regard to the TGA results (Fig. 2-3).[16,31] The relationship between the concentration of oxygen and the electrical conductivity can be explained by the predominant defects according to the following pseudo-chemical reaction.[30,32,33] The predominant defects in $PrBa_{1-x}Ca_xCo_2O_{5+\delta}$ are oxygen interstitials in the PrO layer, O_i'', and electronic holes,

$$h^{\cdot} = Co_{Co}^{\cdot} \qquad \text{Eq. 2-1}$$

Following the Kröger–Vink notation, the pseudo-chemical reaction can be regarded as the interaction between the defects and the atmosphere, as delineated in Eq. 2-2

$$\frac{1}{2}O_2 + V_m^{\times} + 2Co_{Co}^{\times} \leftrightarrow O_m'' + 2Co_{Co}^{\cdot} \qquad \text{Eq. 2-2}$$

, where O_m'' is the mobile oxygen species and $V_m^{\times}$ is the mobile oxygen vacancies. The decrease in mobile oxygen concentration gives rise to a decrease in electronic holes, *i.e.*, charge carriers, which consequently leads to low conductivity. This also can be explained by electro-neutrality,

$$2[O_m''] = Co_{Co}^{\cdot} \qquad \text{Eq. 2-3}$$

Fig. 2-4 (b) shows the correlation between the amount of Ca and electrical conductivity. The electrical conductivity increases with the increasing amount of Ca dopant in the layered perovskite (PBCO, PBCCO10, and PBCCO20). The mixed-phase PBCCO30 has intermediate conductivity between the layered perovskite (PBCO, PBCCO10, and PBCCO20) and the simple perovskite, PBCCO40. The electrical conductivity behavior as a function of Ca amount indicates that the increased hole charge carriers due to increasing mobile oxygen concentration results in increased electrical conductivity of the Ca doped $PrBaCo_2O_{5+\delta}$.

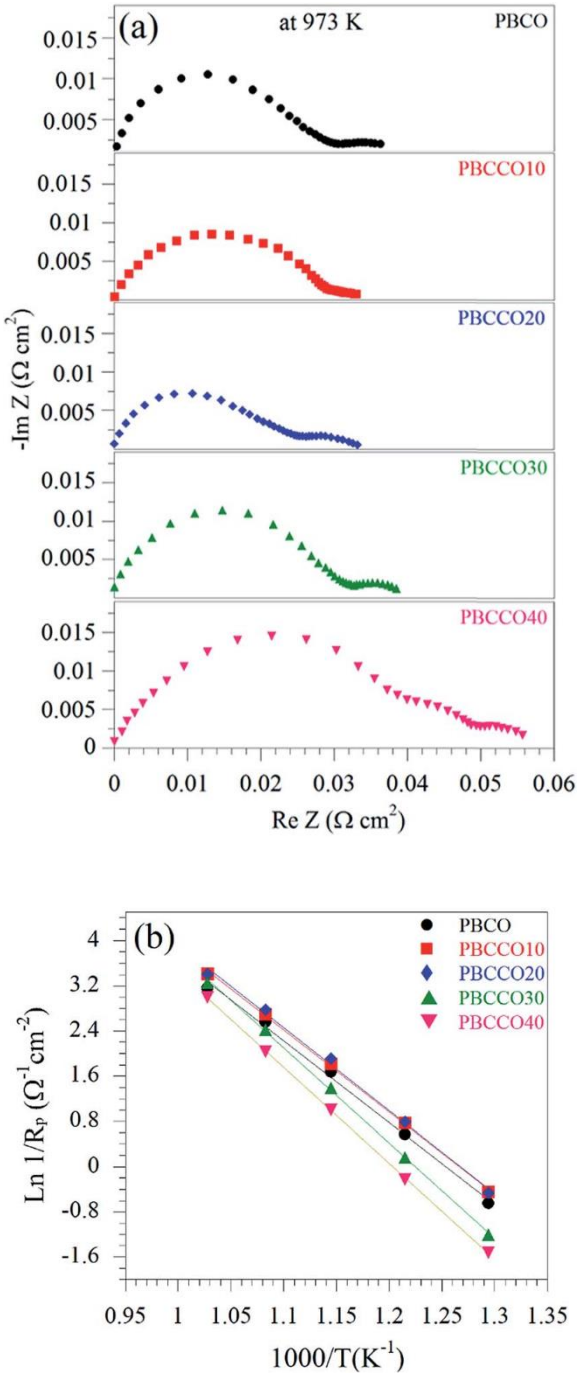

Fig. 2-5. (a) Impedance spectra of $PrBa_{1-x}Ca_xCo_2O_{5+\delta}$ cathodes on LSGM electrolyte with an LDC buffer layer in a symmetrical cell measured at 973 K under OCV conditions. (b) Temperature dependence of the $PrBa_{1-x}Ca_xCo_2O_{5+\delta}$ cathode polarization by Arrhenius plots.

The electro-catalytic activity for the oxygen reduction of a cathode can be obtained from the

electrochemical impedance spectra (EIS) of symmetric cells of $PrBa_{1-x}Ca_xCo_2O_{5+\delta}$ in Fig. 2-5 (a). The polarization resistance values of $PrBa_{1-x}Ca_xCo_2O_{5+\delta}$ (x = 0, 0.1, 0.2, 0.3 and 0.4) - GDC are 0.036, 0.033, 0.033, 0.038, and 0.050 Ω cm^2 at 973 K, respectively. Due to the higher oxygen diffusion coefficients and surface exchange coefficients of the layered perovskite structure compared to that of the simple perovskite structure, the layered perovskite structure(PBCO, PBCCO10, and PBCCO20) exhibits lower polarization resistance than the mixed-phase PBCCO30 and the simple perovskite structure PBCCO40.[16,19] Ca doping decreases the polarization resistance of the layered perovskite structures (PBCO, PBCCO10, and PBCCO20) due to the increased conductivity and mobile oxygen concentration.[28,34,35]

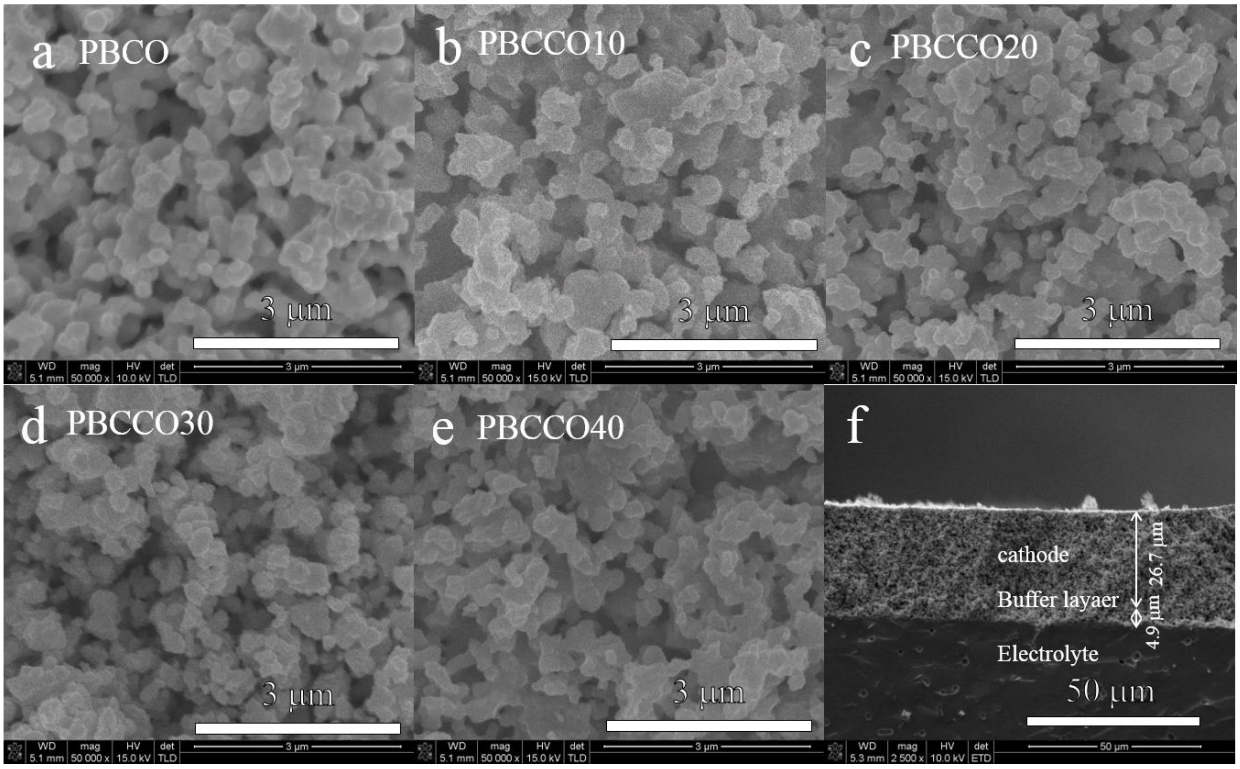

Fig. 2-6. Scanning electron microscope image of $PrBa_{1-x}Ca_xCo_2O_{5+\delta}$ composites, sintered at 973 K for 4 hours. (a) x = 0, (b) x = 0.1, (c) x = 0.2, (d) x = 0.3, (e) x = 0.4 and (f) cross-sectional image of x = 0.3

The Arrhenius plots of the polarization resistance of $PrBa_{1-x}Ca_xCo_2O_{5+\delta}$ are shown in Fig. 2-5 (b). The activation energy is directly related to the cathode characteristics including oxygen adsorption, dissociation, and surface/bulk diffusion.[16,33,36] The activation energy of the layered perovskite (PBCO, PBCCO10, and PBCCO20) is around 120 kJ mol^{-1} and these samples exhibit lower activation energy than the mixed-phase PBCCO30 (139 kJ mol^{-1})) and simple perovskite PBCCO40 (138 kJ mol^{-1}). This indicates that the layered perovskite (PBCO, PBCCO10, and PBCCO20) has higher catalytic activity than simple PBCCO40 and mixed-phase PBCCO30.

The microstructure of the electrode is related to the surface area, electrochemically active sites, gas diffusion, and electron transport. [37,38] These properties affect fuel cell performance through the reaction kinetics, charge transport, and mass transport processes. In this regard, we observed the microstructure of the $PrBa_{1-x}Ca_xCo_2O_{5+\delta}$ - GDC by FE-SEM to identify the microstructural effects of the substitution of Ca.

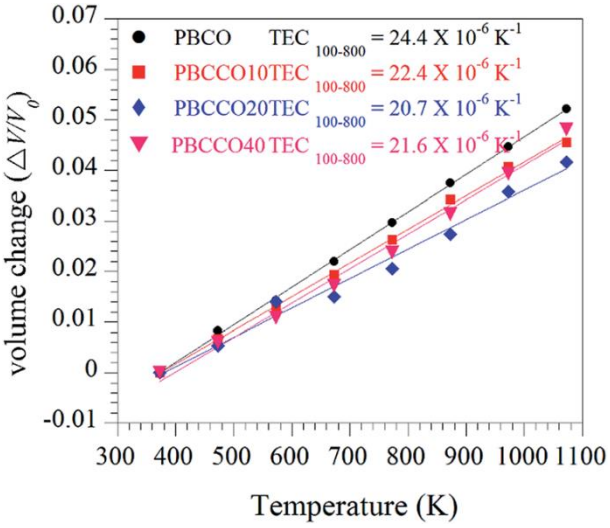

Fig. 2-7. Dependence of unit cell volume (Å^3) on temperature from in situ XRD patterns of $PrBa_{1-x}Ca_xCo_2O_{5+\delta}$ (x = 0, 0.1, 0.2, and 0.4).

As shown in Fig. 2-6, the microstructures of the $PrBa_{1-x}Ca_xCo_2O_{5+\delta}$ - GDC cathodes are similar and thus it is considered that the substitution of Ca for Ba and the phase transition do not affect the electrochemically active sites. The cross-sectional images of the PBCCO–GDC cathode indicate that

the interface of the porous cathode (25 mm thickness), the dense buffer (5 mm thickness), and the electrolyte is well-connected. Fig. 2-7 shows the cell volume changes of $PrBa_{1-x}Ca_xCo_2O_{5+\delta}$ (x = 0, 0.1, 0.2 and 0.4) determined by the *in-situ* X-ray diffraction measurement (see Fig. 2-8) as the temperature was increased from 303 to 1073 K.

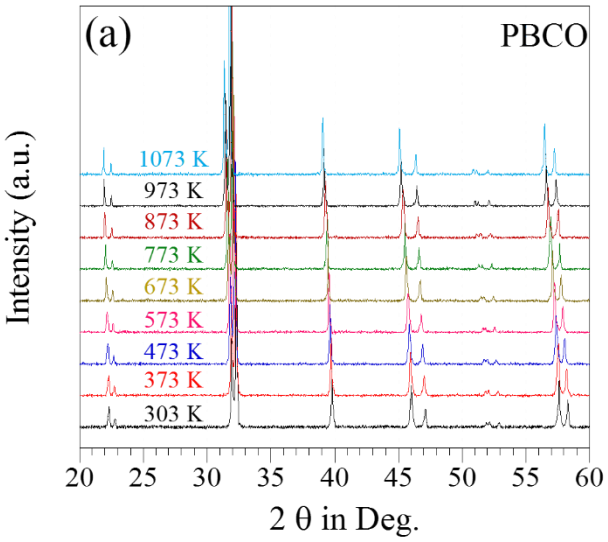

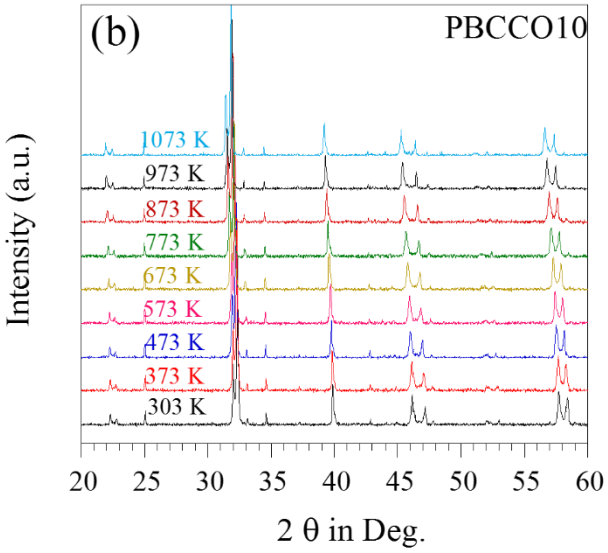

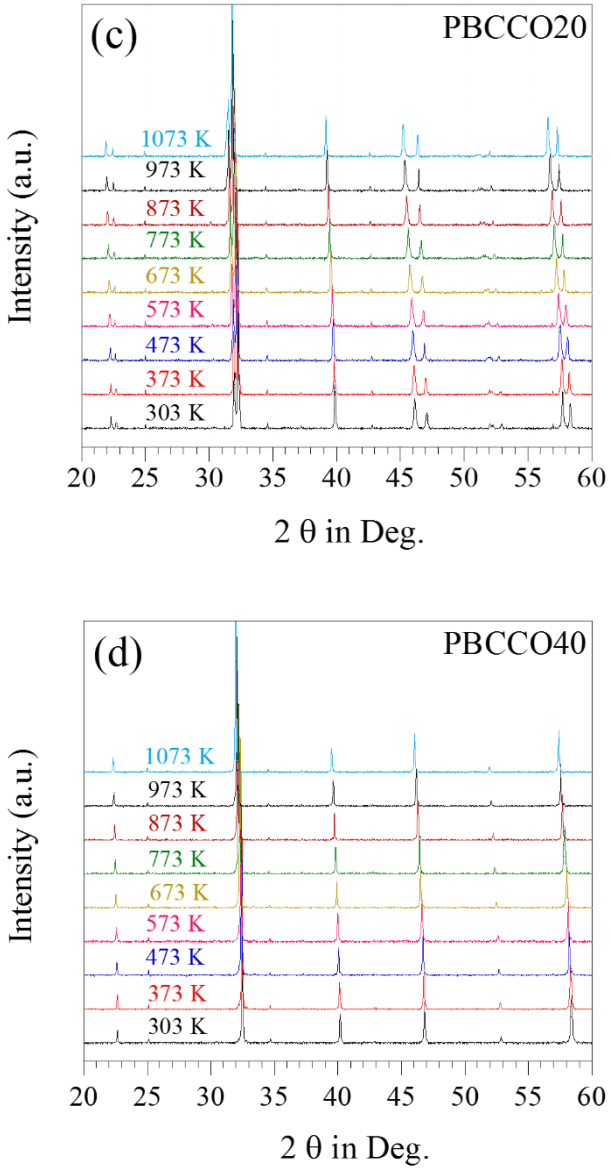

Fig. 2-8. *In situ* XRD patterns of $PrBa_{1-x}Ca_xCo_2O_{5+\delta}$ (a) $x = 0$, (b) $x = 0.1$, (c) $x = 0.2$ and (d) $x = 0.4$ in air from 303 to 1073 K.

From the Bragg equation, the shift of the peak to a lower 2q value denotes the expansion of the lattice, indicating thermal expansion. [39,40] The thermal exchange coefficients (TECs) of the tetragonal perovskite structure PBCO, PBCCO10, and PBCCO20 and cubic perovskite structure PBCCO40 were calculated from the cell volume change and the following equation.

$$\alpha_v = \frac{(v_2 - v_1)/(T_2 - T_1)}{v_1} \qquad \text{Eq. 2-4}$$

In the layered perovskite, the TEC of the Ca doped PBCO decreases with the increasing amount of Ca dopant. Generally, the larger TEC values for the cobalt-based perovskite oxides can be attributed to the increase of the average ionic radius of Co ions during the thermal expansion measurement.[42] The reduction of Co^{4+} to Co^{3+} caused by a loss of oxygen also leads to high TECs due to the larger ionic size of Co^{3+} relative to that of Co^{4+}. Regarding this, minimizing oxygen loss and decreasing the concentration of Co^{3+} are key steps toward stabilizing the thermal expansion behavior.

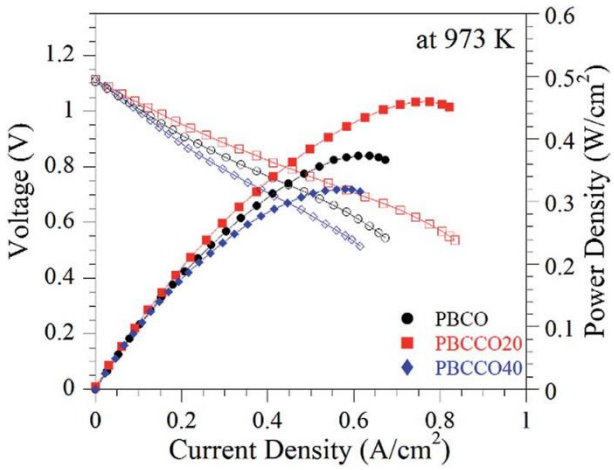

Fig. 2-9. *I–V* curves and corresponding power density curves of single cells of $PrBa_{1-x}Ca_xCo_2O_{5+\delta}$-GDC|LDC|LSGM|PBM ($x$ = 0, 0.2 and 0.4) at 973 K.

Therefore, the substitution of Ca into the Ba site of $PrBaCo_2O_{5+\delta}$ is beneficial to lower the TEC by suppressing the spin-state transition of Co^{3+}.[8,30] To evaluate the performance of the layered perovskite (PBCO and PBCCO20) and simple perovskite (PBCCO40) cathode materials in a practical fuel cell, we used electrolyte supported cells based on a 250 μm thick LSGM electrolyte and PBM anode. Fig. 2-9 depicts the current-voltage (I-V) curves and corresponding power density curves obtained with a configuration of a composite-cathode |LDC|LSGM|LDC|PBM single cell at 973 K. The maximum power densities of the layered perovskite PBCO and PBCCO20 are 0.373 and 0.460 W cm^2, respectively, which are much higher than those of the simple perovskite PBCCO40 (0.320 W cm^2) at 973 K. It is assumed that the high catalytic activity and fast oxygen ion diffusion of the cation ordered layered perovskite structure may account for the higher single cell performance of

the layered structure (PBCO and PBCCO20) than that of the simple perovskite PBCCO40.[19,33] Moreover, the enhanced singe cell performance of the PBCCO20 can be explained by the increased mobile oxygen concentration, which can be anticipated from the behavior of the conductivity and cathode polarization. In summary, we investigated the effect of the Ca dopant in the layered perovskite $PrBaCo_2O_{5+\delta}$. In the layered structure, Ca substitution enhances the electrical and electrochemical properties with less thermal stress. On the other hand, the simple perovskite structure shows relatively lower electrical conductivity and electrochemical performance as compared to the layered perovskite structure. The electrical and electrochemical properties of the mixed-phase PBCCO30 show mixed behavior of the layered perovskite and the simple perovskite.

2.4. Conclusion

The effect of calcium doping into the layered perovskite $PrBa_{1-x}Ca_xCo_2O_{5+\delta}$ was investigated in view of the phase transition and the correlation between the phase transition, electrical properties, and electrochemical performance. In the structural study, a phase transition between the layered perovskite and the simple perovskite occurs with Ca doping into $PrBaCo_2O_{5+d}$ and, during the phase transition, the co-existence of simple and layered perovskite phases was observed at 30 mol% of Ca (PBCCO30). The simple perovskite PBCCO40 presents low electrical and electrochemical properties as compared to the layered perovskite. The mixed-phase PBCCO30 shows characteristics of the layered perovskite and simple perovskite simultaneously in terms of electrical and electrochemical properties. It is considered that the co-existence of the layered perovskite and simple perovskite does not provide a synergetic effect between the phases with respect to the electrical and electrochemical properties. Consequently, in the layered perovskite structure, Ca doping leads to enhanced electrochemical performance and increased electrical conductivity while suppressing thermal expansion.

References

[1] B. C. H. Steele, *J. Mater. Sci*., 2001, **36**, 1053-1068.

[2] S. B. Adler, J. A. Lane, and B. C. H. Steele, *J. Electrochem. Soc.*, 1996, **143**, 3554-3564.

[3] J. Kim, W. Seo, J. Shin, M. Liu, and G. Kim, *J. Mater. Chem. A*, 2013, **1**, 515-519.

[4] H. Fukunaga, M. Koyama, N. Takahashi, C. Wen, and K. Yamada, *Solid State Ionics*, 2000, **132**, 279-285.

[5] K. T. Lee and A. Manthiram, *J. Electrochem. Soc.*, 2005, **152**, A197-A204.

[6] S. Park, S. Choi, J. Shin, and G. Kim, *J. Power Sources*, 2012, **210**, 172-177.

[7] A. Jun, S. Yoo, O. Gwon, J. Shin, and G. Kim, *Electrochim. Acta*, 2013, **89**, 372-376.

[8] K. T. Lee and A. Manthiram, *Solid State Ionics*, 2005, **176**, 1521-1527.

[9] C. Torres-Garibay, D. Kovar, and A. Manthiram, *J. Power Sources*, 2009, **187**, 480-486.

[10] A. Tarancón, S. J. Skinner, R. J. Chater, F. Hernández-Ramírez, and J. A. Kilner, *J. Mater. Chem.*, 2007, **17**, 3175-3181.

[11] J. H. Kim, F. Prado, and A. Manthiram, *J. Electrochem. Soc.*,2008, **155**, B1023-B1028.

[12] S. Choi, S. Yoo, J. Kim, S. Park, A. Jun, S. Sengodan, J. Kim, J. Shin, H. Y. Jeong, Y. Choi, G. Kim, and M. Liu, *Sci. Rep.*, 2013, **3**, 2426.

[13] S. Yoo, A. Jun, Y.-W. Ju, D. Odkhuu, J. Hyodo, H. Y. Jeong, N. Park, J. Shin, T. Ishihara, and G. Kim, *Angew. Chem., Int. Ed.*, 2014, **53**, 13064-13067.

[14] G. Kim, S. Wang, A. J. Jacobson, Z. Yuan, W. Donner, C. L. Chen, L. Reimus, P. Brodersen, and C. A. Mims, *Appl. Phys. Lett.*, 2006, **88**, 24103.

[15] Z. Yuan, J. Liu, C. L. Chen, C. H. Wang, X. G. Luo, X. H. Chen, G. Kim, D. X. Huang, S. S. Wang, A. J. Jacobson, and W. Donner, *Appl. Phys. Lett.*, 2007, **90**, 212111.

[16] G. Kim, S. Wang, A. J. Jacobson, L. Reimus, P. Brodersen, and C. A. Mims, *J. Mater. Chem.*, 2007, **17**, 2500-2505.

[17] J. H. Kim, Y. Kim, P. A. Connor, W. Zhou, J. T. S. Irvine, and J. Bae, *J. Power Sources*, 2009, **194**, 704-711.

[18] S. Yoo, J. Shin, and G. Kim, *J. Mater. Chem.*, 2011, **21**, 439-443.

[19] A. A. Taskin, A. N. Lavrov, and Y. Ando, *Appl. Phys. Lett.*, 2005, **86**, 091910.

[20] S. Park, S. Choi, J. Kim, J. Shin and G. Kim, *ECS Electrochem. Lett*., 2012, **1**, F29-F32.

[21] A. Tarancón, J. Peña-Martínez, D. Marrero-López, A. Morata, J. C. Ruiz-Morales, and P. Núñez, *Solid State Ionics*, 2008, **179**, 2372-2378.

[22] N. Caillol, M. Pijolat, and E. Siebert, *Appl. Surf. Sci.*, 2007, **253**, 4641-4648.

[23] W. Lee, J. W. Han, Y. Chen, Z. Cai, and B. Yildiz, *J. Am. Chem. Soc*., 2013, **135**, 7909-7925.

[24] S. Sengodan, S. Choi, A. Jun, T. H. Shin, Y.-W. Ju, H. Y. Jeong, J. Shin, J. T. S. Irvine, and G. Kim, *Nat. Mater.*, 2014, **14**, 205-209.

[25] A. C. Larson and R. B. Von Dreele, General structure analysis (GSAS), Los Alamos National Laboratory, Los Alamos, NM, 1987.

[26] M. M. Seikh, V. Pralong, O. I. Lebedev, V. Caignaert, and B. Raveau, *J. Appl. Phys*., 2013, **114**, 013902.

[27] Y. Wang, L. Yu, J. Wang, L. Chen, W. Gao, X. Du, and L. Biao, Mater. Lett., 2012, 75, 39–41.

[28] S. Choi, J. Shin, and G. Kim, *J. Power Sources*, 2012, **201**, 10-17.

[29] R. D. Shannon, *Acta Crystallogr., Sect. A: Cryst. Phys., Diffr. Theor. Gen. Crystallogr.*, 1976, **32**, 751-767.

[30] S. Choi, S. Park, J. Shin, and G. Kim, *J. Mater. Chem. A*, 2015, **3**, 6088-6095.

[31] K. Zhang, L. Ge, R. Ran, Z. Shao, and S. Liu, *Acta Mater.*, 2008, **56**, 4876-4889.

[32] S. Sengodan, J. Kim, J. Shin, and G. Kim, *J. Electrochem. Soc*., 2011, **158**, B1373-B1379.

[33] A. Jun, S. Yoo, Y.-W. Ju, J. Hyodo, S. Choi, H. Y. Jeong, J. Shin, T. Ishihara, T. H. Lim, and G. Kim, *J. Mater. Chem. A*, 2015, **3**,15082-15090.

[34] S. Yoo, J. Shin, and G. Kim, *J. Electrochem. Soc.*, 2011, **158**, B632-B638.

[35] J. Kim, A. Jun, J. Shin, and G. Kim, *J. Am. Ceram. Soc.*, 2014, **97**, 651-656.

[36] S. Lu, X. Meng, Y. Ji, C. Fu, C. Sun, and H. Zhao, *J. Power Sources*, 2010, **195**, 8094-8096.

[37] J. H. Nam and D. H. Jeon, *Electrochim. Acta*, 2006, **51**, 3446-3460.

[38] M. Andersson, J. Yuan, and B. Sundén, *Appl. Energy*, 2010, **87**, 1461-1476.

[39] C. Kuroda, K. Zheng, and K. Świerczek, *Int. J. Hydrogen Energy*, 2013, **38**, 1027-1038.

[40] D. Bahadur, W. Fischer, and M. V. Rane, *Mater. Sci. Eng. A*, 1998, **252**, 109-116.

[41] C. Y. Huang, D. K. Agrawal, and H. A. Mckinstry, *J. Mater. Sci.*, 1995, **30**, 3509-3514.

[42] M. Mori and N. M. Sammes, *Solid State Ionics*, 2002, **146**, 301-312.

Chapter 3. Energy conversion (2): Investigation of the Fe doping effect on the B-site of the layered perovskite $PrBa_{0.8}Ca_{0.2}Co_2O_{5+\delta}$ for a promising cathode material of the intermediate-temperature solid oxide fuel cells

DOI: https://doi.org/10.1016/j.ijhydene.2018.10.182

3.1. Introduction

Solid oxide fuel cell (SOFC) is one of the most promising energy conversion systems that convert chemical energy into electrical energy directly with high energy conversion efficiency, environmental friendliness, and fuel flexibility.[1-3] Despite these advantages, its high operating temperature of 800 - 1000 ºC leads to serious problems such as high material costs, chemical reactions between fuel cell components, thermal stress/strain, and chemical/thermal degradation.[4] There have been significant efforts to decrease operating temperature down to the intermediate range (500 - 700 ºC) to overcome the problems associated with high operating temperatures. Lowering the operating temperature, however, causes serious problems such as poor activity for oxygen reduction reaction (ORR) and low oxygen-ion conductivity, resulting in inferior electrochemical performance of SOFC.[5] One of the major challenges in lowering the operating temperature is to develop electrocatalytically active and stable cathode toward ORR at low operating temperatures. Considerable efforts have been devoted to developing new alternative cathode materials that guarantee excellent and stable electrochemical performance in the intermediate temperature.

For these reasons, mixed ionic-electronic conducting (MIEC) perovskite oxides have been attracting much attention as cathode materials of intermediate-temperature solid oxide fuel cell (IT-SOFC). MIEC perovskite materials exhibit superior performance in the intermediate temperature range because of their high conductivity, thermal stability, high oxygen ion diffusion, and high surface oxygen exchange characteristics. Also, in MIEC perovskite materials, ORR occurs not only at the triple-phase boundary (TPB) between electrolyte, cathode, and gas-phase but also at the entire surface of the cathode (double-phase boundary). [6-10]

Among MIEC perovskite materials, layered perovskite oxides, $LnBaCo_2O_{5+\delta}$ (*Ln* = Pr, Nd, Sm, Gd, and *etc.*), have gained much attention because they show a very low area-specific resistance (ASR), high oxygen kinetics, and good electrochemical performance compared to simple perovskite oxides.[11-14] According to the previously reported density functional theory (DFT) modeling, the layered perovskite oxides have pore channels in the [*Ln*-O] and [Co-O] planes, providing a fast oxygen transport path.[14] However, Co contained layered perovskite oxides have some disadvantages such as high thermal expansion coefficients (TECs), chemical degradation, and poor redox stability.[15,16]

Our previous study has shown that Ca doping at A-site in $LnBaCo_2O_{5+\delta}$ (*Ln* = Pr and Nd) can improve electrical properties and electrochemical performance with structural, redox, chemical, and thermal stability.[8,9,11] Similarly, a partial substitution of transition metal (*e.g.* Mn, Fe, Ni, Cu, and *etc.*) on the B-site in $LnBaCo_2O_{5+\delta}$ not only increases the electrochemical performance of the fuel cell but also shows high redox stability and low TECs.[2,3,13,17-19] Among B-site doping in $LnBaCo_2O_{5+\delta}$, Fe doping is known to decrease TECs and enhance oxygen diffusivity, catalytic activity for ORR, and thermal stability.[2,3,15]

The aim of this study is to overcome the drawbacks of the Co-based perovskite oxides by introducing Fe in B-site of $PrBa_{0.8}Ca_{0.2}Co_2O_{5+\delta}$ as the IT-SOFC cathode material. Stronger Fe-O bonding as compared with Co-O bonding can improve the electrochemical performance by increasing the mobile oxygen species in the Pr-O layer [2,15] which can be easily attached and released from the lattice. Moreover, the increased bonding strength between transition metal and oxygen provides improved redox, thermal, long-term stability.

Here, we investigated the effect of B-site Fe doping through systematic characterization of its crystal structure, electrical conductivity, electro-catalytic activity, and electrochemical performance.

3.2. Experimental procedure

3.2.1. Synthesis and fabrication

$PrBa_{0.8}Ca_{0.2}Co_{2-x}Fe_xO_{5+\delta}$ (PBCCF; x = 0, 0.5, and 1.0) oxides were synthesized by the previously

reported conventional sol-gel (Pechini) method.[11] Stoichiometrically calculated amounts of $Pr(NO_3)_3 \cdot 6H_2O$, $Ba(NO_3)_2$, $Ca(NO_3)_2 \cdot 4H_2O$, $Co(NO_3)_2 \cdot 6H_2O$, $Fe(NO_3)_3 \cdot 9H_2O$, and citric acid were dissolved in deionized water with a sufficient amount of polyethylene glycol. After nitrates and citric acid were completely dissolved, the viscous resin was formed and heated at 280 ºC until the resin was completely combusted. The combusted powder was calcined at 600 ºC for 4 h, and then ball-milled with acetone for 24 h.

Table 3-1 Abbreviations of the samples.

Chemical composition	Abbreviations
$PrBa_{0.8}Ca_{0.2}Co_2O_{5+\delta}$	PBCCO
$PrBa_{0.8}Ca_{0.2}Co_{1.5}Fe_{0.5}O_{5+\delta}$	PBCCF05
$PrBa_{0.8}Ca_{0.2}Co_{1.0}Fe_{1.0}O_{5+\delta}$	PBCCF10

The ball-milled powder was pressed into pelletizer and then sintered in air at 1050 ºC for 12 h. The chemical composition of the samples and their abbreviations are summarized in Table 3-1.

3.2.2. Characterizations

The crystal structures of PBCCFs were analyzed by X-ray diffractometer (XRD; D/MAX2500 V/PC, Rigaku Co.) using Kα radiation at a scanning rate of 0.2 º min^{-1}. Crystallographic information was obtained through Rietveld refinement using the GSASII program.[20] Thermal stability and thermal expansion coefficient (TEC) in the air atmosphere were analyzed using an in-situ XRD (AXS D8 Advance diffractometer, Bruker) at a temperature range of room temperature to 700 ºC. Microstructures of PBCCFs cathodes were examined by field emission scanning electron microscopy (FE-SEM; Nova Nano SEM, FEI). Electrical conductivities of the PBCCFs were measured by the four-probe DC method using a rectangular-shaped bar type sample (approximately 90% theoretical density). Thermogravimetric analysis (TGA) was used to observe oxygen content in the PBCCFs at a heating/cooling rate of 2 ºC min1 in the air between 100 and 700 C using a thermogravimetric analyzer (TGA; SDT-Q600, TA instrument). Iodometric titration was carried out to determine the initial oxygen

content of PBCCFs. The impedance spectra of PBCCF cathodes were recorded using a symmetric cell. The GDC powder was pressed into pellets and sintered at 1350 ºC for 4 h in the air to obtain 250 μm thickness dense electrolyte substrate. Slurries of samples were screen-printed onto both sides of a GDC electrolyte to form a symmetric cell. The electrode slurries were prepared by mixing PBCCF powders with Heraeus V006 organic binder. The screen-printed cathodes were sintered at 950 ºC for 4 h in air. A silver paste and a silver wire were used as the current collector for both side electrodes. A Ni-$Gd_{0.1}Ce_{0.9}O_{1.95}$ (Ni-GDC) anode supported cell with a configuration of Ni-GDC|GDC|PBCCFs was fabricated to conduct the single-cell test. For the anode support, NiO and GDC powders were mixed with corn starch and ball-milled together for 24 h in ethanol. The ball-milled powder was dried and pelletized into a pellet (~0.6 mm thick and 15 mm diameter). A thin GDC electrolyte layer was deposited on pre-sintered NiO-GDC anode support and then dried in the air, followed by sintering at 1400 ºC for 5 h. The electrode slurries were prepared by mixing PBCCF powders with V006 organic binder. After sintering, PBCCF cathode slurries were painted onto the top of the GDC electrolyte by screen printing method and fired at 950 ºC for 4 h in the air (~20 μm thickness and 0.36 cm^2 diameter). Current collector, Ag wires were attached on both electrodes using Ag paste. A prepared single cell was attached to the alumina tube using ceramic adhesive (Aremco, Ceramabond 552). Humidified hydrogen (3% H_2O) and dried air were fed with 100 sccm flow rate to the anode and cathode as fuel and oxidant, respectively. Cell performance (with scan rate 10 mV s^{-1}) and impedance spectra were evaluated using a potentiostat (VMP3, Biologic Co.).

3.3. Results and Discussion

3.3.1 Characterization

Fig. 3-1(a) presents the XRD patterns of PBCCFs sintered at 1050 ºC in the air for 4 h, indicating that PBCCFs have a single-phase perovskite structure without detectable impurity or secondary phase. The Rietveld refinement results (Fig. 3-1(b) and Table 3-2) reveal that the structure of PBCCFs samples have a tetragonal structure with space group P4/mmm and presents good agreement between calculated

and observed profiles. The crystallographic information of PBCCFs implies that the lattice volume gradually increases with increasing Fe amount probably due to the substitution of relatively large Fe^{3+}/Fe^{4+} ions into the small Co^{3+}/Co^{4+} ions. The lattice parameter, cell volume, and initial oxygen contents at room temperature measured by iodometric titration are summarized in Table 3-2. The phase evaluation of PBCCF05 against temperature is carried out by the *in-situ* XRD measurement between the temperature range of 100 ºC ~ 700 ºC as shown in Fig. 3-1(c). PBCCF05 shows no structural or chemical change and is thermally stable in the cathode operating environment.

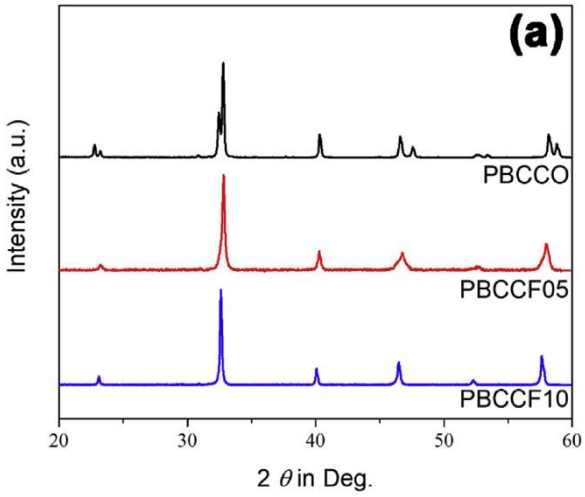

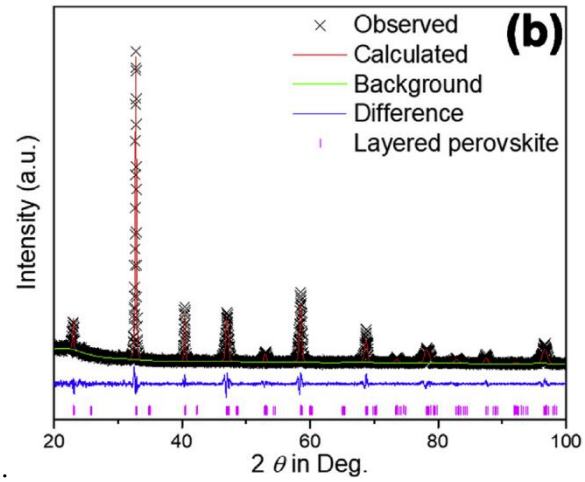

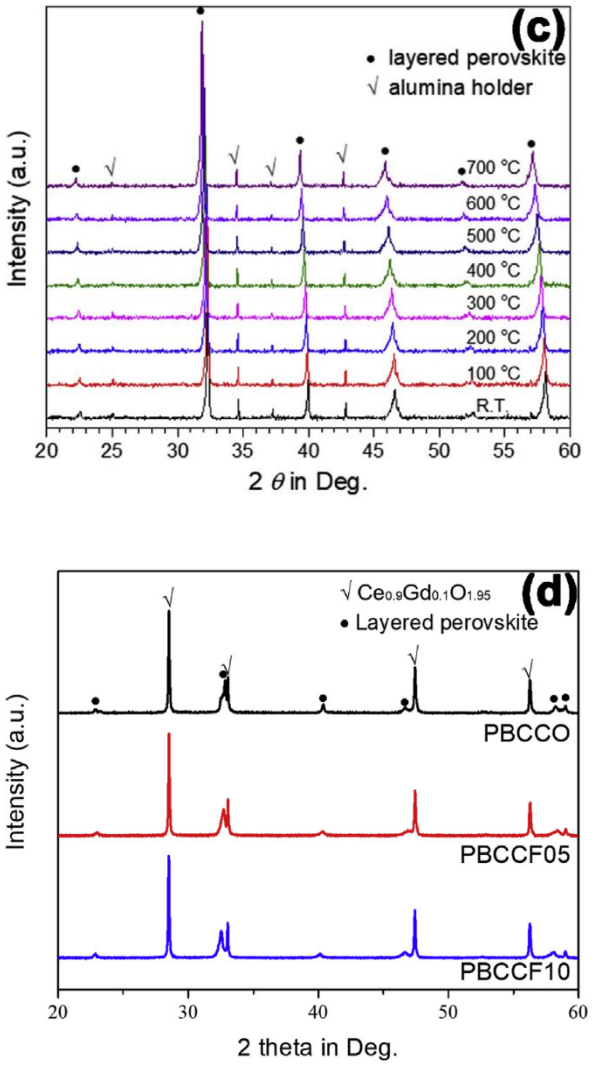

Fig. 3-1. (a) XRD results of PBCCFs, (b) Rietveld refinement result of PBCCF05 (c) in-situ XRD of PBCCF05, and (d) reactivity test with GDC of PBCCFs.

The chemical compatibility between the cathode and GDC electrolyte was analyzed by XRD measurements of a mixture of PBCCFs and GDC fired at 950 ºC for 4 h, as presented in Fig. 3-1(d). The XRD patterns suggest that there are no detectable secondary phases or impurities, indicating that the cathodes do not react with the GDC electrolyte. The microstructures of PBCCFs are examined using field emission scanning electron microscopy (FE-SEM). Fig. 3-2(a) is a cross-sectional image of Ni-GDCjGDCjPBCCF05 with an overview of the three layers, showing the thickness of ~20 μm for cathode and ~15 μm for the electrolyte. All three components

seem to be well-connected and the electrolyte is dense enough without detectable pores or cracks. The microstructure of the PBCCF cathodes prepared by the screen printing on the GDC electrolyte is shown in Fig. 3-2 (b) - (d). Since the microstructures of all PBCCF cathodes are similar, microstructure does not seem to change significantly by Fe doping.

Table 3-2 Space group and lattice parameters of PBCCFs.

Properties	Samples		
	PBCCO	PBCCF05	PBCCF10
Space group	*P4/mmm*	*P4/mmm*	*P4/mmm*
a (Å)	3.885	3.871	3.877
c (Å)	7.634	7.703	7.762
V (Å^3)	115.232	115.421	116.683
Oxygen contents (5+δ)	5.75	5.81	5.97
Pr			
x	0.0000	0.0000	0.0000
y	0.0000	0.0000	0.0000
z	0.5000	0.5000	0.5000
Ba/Ca			
x	0.0000	0.0000	0.0000
y	0.0000	0.0000	0.0000
z	0.0000	0.0000	0.0000
Co/Fe			
x	0.5000	0.5000	0.5000
y	0.5000	0.5000	0.5000
z	0.2513	0.2518/0.2597	0.2539/0.2538
O1			
x	0.5000	0.5000	0.5000
y	0.5000	0.5000	0.5000
z	0.0000	0.0000	0.0000
O2			
x	0.0000	0.0000	0.0000
y	0.5000	0.5000	0.5000
z	0.2353	0.2741	0.2254
O3			
x	0.5000	0.5000	0.5000
y	0.0000	0.0000	0.0000
z	0.2899	0.2233	0.2995
O4			
x	0.5000	0.5000	0.5000
y	0.5000	0.5000	0.5000
z	0.5000	0.5000	0.5000

Fig. 3-3 shows the TGA curves of PBCCF samples as a function of temperature in air. The initial oxygen contents at room temperature were obtained by iodometric titration. All PBCCFs start to lose oxygen at

T > 200 ºC from the lattice along with the reduction of Fe^{3+}/Fe^{4+} and Co^{3+}/Co^{4+}.[11] The degree of oxygen loss decreases with increasing Fe amount at given temperature because the stronger Fe-O bond compared to the Co-O bond retains the oxygen loss on heating.[2] Also, as shown in Table 3-2, the initial oxygen contents increase from 5.75 to 5.97 with increasing Fe substitution.

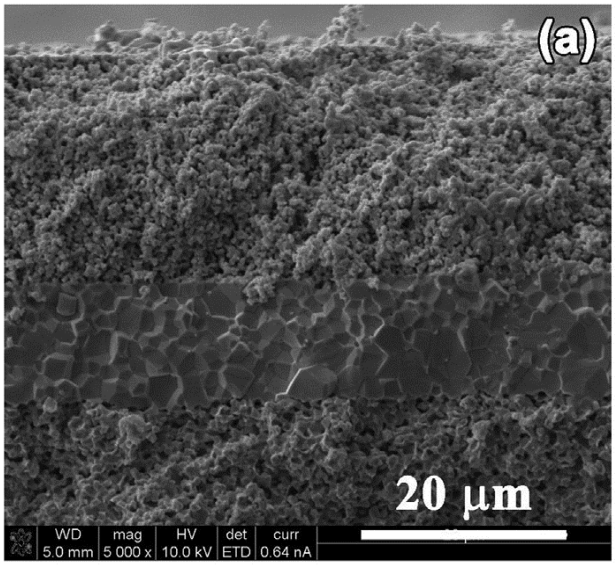

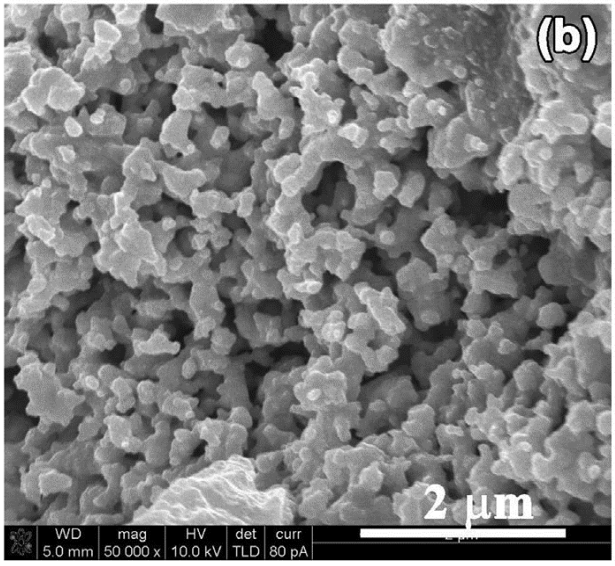

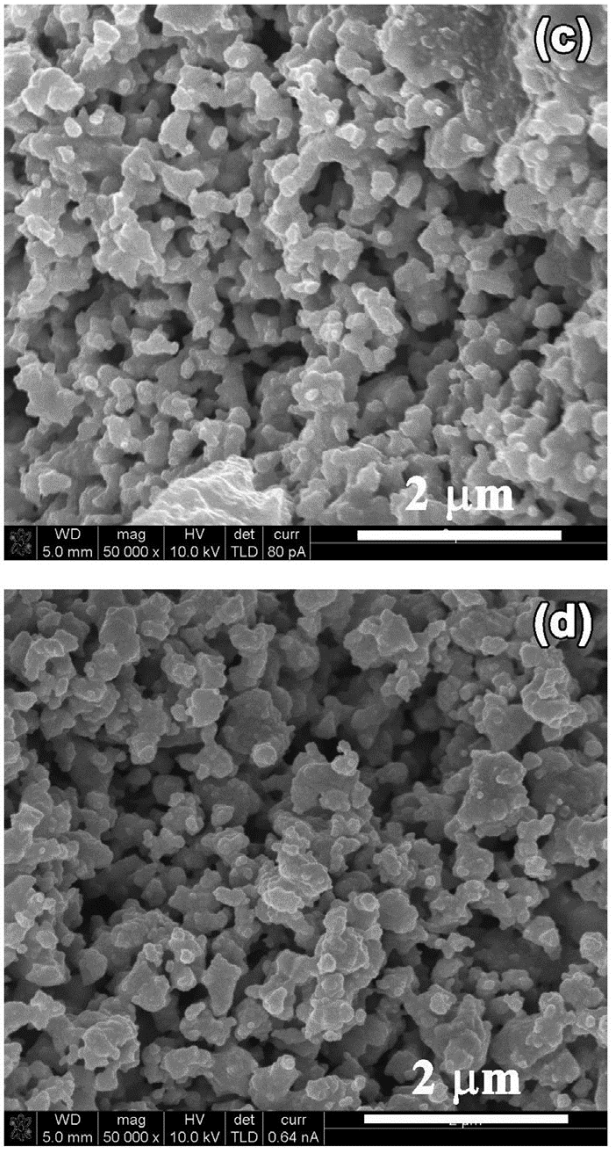

Fig. 3-2. (a) Cross-sectional SEM image of PBCCF05 and SEM images of (b) PBCCO, (c) PBCCF05, and (d) PBCCF10 cathodes

Fig. 3-4 shows the temperature-dependent electrical conductivity of PBCCFs in air. The conductivity of the PBCCO increases with decreasing the temperature, exhibiting typical metallic conduction behavior because of the reduction of the charge carrier concentration, $Co_{Co}^{\cdot}$, accompanied by the oxygen loss as mentioned in TGA results.[11] As described in the *pseudo*-chemical reaction below, the hole is the majority charge carrier of the cobalt-based perovskite as shown in Eq. 2-1. The reduction of the Co^{4+} to Co^{3+} by the oxygen loss results in a decrease of the hole charge carrier and consequently a

decrease of the conductivity.[9] At the given temperature, the conductivity of PBCCF increases with decreasing Fe concentration, and this behavior is due to a decrease in the covalency of the (Co-Fe)-O bond.[21,22] The electrical conductivity of the Fe-doped sample shows a metal-insulator (M-I) transition behavior at a temperature above 300 ºC. Further increasing temperature above 300 ºC, the electrical conductivity decreases due to the increase in oxygen loss.[24]

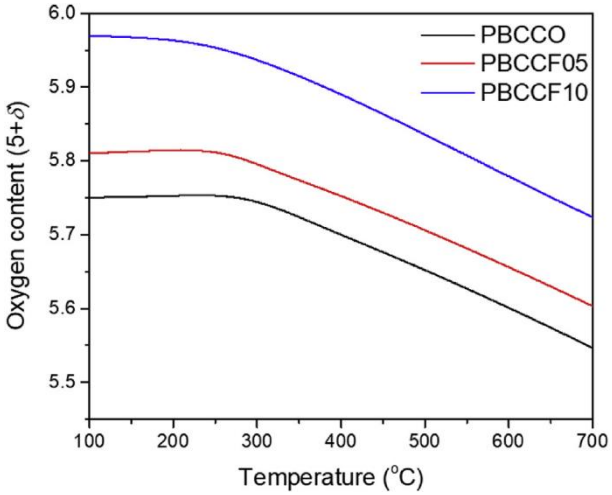

Fig. 3-3. TGA curves of PBCCFs

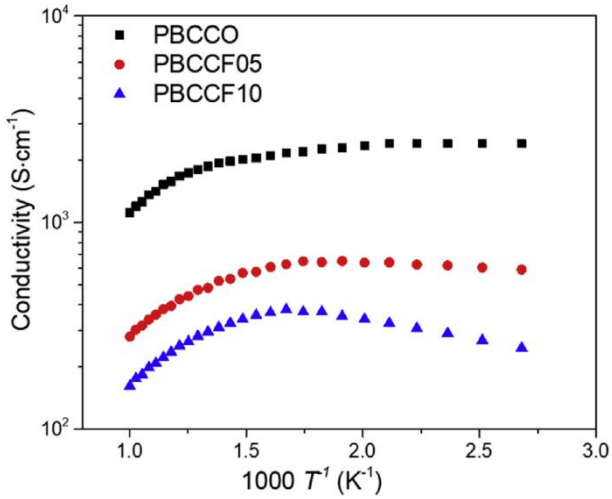

Fig. 3-4. Conductivity results of PBCCFs

As shown in the *in-situ* XRD results (Fig. 3-1(c)), the main diffraction peaks shift to lower 2 θ values with increasing temperature, suggesting that the volume of the unit cell increases. The volume of the lattice can be obtained from the XRD peak of 2 θ values using Bragg's law and the thermal expansion coefficient can be calculated by lattice volume change.[23] Fig. 3-5 shows the lattice volume changes of PBCCO and PBCCF05 and their corresponding TECc in the temperature range of 100 ºC ~ 700 ºC. The TECs with a low temperature range of 100 ºC ~ 400 ºC of the PBCCFs are similar (19.18 × 10^{-6} K^{-1}, 19.28 × 10^{-6} K^{-1}, and 19.38 × 10^{-6} K^{-1} for PBCCO, PBCCF05, and PBCCF10, respectively) meaning that effect of Fe doping on thermal expansion at low temperature is negligible. The TECs with a temperature range of 400 ºC ~ 700 ºC of PBCCO, PBCCF05, and PBCCF10 are 23.28 × 10^{-6} K^{-1}, 20.28 × 10^{-6} K^{-1}, and 17.95 × 10^{-6} K^{-1}, respectively, indicating that TEC decreases by Fe doping. Generally, the large thermal expansion of the cobalt-based perovskite oxides mainly comes from the large ionic radius of Co^{3+} compared to Co^{4+} that formed during the reduction of Co^{4+} to Co^{3+} by oxygen loss.[3,11,15] Therefore, minimizing the oxygen loss and decreasing the Co^{3+} cation content in the perovskite lattice are the key factors to decrease the TEC. In Fe substituted samples, the oxygen loss is predominantly compensated by the formation of Fe^{3+} rather than reduction of Co^{4+} to Co^{3+}. [2]

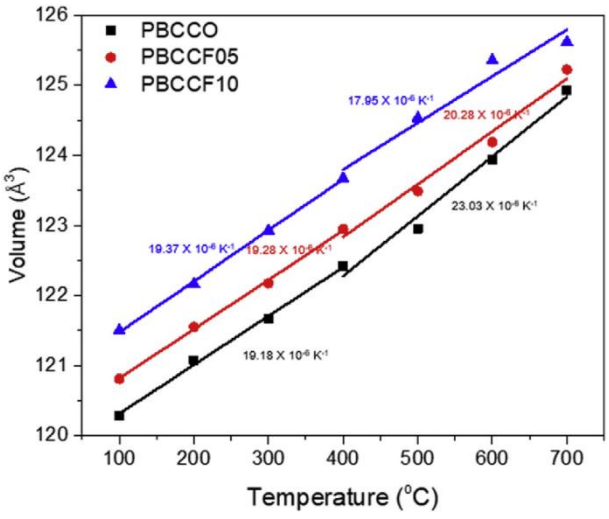

Fig. 3-5. Thermal expansion coefficients of PBCCFs

3.3.2. Electrochemical properties

The ASR of PBCCF is obtained at 600 ºC by AC impedance spectroscopy with PBCCF|GDC|PBCCF symmetric cells. The ASR values are determined by the intercept between the high and low frequencies arcs on the real axis of the Nyquist plot, which can be expressed as the sum of the charge transfer resistance and the non-charge transfer resistance. In the Nyquist plots, the high frequency (R_2) arc corresponds to charge transfer caused by the migration and diffusion of oxygen ion from the TPB into the electrolyte lattice.[24] On the other hand, low frequency (R_3) arc is equivalent to non-charge/transfer including oxygen surface exchange, solid-state diffusion, and inner/outer gas-phase diffusion. [25] The polarization resistance (R_p) of the cathodes is defined by the sum of R_2 and R_3. The experimental impedance spectra and fitted equivalent circuit model (inset) are presented in Fig. 3-6 (a). The impedance values at 600 ºC with various Fe content were summarized in Table 3-3.

Table 3-3. Summary of the impedance spectra of PBCCF cathodes at 600 ºC

Sample	R_2 (Ω cm^2)	R_3 (Ω cm^2)	R_p (Ω cm^2)
PBCCO	0.062	0.138	0.200
PBCCF05	0.045	0.035	0.080
PBCCF10	0.059	0.042	0.101

The R_p values of PBCCO, PBCCF05, and PBCCF10 at 600 ºC are 0.200, 0.080, and 0.101 Ω cm^2, respectively. Both R_2 and R_3 are decreased with Fe substitution due to the higher concentration of the mobile oxygen species in the [Pr-O] plane, which could be responsible for faster oxygen kinetics.

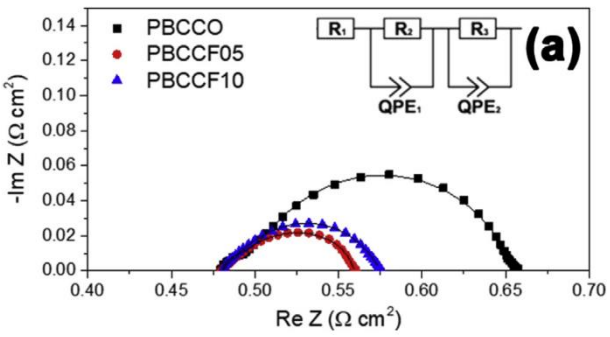

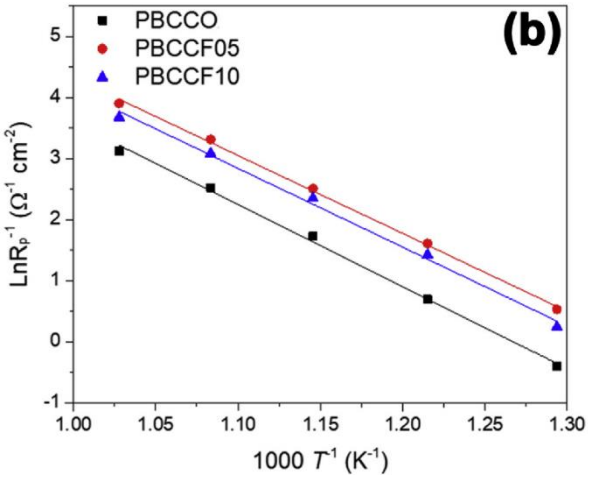

Fig. 3-6. (a) Experimental and fitted impedance spectra at 600 °C and (b) Arrhenius plots of PBCCFs cathode on GDC electrolyte in a symmetric cell

However, too high concentration of Fe can inhibit the oxygen kinetics because too strong Fe-O bonding strength interferes with the attachment and release of mobile oxygen from oxygen lattice in the mobile oxygen channel. [2,14] From the previous studies, the population of mobile oxygen species in the [Pr-O] planes could contribute to improved oxygen kinetics associated with oxygen bulk diffusion and surface exchange.[2,3,7,9-11,13-17,26] Arrhenius plots of the ASR for PBCCF are shown and summarized in Fig. 3-6 (b) and Table 3-4.

Table 3-4. Summary of activation energy of PBCCF

Sample	Activation energy (kJ mol^{-1})		
	R_2	R_3	R_p
PBCCO	129.949	90.742	110.366
PBCCF05	113.492	89.399	105.379
PBCCF10	120.619	91.181	107.264

From these ASR values, the apparent activation energies of PBCCO, PBCCF05, and PBCCF10 are calculated as 110.37 kJmol^{-1}, 105.38 kJ mol^{-1}, and 107.26 kJ mol^{-1}, respectively. The activation energy of PBCCF05 is lower than that of PBCCO and PBCCF10. The lower activation energy of PBCCF05

can be realistic evidence of the superior oxygen kinetic of PBCCF05. Interestingly, activation energies for non-charge transfer of PBCCFs are similar (R_3), and the difference in the activation energy of R_p occurred only in the charge transfer reaction (R_2). This result suggests that the Fe doping effect does not affect non-charge transfer such as gas diffusion, but only charge transfer such as surface exchange and oxygen reduction reaction. Anode supported single cell (cell configuration of Ni-GDC|GDC|PBCCFs-GDC) with a 15 μm thickness GDC electrolyte and Ni-GDC anode support was used to evaluate electrochemical performance of PBCCO-GDC and PBCCF05-GDC. Humidified H_2 (3% H_2O) as fuel and ambient air as oxidant are supplied to anode and cathode, respectively. Fig. 3-7 (a) shows *I-V* curves and corresponding power density curves of the single-cell for PBCCF05. Fig. 3-7 (b) shows the electrochemical impedance spectra of the PBCCF05 cell corresponding to the *I-V* curve under the OCV condition. Table 3-5 summarizes the electrochemical performance of PBCCO and PBCCF05 fuel cells at 500 ºC ~600 ºC. The maximum power densities of PBCCO and PBCCF05 are 1.82 W cm^2 and 1.89 W cm^2 at 600 ºC, respectively.

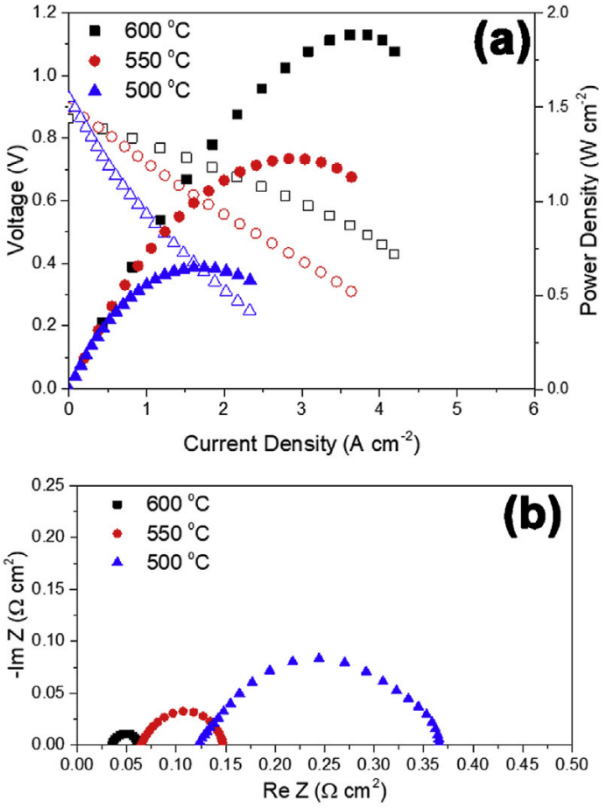

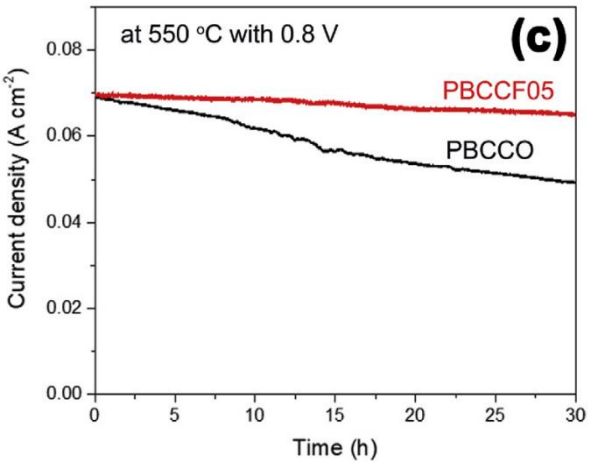

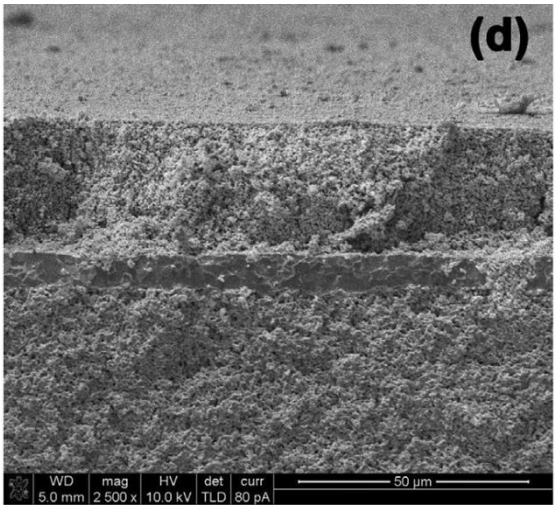

Fig. 3-7. (a) I-V curves and corresponding power densities and (b) impedance spectra of Ni-GDC|GDC|PBCCF05, (c) single cell and stability test at 550 °C with 0.8 V of PBCCO and PBCCF05 single cell, and (d) SEM image of the PBCCF05-GDCjGDCjNi-GDC single cell

The single-cell performance is enhanced with doping Fe and is consistent with the trend of the ASR and the electrical conductivity results. The stability test with PBCCF05(PBCCO)-GDC|GDC|Ni-GDC single-cell was conducted under a constant current density of - 0.8 V and humidified H_2 (3% H_2O) as fuel and dry air as an oxidant at 550 °C, as shown in Fig. 3-7 (c). The PBCCF05 single cell shows more than 30 h stable performance while PBCCO single cell gets severe degradation.

Table 3-5. Summary of the single-cell test results of PBCCO and PBCCF05

Sample	Temp (°C)	R_o (Ω cm^2)	R_p (Ω cm^2)	Rt (Ω cm^2)	Maximum power density (W cm^{-2})
PBCCO	600	0.037	0.038	0.076	1.822
	550	0.067	0.103	0.170	1.148
	500	0.118	0.289	0.407	0.605
PBCCF05	600	0.034	0.031	0.065	1.890
	550	0.063	0.083	0.146	1.227
	500	0.122	0.245	0.367	0.646

The Fe doping on the Co site of PBCCO can enhance the stability because stronger Fe-O bonding as compared with CoeO bonding provides higher redox and chemical stability. [27] Fig. 3-7 (d) presents an SEM image of PBCCF05-GDC|GDC|Ni-GDC single-cell after electrochemical evaluation. There is no detectable change after measurement from the SEM image. Conclusively, PBCCF05 is a promising cathode material for IT-SOFC with improved electrochemical performance and thermal stability. It also shows satisfactory electrical conductivity and thermal expansion as well as long-term stability behavior under practical fuel cell operating conditions.

3.4. Conclusion

The effect of partial substitution of Fe in $PrBa_{0.8}Ca_{0.2}Co_2O_{5+\delta}$ layered perovskite oxide has been studied as a potential cathode material for IT-SOFCs. Structural properties, thermal expansion behavior, electrical conductivities, and electrochemical performance were investigated in this study. The in situ XRD spectra on $PrBa_{0.8}Ca_{0.2}Co_{1.5}Fe_{0.5}O_{5+\delta}$ sample from room temperature to 700 °C show no structural change occurred. The Electrical conductivity increases with decreasing Fe substitution from 197 S to 1361 S cm1 at 600 °C, which reaches the general required value for IT-SOFC cathode. The optimized $PrBa_{0.8}Ca_{0.2}Co_{1.5}Fe_{0.5}O_{5+\delta}$ cathode shows lowest polarization resistance value of 0.080 Ω cm^2 and remarkable fuel cell performance of 1.89 W cm^2 at 600 C. Moreover, $PrBa_{0.8}Ca_{0.2}Co_{1.5}Fe_{0.5}O_{5+\delta}$ presents a low thermal expansion coefficient and long-term stability under practical fuel cell operating conditions mainly due to stronger.

References

[1] S. Sengodan, S. Choi, A. Jun, T. H. Shin, Y. -W. Ju, H. Y. Jeong, J. Shin, J. T. S. Irvine, and G. Kim, *Nat Mater*, 2014, **14**, 205-209.

[2] J. Kim, A. Jun, J. Shin, and G. Kim, *J. Am. Ceram. Soc.*, 2014, **97,** 651-656.

[3] S. Joo, J. Kim, J. Shin, T. H. Lim, and G. Kim, *J. Electrochem. Soc.*, 2016, **163,** F1489-F1495.

[4] B. C. H. Steele, A. Heinzel, Nature, 2001, **414**, 345-352.

[5] B. C. H. Steele, *J. Mater. Sci.*, 2001, **36**, 1053-1068.

[6] S. Park, S. Choi, J. Shin, and G. Kim, *J. Power Sources*, 2012, **210**, 172-177.

[7] C.Kim, J. Shin, and G. Kim, *Int. J. Hydrogen Energy*, 2011, **39**, 20812-20818.

[8] S. Yoo, A. Jun, Y. -W. Ju, D. Odkhuu, J. Hyodo, H. Y. Jeong, N. Park, J. Shin, T. Ishihara, and G. Kim, *Angew. Chem. Int. Ed.*, 2014, **53**, 13064-13067.

[9] S. Choi, S. Park, J. Shin, and G. Kim, *J. Mater. Chem. A*, 2015, **3**, 6088-6095.

[10] S. Kim, A. Jun, O. Kwon, J. Kim, S. Yoo, H. Y. Jeong, J. Shin, G. Kim, *ChemSusChem,* 2015, **8**, 3153-3158.

[11] C. Lim, A. Jun, H. Jo, K. M. Ok, J. Shin, Y. -W. Ju, and G. Kim, *J. Mater. Chem. A*, 2016, **4**, 6479-6486.

[12] G. Kim, S. Wang, A. J. Jacobson, Z. Yuan, W. Donner, C. L. Chen, L. Reimus, P. Brodersen, and C. A. Mims, *Appl. Phys. Lett.*, 2006, **88**, 204103.

[13] A. Jun, T. -H. Lim, J. Shin, and G. Kim, *Int. J. Hydrogen Energy*, 2014, **39**, 20791-20798.

[14] S. Choi, S. Yoo, J. Kim, S. Park, A. Jun, S. Sengodan, J. Kim, J. Shin, H. Y. Jeong, Y. Choi, M. Liu, and G. Kim, *Sci. Rep*., 2013, **3**, 2426.

[15] A. Jun, S. Yoo, Y. -W. Ju, J. Hyodo, S. Choi, H. Y. Jeong, J. Shin, T. Ishihara, T. -H. Lim, and G. Kim, *J. Mater. Chem. A*, 2015, **3**, 15082-15090.

[16] D. S. Tsvetkov, I. L. Ivanov, I. V. Urusov, A. Yu Zuev, *Thermochimica Acta*, 2011, **519**, 12-15.

[17] S. Park, S. Choi, J. Shin, and G. Kim, *Electrochim. Acta*, 2014, **125**, 683-690.

[18] A. Jun, J. Shin, and G. Kim, *Phys. Chem. Chem. Phys.*, 2013, **15**, 19906-19912.

[19] J. Kim, S. Choi, S. Park, C. Kim, J. Shin, and G. Kim, *Electrochim. Acta*, 2013, **112**, 712-718.

[20] B. H. Toby and R. B. Dreele, *J. appl. Cryst*, 2013, **46**, 544-549.

[21] G. W. Rathernau and J. B. Goodenough, *J. Appl. Phys.*, 1968, **39**, 403-411.

[22] Y. Matsumoto, S. Yamada, T. Nishida, and E. Sato, *J. Electrochem. Soc.*, 1980, **127**, 2360-2364.

[23] M. Nakayama, H. Ikuta, Y. Uchimoto, and M. Wakihara, *J. Mater. Chem.*, 2002, **12**, 1500-1504.

[24] S. Park, S. Choi, J. Shin, and G. Kim, *RSC Adv*., 2014, **4**, 1775.

[25] S. Choi, S. Park, J. Kim, T. -H. Lim, J. Shin, G. Kim, *Electrochem. Commun.*, 2013, **34**, 5-8.

[26] S. Yoo, S. Choi, J. Kim, J. Shin, and G. Kim, *Electrochim. Acta*, 2013, **100**, 44-45.

[27] S. Choi, J. Shin, and G. Kim, *J. Power Sources*, 2012, **201,** 10-17.

Chapter 4. Energy conversion (3): Ca and Ni-doped $Pr_{0.5}Ba_{0.5}FeO_{3-\delta}$ as a highly active and robust cathode for high-temperature solid oxide fuel cell

4.1. Introduction

Since concerns about pollution, global warming, and energy depletion have seriously increased, the demands for eco-friendly and sustainable fuel/devices are accelerating to replace the combustion systems.[1,2] Solid oxide fuel cells (SOFCs) can be considered as leading electrochemical energy conversion devices to provide clean and highly efficient energy.[3,4] Most commercial SOFC systems are now operating based on yttria-stabilized zirconia (YSZ) electrolyte supported cells to secure manufacturing convenience, cost effect, and mechanical/chemical stability.[5,6] Despite these attractive features of the electrolyte support system, a huge ohmic loss is induced by a very thick YSZ electrolyte layer. Therefore, the operating temperature should be increased up to a high-temperature range (800~1000 ºC) to minimize the resistance from thick YSZ electrolyte.

Due to their high operating temperature, $La_{1-x}Sr_xMnO_{3-\delta}$ (LSM) is commonly used as a cathode material on the basis of its robust thermal stability, sufficient electronic conductivity, and non-reactivity with YSZ.[7,8] However, LSM is electronically conductive but ionically insulating, and thus the electrochemical reaction area is limited to the triple-phase boundary (TPB) where the electronic conductor, ionic conductor, and gas meet simultaneously. This single electronically conductive property strongly affected the limitation of electrocatalytic oxygen reduction reaction (ORR) activities, consequently resulting in a poor fuel cell performance. In this regard, it is necessary to develop new cathodes as mixed ionic and electronic conductors (MIECs) to adequately replace the conventional LSM cathode in commercial SOFC system conditions.

Recently, Fe-based MIEC perovskite oxides have been widely investigated as alternative cathode materials due to their excellent electronic/ionic conductivity and sufficient catalytic activities toward ORR.[9,10] In other words, these materials can effectively extend the electrochemical reaction sites by the migration of oxygen species through the bulk as well as the entire surface of materials. Although

Fe-based perovskite oxides exhibit excellent electrochemical properties, high fabricating and operating temperatures due to the electrolyte supported system lead to severe electrochemical degradation by particle coarsening.

Thus, partially substituting appropriate dopant ions on either A and/or B sites of perovskite structures are widely adopted to solve this critical issue or obtain the desired properties. As a means of providing a coarsening tolerance and thermal stability under high-temperatures, various transition metal ions have been introduced into the B-site. Interestingly, Ni additive is known as a sintering agent to provide better adhesion between grains, but the Ni dopant provides thermal stability by improving the coarsening tolerance.[11-15] Additionally, many studies have found that Ca doping into the A site in perovskite structure could improve electrical conductivity as well as thermal/chemical stability by the substitution of smaller divalent ions.[16-18]

These findings motivated us to demonstrate a strategic effect on Ca and Ni doping in Fe-based MIEC perovskite cathode, $Pr_{0.5}Ba_{0.5}FeO_{3-\delta}$ (PBF). This study focuses on finding an alternative to commercial LSM cathode with excellent electrochemical performance and thermal/chemical durability. The microscopically analysed thermal stability presents that doping Ni provides robust thermal stability during fabrication and operation by improving coarsening tolerance at high temperatures. Therefore, newly developed cathode, Ca and Ni coped PBF can be considered as an alternative of commercial LSM cathode for high-temperature SOFC.

4.2. Experimental procedure

4.2.1. Synthesis and fabrication

The $Pr_{0.5}Ba_{0.3}Ca_{0.2}Fe_{1-x}Ni_xO_{3-\delta}$ (x = 0, 0.1, 0.2, and 0.3) cathode powders were synthesized by a conventional sol-gel combustion method, the Pechini method. Calculated amounts of $Pr(NO_3)_3 \cdot 6H_2O$ (Sigma-Aldrich, 99.9%, metal basis), $Ba(NO_3)_2$ (Sigma-Aldrich, 99+%), $Ca(NO_3)_2 \cdot 4H_2O$ (Alfa Aesar, 99.98%), $Fe(NO_3)_3 \cdot 9H_2O$ (Sigma-Aldrich, ≥98%), and $Ni(NO_3)_2 \cdot 6H_2O$ (Sigma-Aldrich, 99+%) were added with proper amounts of citric acid and ethylene glycol (Sigma-Aldrich, average Mn 400) into D.I

water and were stirred until completely dissolved. The dissolved solutions were heated at 250 ºC on a hot plate until it was spontaneously combusted. The combusted ashes were collected and calcined at 600 ºC for 2 h to remove the combustion residue. The calcined powders were heat-treated at 1300 ºC for 4 h to form a perovskite phase and then ball-milled for 24 h to decrease the particle size. The ball-milled powders were mixed with $Ce_{0.9}Gd_{0.1}O_{1.95}$ (GDC) powder by the ball-milling process to prepare composite cathode powders. The acronyms of synthesized powders are summarized in Table 4-1. The YSZ electrolyte supported cells with the GDC buffer layer were fabricated by a conventional pressing method and drop coating method. 0.4 g of YSZ powder was pressed into 20 mm diameter pellet at a pressure of 2 tons for 1 min and then pre-sintered at 800 ºC for 2 h. The GDC buffer layer was coated on both sides of the YSZ electrolyte by a drop coating method. The GDC slurry for drop coating was prepared by dispersing the GDC powder into an ethanol base solution containing a small amount of dispersant (triethanolamine, Alfa Aesar), binder (polyvinyl Butyral, B-98), and plasticizers (polyalkylene glycol and Benzyl Butyl Phthalate). The GDC drop coating slurry was dripped onto the pre-sintered YSZ pellet and sintered at 1400 ºC for 2 h. PBCFNi-GDC cathodes were screen printed onto both sides of GDC|YSZ|GDC electrolyte supported cell. The prepared cathode powders and GDC electrolyte were mixed with an ink vehicle (Heraeus V006) using mortar and pestle. The prepared cathode pastes were screen printed, dried in room temperature, and sintered at 1200 ºC for 2 h, the usual fabrication temperature of LSM cathode.[19-23]

Table 4-1 Summary of synthesized powders

Chemical composition	Acronym
$Pr_{0.5}Ba_{0.3}Ca_{0.2}FeO_{3-\delta}$	PBCF
$Pr_{0.5}Ba_{0.3}Ca_{0.2}Fe_{0.9}Ni_{0.1}O_{3-\delta}$	PBCFNi10
$Pr_{0.5}Ba_{0.3}Ca_{0.2}Fe_{0.8}Ni_{0.2}O_{3-\delta}$	PBCFNi20
$Pr_{0.5}Ba_{0.3}Ca_{0.2}Fe_{0.7}Ni_{0.3}O_{3-\delta}$	PBCFNi30

4.2.2. Characterization

The crystal structures of the synthesized powders were characterized by X-ray diffractometer (XRD; AXS D8 Advance diffractometer, Bruker) using Cu Kα radiation with a scanning speed of 2 ° min^{-1}.

The SiO_2 (DAEJUNG, extra pure) power was used as a reference to calibrate the peak positions. The chemical compatibilities between cathode and electrolyte were tested using XRD analysis with a heat-treated mixture of cathode and electrolyte at 1200 ºC for 2 h. The microstructures of PBCFNi-GDC composite cathodes were observed using scanning electron microscopy (SEM; Nova Nano SEM, FEI). The oxygen vacancy and oxidation states of B-site (Fe and Ni) were evaluated by iodometric titration and X-ray photoelectron spectroscopy (XPS; K-alpha system, ThermoFisher). The electrochemical properties of PBCFNi-GDC composite were evaluated by electrochemical impedance spectra using a symmetrical cell of PBCFNi-GDC|GDC|YSZ|GDC| PBCFNi-GDC configuration at 850 ºC. The platinum mesh was attached with platinum paste to be used as a current collector. Long-term stabilities of PBCFNi-GDC composite cathodes were measured by the time-dependence impedance spectra test using a symmetrical cell at 850 ºC.

4.3. Results and discussion

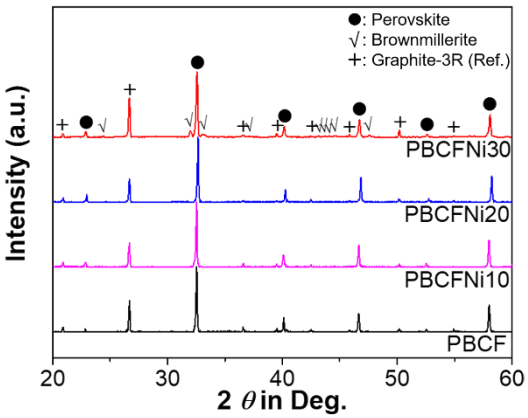

Fig. 4-1. XRD patterns of PBCFNi powders (heated at 1300 ºC for 4 hr)

The powder X-ray diffraction patterns of PBCFNi are displayed in Fig. 4-1. The PBCF, PBCFNi10, and PBCFNi20 show a single perovskite phase without the detectable impurity or secondary phases. Moreover, the peaks are slightly shifted toward higher 2 θ with increasing Ni contents. Based on followed Bragg`s equation (Eq. 4-1), higher 2 θ peaks represent smaller d-space.[17]

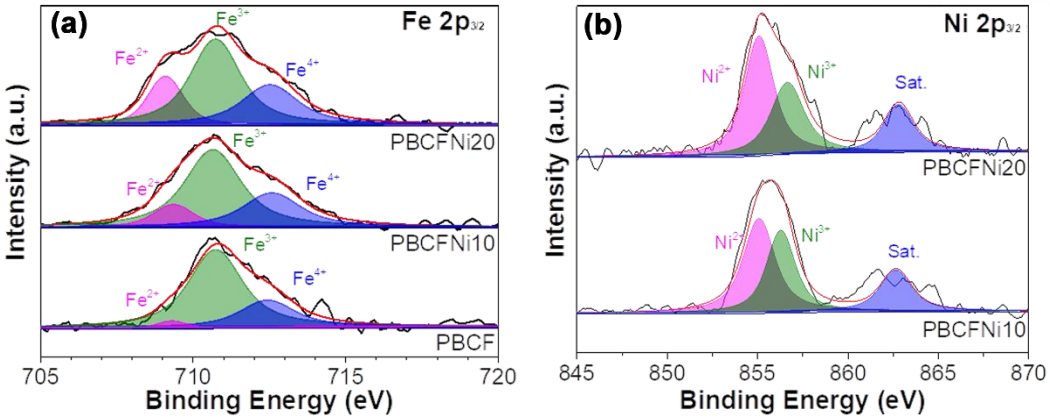

Fig. 4-2. Deconvoluted XPS spectra of (a) Fe $2p_{3/2}$ and (b) Ni $2p_{3/2}$ of PBCF, PBCFNi10, and PBCFNi20

The Bragg`s equation is expressed as

$$d = \frac{n\lambda}{sin\theta} \qquad \text{Eq. 4-1}$$

where d is the distance of interplanar, n is a positive integer, λ is the wavelength of x-ray source (Cu $K\alpha$ = 1.54 Å), θ is scattering angle. The decreased lattice parameter of PBCFNi by doping Ni can be explained by the oxidation state of B-site.

Fig. 4-2 (a) and (b) present deconvoluted spectra of Fe $2p_{3/2}$ and Ni $2p_{3/2}$. As shown in Fig. 4-2 (a), the XPS spectra of Fe $2p_{3/2}$ are deconvoluted into three different peaks at the binding energies of ~709.2 eV, ~710.4 eV, and ~712 eV, corresponding to Fe^{2+}, Fe^{3+}, and Fe^{4+}, respectively.[24] As shown in table 4-2, the amount Fe^{2+} are increased (3%, 12 %, and 19 % for PBCF, PBCFNi10, and PBCFNi20, respectively) and Fe^{3+} are decreased (72 %, 60 %, and 53 % for PBCF, PBCFNi10, and PBCFNi20, respectively) with increasing lower valence Ni. The decrease of relatively larger size Fe^{3+} (0.79 Å) and the increase of smaller size Fe^{2+} (0.75 Å) can be contributed to the reduction of the size of B-site, consequently resulting in a decrease of the lattice parameter.[25] The XPS spectra of Ni 2p3/2 of PBCFNI10 and PBCFNi20 are also deconvoluted into two different peaks at the binding energies of ~854 eV and ~856 eV, corresponding to Ni^{2+} and Ni^{3+}, respectively. The amounts of Ni^{2+} of PBCFNi10 and PBCFNi20 are 56 % and 60 %, respectively. Although concentration of larger size Ni^{2+} (0.83 Å) as

compared to Ni^{3+} (0.70 Å) is increased with increasing Ni, the calculated B-site size is decreased with increased amount of Ni (0.7691 Å, 0.7651 Å, and 0.7647 Å for PBCF, PBCFNi10, and PBCFNi20, respectively) because the effect of reduced size by increase of large size Fe^{3+} is much higher than the effect of increased size by increasing Ni^{2+}.

Table 4-2 Summary of deconvoluted XPS results of PBCF, PBCFNi10, and PBCFNi20

Sample	Fe (%)			Ni (%)		The calculated size of B-site cation (Å)	Oxygen contents ($3-\delta$)
	Fe^{2+}	Fe^{3+}	Fe^{4+}	Ni^{2+}	Ni^{3+}		
PBCF	3	72	25	-	-	0.7691	2.86
PBCFNi10	12	60	28	56	44	0.7651	2.79
PBCFNi20	19	53	28	60	40	0.7647	2.72

The reduced B-site size with increasing Ni contents causes decreasing lattice parameter of PBCFNi, which can be a reason for higher shifted 2 θ peaks in XRD results. [26] While other samples show only a single perovskite phase, PBCFNi30 has a brownmillerite phase as well as a perovskite phase.[27] The brownmillerite oxides are known to have slightly high ionic conductivity and suppressed thermal expansion, so they may enhance the thermal stability without electrochemical degradation.[27,28] The cathodes and the electrolytes must be chemically stable because the chemical reactions between them can generally increase the resistance and deteriorate the electrochemical properties by forming insulating secondary phases at the interface.[29-31]

Fig. 4-3 exhibits the chemical compatibility study of PBCFNi with YSZ and GDC electrolyte. For compatibility study, PBCFNi cathodes were mixed with YSZ and GDC electrolytes using mortar and pestle, respectively, and then were heat-treated at 1200 ºC (fabrication temperature of cathode). All PBCFNi chemically react with the YSZ electrolyte and form $BaZrO_3$. (Fig. 4-3 (a))

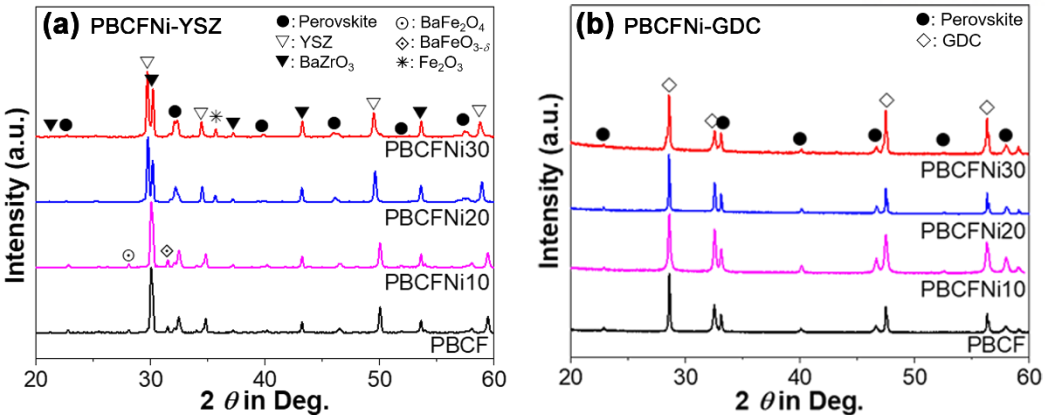

Fig. 4-3. Reactivity study of PBCFNi with (a) YSZ and (b) GDC (heat-treated at 1200 ºC)

The reaction between YSZ and PBCF and PBCFNi10 forms $BaFe_2O_4$ and $BaFeO_3$ impurities in addition to $BaZrO_3$ impurity.[32-34] The PBCFNi20 and PBCFNi30 show Fe_2O_3 (PDF# 39-1346) impurity instead of $BaFe_2O_4$ and $BaFeO_3$ impurities. On the other hand, all PBCFNi are chemically stable with GDC as shown in Fig. 4-3 (b). Therefore, it is necessary to use GDC buffer layer to prevent chemical reaction between PBCFNi cathodes and YSZ electrolyte. The electrochemical performance of cathodes is highly influenced by micro-structure because it can affect reaction kinetics, charge/non-charge transfer reaction, and gas diffusion.[35,36] Smaller particle size and proper pore structure can improve the electrochemical performance by increasing the length of the TPB and enhancing gas diffusion.[37] The SEM images of as-fabricated (at 1200 ºC for 2 h) and post-heat treated (at 850 ºC for 200 h) PBCFNi-GDC are displayed in Fig. 4-4 (a) - (d). As shown in SEM images of as-fabricated PBCFNi-GDC, un-doped PBCF-GDC cathode shows highly agglomerated particles with insufficient pores, resulting in insufficient electrocatalytic active sites and gas diffusion.[38] On the other hand, Ni-doped PBCF has smaller size particles and increased pores as shown in SEM images of as-fabricated PBCFNi-GDC (left side of Fig 4-4 (a) – (d)).

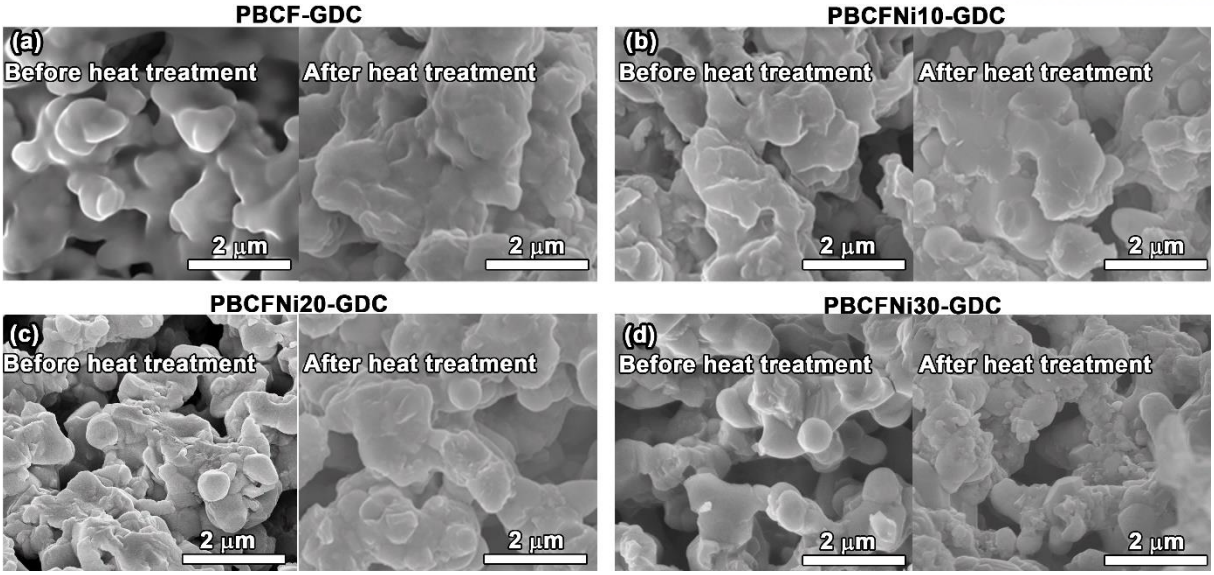

Fig. 4-4. SEM images of as-fabricated (left) at 1200 ºC for 2 hr and post-heat treated (right) at 850 ºC for 200 hr (a) PBCF-GDC, (b) PBCFNi10-GDC, (c) PBCFNi20-GDC, and (d) PBCFNi30-GDC

The improved microstructure (particle size and pore structure) can be attributed to prevented coarsening by Ni doping. [12–14] This coarsening prevention can be explained by increased oxygen vacancy and cation vacancy with an increase in the amount of Ni. The relatively low valence Ni^{2+} into Fe sites increases oxygen vacancies, as shown in Table 4-2. As Schottky-type defect, the increased oxygen vacancy also increases the cation vacancy which can retard the grain growth and coarsening by the prevention of cation diffusion. [13,15] The prevented grain growth can be confirmed by calculated crystalline size using the *Debye-Scherrer* equation (Eq. 4-2). The *Debye-Scherrer* equation is given as

$$D = \frac{K\lambda}{B\sin\theta} \qquad \text{Eq. 4-2}$$

where D is the mean crystalline size, K is a numerical factor referred to as the crystallite-shape factor (≈ 0.93), λ is the wavelength of the X-ray (Cu Kα = 0.1541 Å), β is the full-width at half maximum of the X-ray diffraction peak in radian, and θ is the Bragg angle.[39] The calculated crystalline sizes of the PBCF, PBCFNi10, PBCFNi20, and PBCFNi30 (perovskite only) are 73.88 nm, 68.96 nm, 59.99 nm, and 52.77 nm, respectively. The retarded grain growth of the PBCF by doping Ni can provide coarsening tolerance during fabrication and operation. In order to demonstrate the long-term stability,

as-fabricated PBCFNi-GDC were heat-treated at an operating temperature of 850 ºC for 200 h and observed microstructure by SEM. All samples show agglomerated particles with reduced pores after 200 h post-heat-treatment. Especially, un-doped PBCF-GDC shows highly agglomerated particles with insufficient pores. Similar to the SEM results of as-fabricated PBCFNi-GDC, increased Ni concentration decreases the agglomeration of particles during long-term heat treatment by preventing coarsening. Particularly, PBCFNi30-GDC shows a small particle size and a proper pore structure as compared with other samples, which can be expected to have outstanding long-term stability. The electrocatalytic activity for ORR of the composite cathode was evaluated by electrochemical impedance spectra (EIS) using a symmetrical cell under open-circuit voltage (OCV). Fig. 4-5 (a) presents a cross-sectional image of PBCFNi30-GDC|GDC|YSZ symmetrical cell. The cathode and the electrolyte are well connected without any detectable delamination and/or crack. The GDC buffer layer and the YSZ electrolyte are dense enough to be used as an electrolyte, and the PBCFNi30-GDC cathode has enough pore for gas diffusion and proper thickness of 10 μm. In the EIS results, the difference between the low intercept and the high intercept of the real axis of the Nyquist plot is considered as cathodic polarization resistance.[40] The EIS results are summarized in Table 4-3 As shown in Fig. 4-5 (b), un-doped PBCF-GDC cathode indicates a very high polarization resistance of 0.24 Ω cm^2 due to the lack of pores and electrocatalytic active sites (TPB), as mentioned in the SEM section. On the other hand, Ni-doped PBCFNi10-GDC (0.068 Ω cm^2), PBCFNi20-GDC (0.033 Ω cm^2), and PBCFNi30-GDC (0.061 Ω cm^2) present better electrochemical performance than that of commercial LSM-YSZ cathode (0.15 Ω cm^2), because the extended catalytic active sites by mixed ionic electronic conductivity provide better oxygen kinetics.[41]

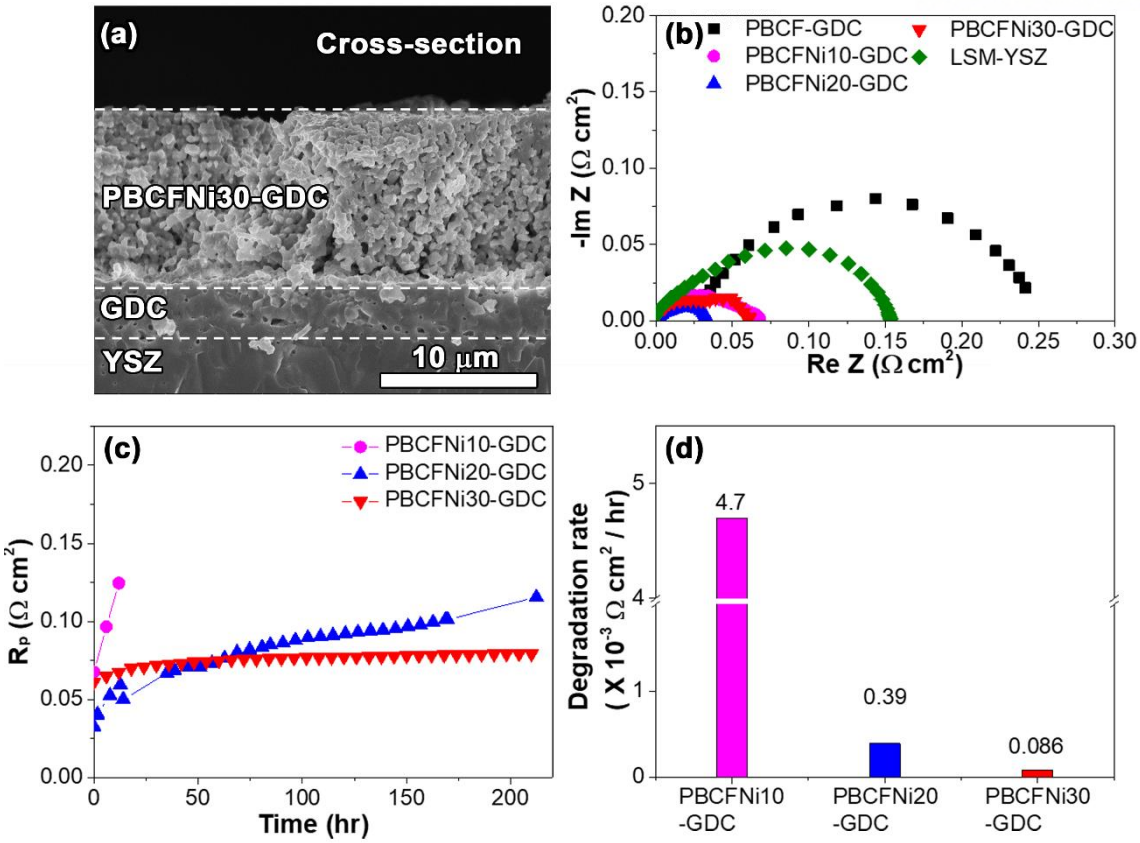

Fig. 4-5. (a) cross-sectional SEM image of PBCFNi30-GDC|GDC|YSZ, (b) impedance spectra of PBCFNi-GDC and LSM-YSZ, (c) long-term stability test, and (d) degradation rate of PBCFNi10-GDC, PBCFNi20-GDC, and PBCFNi30-GDC at 850 ºC

The polarization resistance of PBCFNi20 is much lower than that of PBCFNi10 as shown in Fig. 4-5 (b). The improved polarization resistance can be explained by increased oxygen vacancy by Ni doping. As shown in Table 4-2, the increasing number of relatively lower valence Ni increases the oxygen vacancy by decreasing the oxidation state of B-site. Since the oxygen vacancy provides oxygen ion adsorption/desorption and oxygen transport, increasing oxygen vacancy can improve the electrochemical properties of the cathode.[11,42] However, PBCFNi30 deteriorates electrocatalytic activity possibly owing to the existence of a brownmillerite phase which has relatively lower ionic conduction as compared with perovskite.[43]

Table 4-3 Summary of the EIS and stability results at 850 °C

Sample	Polarization resistance (Ω cm^2)	Degradation rate ($\times10^{-3}$ Ω cm^2/h)
PBCF-GDC	0.24	-
PBCFNi10-GDC	0.068	4.7
PBCFNi20-GDC	0.033	0.39
PBCFNi30-GDC	0.061	0.086
LSM-YSZ	0.15	-

Fig. 4-5 (c) shows the long-term stability test of PBCFNi10-GDC, PBCFNi20-GDC, and PBCFNi30-GDC. The stability test was carried out by EIS measurement using a symmetrical cell at 850 °C. Since the particle coarsening is retarded with increasing Ni concentration during operation, the highest Ni concentrated PBCFNi30-GDC cathode shows outstanding long-term stability (degradation rate: 0.086×10^{-3} Ω cm^2/h) as compared with PBCFNi10-GDC (degradation rate: 4.7×10^{-3} Ω cm^2/h)and PBCFNi20-GDC(degradation rate: 0.39×10^{-3} Ω cm^2/h).

4.4 Conclusion

Fe-based MIEC $Pr_{0.5}Ba_{0.3}Ca_{0.2}Fe_{1-x}Ni_xO_{3-\delta}$ (x = 0, 0.1, 0.2, and 0.3; PBCFNi) cathodes have been studied as an alternative of the most commonly used LSM cathode for high temperature commercial SOFC system (operating temperature: 800 °C ~ 1000 °C). Ni dopant not only retards electrochemical degradation of Fe-based perovskite by preventing coarsening of the particle during fabrication and operation, but also improves the polarization resistance by increasing the oxygen vacancy of PBCF. The composite PBCFNi30-GDC cathode exhibits lower cathodic polarization resistance of 0.061 Ω cm^2 as compared to LSM-YSZ (0.15 Ω cm^2) with the excellent long-term stability of 0.086×10^{-3} Ω m^2/hr at 850 °C. Therefore, PBCFNi30-GDC can be considered as a promising alternative to the LSM cathode for high-temperature commercial SOFC systems.

Reference

1. Chen, F., Liu, M., Preparation of yttria-stabilized zirconia (YSZ) films on $La_{0.85}Sr_{0.15}MnO_3$ (LSM) and LSM-YSZ substrates using an electrophoretic deposition (EPD) process, *Elsevier, J. Eup. Ceram. Soc*., Vol. 21, No. 2, pp127-134, 2001.
2. Lim, C., Sengodan, S., Jeong, D., Shin, J., Kim, G, Investigation of the Fe doping effect on the B-site of the layered perovskite $PrBa_{0.8}Ca_{0.2}Co_2O_{5+\delta}$ for a promising cathode material of the intermediate-temperature solid oxide fuel cells, *Elsevier, Int. J. Hydrogen Energy*., Vol. 44, No. 2, pp1088-1095, 2019.
3. Sengodan, S., Choi, S., Jun, A., Shin, T. H., Ju, Y. -W., Jeong, H. Y., Shin, J., Irvine, J. T. S., Kim, G., Layered oxygen-deficient double perovskite as an efficient and stable anode for direct hydrocarbon solid oxide fuel cells, *Nature, Nature Mat*., Vol. 14, pp 205-209, 2015.
4. Choi, S., Yoo, S., Kim, J., Park, S., Jun, A., Sengodan, S., Kim, J., Shin, J., Jeong, H. Y., Choi, Y., Kim, G., Liu, M., Highly efficient and robust cathode materials for low-temperature solid oxide fuel cells: $PrBa_{0.5}Sr_{0.5}Co_{2-x}Fe_xO_{5+\delta}$, *Nature, Sci. Rep*., Vol. 3, pp 2426, 2013.
5. Weber, A., Ivers-Tiffée, E., Materials and concepts for solid oxide fuel cells (SOFCs) in stationary and mobile applications. *Elsevier, J. power sources*., Vol. 127, No. 1-2, pp 273-283, 2004.
6. Minh, N. Q., Solid oxide fuel cell technology - Features and applications, *Elsevier, Solid State Ionics*, Vol. 174, No. 1-4, pp 271-277, 2004.
7. Huang, Y., Vohs, J. M., Gorte, R. J., SOFC Cathodes Prepared by Infiltration with Various LSM Precursors. *ECS, Electrochem. Solid-State Lett.*, Vol. 9, No. 5, pp A237-A240, 2006.
8. Piao, J., Sun, K., Zhang, N., Xu, S., A study of process parameters of LSM and LSM-YSZ composite cathode films prepared by screen-printing, *Elsevier, J. power sources*., Vol. 175, No. 1, pp 288-295, 2008.
9. Niu, Y., Sunarso, J., Zhou, W., Liang, F., Ge, L., Zhu, Z., Shao, Z., Evaluation and optimization of $Bi_{1-x}Sr_xFeO_{3-\delta}$ perovskites as cathodes of solid oxide fuel cells, *Elsevier, Int. J. Hydrogen Energy*, Vol. 36, No. 4, pp 3179-3186, 2011.

10. Kishimoto, H., Sakai, N., Horita, T., Yamaji, K., Brito, M. E., Yokokawa, H., Cation transport behavior in SOFC cathode materials of $La_{0.8}Sr_{0.2}CoO_3$ and $La_{0.8}Sr_{0.2}FeO_3$ with perovskite structure, *Elsevier, Solid State Ionics*, Vol. 178, No. 21-22, pp 1317-1325, 2007.
11. Huang, K., Lee, H. Y., Goodenough, J. B., Sr- and Ni-Doped $LaCoO_3$ and $LaFeO_3$ Perovskites, *ECS, J. Electrochem. Soc*., Vol. 145, No. 9, pp 3220-3227, 1998.
12. Burnwal, S. K., Suresh, M. B., Kistaiah, P. Synthesis and Characterization of Ni Doped BSCF as a Cathode Material for IT-SOFC. *IJSR, Int. J. Sci. Res.*, Vol. 2, No. 2, pp 377-379, 2013.
13. Wang, L., Dou, R., Li, Y., Lu, H., Bai, M., Hall, D., Chen, Y., Microstructure and mechanical properties of $Ba_{0.5}Sr_{0.5}Co_{0.8}Fe_{0.2}O_{3-\delta}$ perovskite-structured oxides doped with different contents of Ni, *Elsevier, Mater. Sci. Eng. A*, Vol. 658, pp 280-288, 2016.
14. Yaqub, A., Janjua, N. K., Savaniu, C., Irvine, J. T. S. Synthesis and characterization of B-site doped $La_{0.2}0Sr_{0.25}Ca_{0.45}TiO_3$ as SOFC anode materials, *Elsevier, Int. J. Hydrogen Energy*, Vol. 40, No. 1, pp 760-766, 2015.
15. Tzing, W. H., Tuan, W. H., Effect of NiO addition on the sintering and grain growth behavior of $BaTiO_3$, *Elsevier, Ceram. Int*., Vol. 25, No. 1, pp 6-75, 1999.
16. Yoo, S., Jun, A., Ju, Y. -W., Odkhuu, D., Hyodo, J., Jeong, H. Y., Park, N., Shin, J., Ishihara, T., Kim, G., Development of double-perovskite compounds as cathode materials for low-temperature solid oxide fuel cells. *Wiley, Angew. Chemie. Int. Ed.*, Vo.l. 53, No. 48, pp 13064-13067, 2014.
17. Lim. C., Jun, A., Jo, H., Ok, K. M., Shin, J., Ju, Y. -W., Kim, G., Influence of Ca-doping in layered perovskite $PrBaCo_2O_{5+\delta}$ on the phase transition and cathodic performance of a solid oxide fuel cell. *RSC, J. Mater. Chem. A.*, Vol. 4, No. 17, pp 6479-6486, 2016.
18. Choi, S., Park, S., Shin, J., Kim, G., The effect of calcium doping on the improvement of performance and durability in a layered perovskite cathode for intermediate-temperature solid oxide fuel cells, *RSC, J. Mater. Chem. A*, Vol. 3, No. 11, pp 6088-6095, 2015.
19. Hagiwara, A., Hobara, N., Takizawa, K., Sato, K., Abe, H., Naito, M., Preparation and evaluation of mechanochemically fabricated LSM/ScSZ composite materials for SOFC cathodes, *Elsevier, Solid State Ionics*, Vol. 177, No. 33-34, pp 2967-2977, 2006.

20. Hagiwara, A., Hobara, N., Takizawa, K., Sato, K., Abe, H., Naito, M.. Microstructure control of SOFC cathodes using the self-organizing behavior of LSM/ScSZ composite powder material prepared by spray pyrolysis, *Elsevier, Solid State Ionics*, Vol. 178, No. 27-28, pp 1552-1562, 2007.
21. Hosokawa, K., Kondo, A., Okumiya, M., Abe, H., Naito, M., One-step mechanical processing to prepare LSM/ScSZ composite particles for SOFC cathode. *Elsevier, Adv. Powder Technol.*, Vol. 25, No. 5, pp 1430-1434, 2014.
22. Yang, S. H., Kim, K. H., Yoon, H. H., Kim, W. J., Choi, H. W., Comparison of combustion and solid-state reaction methods for the fabrication of SOFC LSM cathodes. *Taylor&Francis, Mol. Cryst. Liq. Cryst.*, Vol. 539, No. 1, pp 50/[390]-57/[397], 2011.
23. Imanishi, N., Ohno, R., Murata, K., Hirano, A., Takeda, Y., Yamamoto, O., Yamahara, K., LSM-YSZ cathode with infiltrated cobalt oxide and cerium oxide nanoparticles, *Wiley, Fuel Cells* Vol. 9, No. 3, pp 215-221, 2009.
24. Zhu, J. Guo, S., Chu, Z., Jin, W., CO_2-tolerant oxygen-permeable perovskite-type membranes with high permeability, *RSC, J. Mater. Chem. A.*, Vol. 3, No. 45, pp 22564-22573, 2015.
25. Shannon, R. D., Prewitt, C. T., Effective ionic radii in oxides and fluorides, *Wiley, Acta Cryst.*, Vol. 25, No. 5, pp 925-946, 1969.
26. Cullity, B. D., *Elements of X-ray diffraction. 2nd ed.*, Addison-Wesley Publ. Co., Osmania University, Miami, 1978.
27. Ortiz-Vitoriano, N., De Larramendi, I. R., Cook, S. N., Burriel, M., Aguadero, A., Kilner, J. A., Rojo, T., The formation of performance enhancing pseudo-composites in the highly active $La_{1-x}Ca_xFe_{0.8}Ni_{0.2}O_3$ system for IT-SOFC application, *Wiley, Adv. Funct. Mater.*, Vol. 23, No. 41, pp 5131-5139, 2013.
28. Lee, S. J., Yong, S. -M., Kim, D. S., Kim, D. K., Cobalt-free composite cathode for SOFCs: Brownmillerite-type calcium ferrite and gadolinium-doped ceria, *Elsevier, Int. J. Hydrogen Energy*, Vol. 37, No. 22, pp 17217-17224, 2012.
29. Jun, A., Shin, J., Kim, G., High redox and performance stability of layered $SmBa_{0.5}Sr_{0.5}Co_{1.5}Cu_{0.5}O_{5+\delta}$ perovskite cathodes for intermediate-temperature solid oxide fuel cells, *RSC, Phys. Chem. Chem. Phys.*, Vol. 15, No. 45, pp 19906-19912, 2013.

30. Duan, Z., Yang, M., Yan, A., Hou, Z., Dong, Y., Chong, Y., Cheng, M., Yang, W., $Ba_{0.5}Sr_{0.5}Co_{0.8}Fe_{0.2}O_{3-\delta}$ as a cathode for IT-SOFCs with a GDC interlayer, *Elsevier, J. Power Sources*, Vol. 160, No. 1, pp 57-64, 2006.

31. Cortés-Escobedo, C. A., Muñoz-Saldaña, J., Bolarín-Miró, A. M., Sánchez-de Jesús, F., Determination of strontium and lanthanum zirconates in YPSZ-LSM mixtures for SOFC, *Elsevier, J. Power Sources*, Vol. 180, No. 1, 2008.

32. Kida, T., Takauchi, D., Watanabe, K., Yuasa, M., Shimanoe, K., Teraoka, Y., Yamazoe, N., Oxygen Permeation Properties of Partially A-Site Substituted $BaFeO_{3-\delta}$ Perovskites, *ECS, J. Electrochem. Soc.*, Vol. 156, No. 12, pp E187-E191, 2009.

33. Kim, D. Y., Miyoshi, S., Tsuchiya, T., Yamaguchi, S., Defect Chemistry and Electrochemical Properties of $BaZrO_3$ Heavily Doped with Fe, *ECS, ECS Trans.*, Vol. 45, No. 1, pp 161-170, 2012.

34. Dong, F., Chen, D., Chen, Y., Zhao, Q., Shao, Z., La-doped $BaFeO_{3-\delta}$ perovskite as a cobalt-free oxygen reduction electrode for solid oxide fuel cells with oxygen-ion conducting electrolyte, *RSC, J. Mater. Chem.*, Vol 22, No. 30, pp 15071-15079, 2012.

35. Fu, C., Sun, K., Zhang, N., Chen, X., Zhou, D., Electrochemical characteristics of LSCF-SDC composite cathode for intermediate temperature SOFC, *Elsevier, Electrochimica Acta*, Vol. 52, No. 13, pp 4589-4594, 2007.

36. Park, S., Choi, S., Shin, J., Kim, G., A collaborative study of sintering and composite effects for a $PrBa_{0.5}Sr_{0.5}Co_{1.5}Fe_{0.5}O_{5+\delta}$ IT-SOFC cathode, *RSC, RSC Adv*. Vol. 4, No. 4, pp 1775-1781, 2014.

37. Kim, S., Jun, A., Kwon, O., Kim, J., Yoo, S., Jeong, H. Y., Shin, J., Kim, G., Nanostructured Double Perovskite Cathode With Low Sintering Temperature For Intermediate Temperature Solid Oxide Fuel Cells. *Wiley, ChemSusChem*, Vol. 8, No. 18, 2015.

38. Torres-Garibay, C., Kovar, D., Manthiram, A., $Ln_{0.6}Sr_{0.4}Co_{1-y}Fe_yO_{3-\delta}$ (Ln = La and Nd; y = 0 and 0.5) cathodes with thin yttria-stabilized zirconia electrolytes for intermediate temperature solid oxide fuel cells, *Elsevier, J. Power Sources*, Vol. 187, No. 2, pp 480-486, 2009.

39. Holzwarth, U., Gibson, N., The Scherrer equation versus the 'Debye-Scherrer equation', *Nature*, *Nat. Nanotechnol.*, Vol. 6, 2011.

40. Yoo, S., Shin, J., Kim, G., Thermodynamic and Electrical Properties of Layered Perovskite $NdBaCo_{2-x}Fe_xO_{5+\delta}$-YSZ ($x$ = 0, 1) Composites for Intermediate Temperature SOFC Cathodes, *ECS*, *J. Electrochem. Soc.*, Vol. 158, No. 6, pp B632-B638, 2011.

41. Choi, S., Park, S., Kim, J., Lim, T. -H., Shin, J., Kim, G., Electrochemical properties of an ordered perovskite $LaBaCo_2O_{5+\delta}$-$Ce_{0.9}Gd_{0.1}O_{2-\delta}$ composite cathode with strontium doping for intermediate-temperature solid oxide fuel cells, Elsevier, Electrochem. Commun. Vol. 34, pp 5-8, 2013.

42. Yoo, S., Choi, S., Shin, J., Liu, M., Kim, G., Electrical properties, thermodynamic behavior, and defect analysis of $La_{n+1}Ni_nO3_{n+1+\delta}$ infiltrated into YSZ scaffolds as cathodes for intermediate-temperature SOFCs, *RSC*, *RSC Adv.*, Vol. 2, No. 11, pp 4648-4655, 2012.

43. Fagg, D. P., Kharton, V. V., Kovalevsky, A. V., Viskup A. P., Naumovich, E. N., Frade, J. R., The stability and mixed conductivity in La and Fe doped $SrTiO_3$ in the search for potential SOFC anode materials, *ECERS*, *J. Eur. Ceram. Soc.*, Vol. 21, No. 10-11, pp 1831-1835, 2001.

Chapter 5. Energy storage: Nano-perovskite oxide prepared *via* inverse microemulsion mediated synthesis for oxygen evolution reaction catalyst

DOI: https://doi.org/10.1016/j.electacta.2018.04.121

5.1. Introduction

Li-air batteries are receiving significant attention due to their higher theoretical energy density (11,140 Wh kg^{-1}) compared to other rechargeable batteries such as Li-ion polymer (387 Wh kg^{-1}) and Li-S (1,086 Wh kg^{-1}) batteries. [1-4] However, the practical use of Li-air batteries is hampered by poor performance and low energy efficiency during cycling, mainly because of the high overpotential at the air electrode. [5,6] For this reason, Li-air batteries need new air-electrode catalysts with high catalytic activity and stability. At present, precious metal catalysts such as Pt/C and IrO_2 are considered as the most effective air electrode catalyst for Li-air batteries because of their excellent catalytic activity in oxygen reduction reaction (ORR) and oxygen evolution reaction (OER). [7,8] However, the development of alternative catalysts is required due to the high cost and instability of those catalysts. Some candidate materials have been viewed as alternatives for air electrode of Li-air batteries., e.g., carbon-based materials, [9] spinel structured oxides, [10] and perovskite structured oxides. [11-15] Among these alternatives, the perovskite structured oxides are attracting attention owing to their high electrical conductivity, electro-catalytic activity, and redox stability. [16-20] On the other hand, despite these excellent properties, the high synthesis temperature (1000 ~ 1500 °C) of the perovskite structured oxides decreases the specific surface area, thereby degrading the electrochemical performance. The main challenge to the perovskite structured oxides is, therefore, to increase the surface area for sufficient electrochemically active sites. In this regard, many researchers have studied various methods such as microemulsion, [21] hydrothermal, [22] co-precipitation, [23] and electro-spinning [24] to increase the surface area. Among them, the microemulsion is one of the simplest and most effective ways of constructing nanostructures because it can prevent particle agglomeration through the encapsulation of a precursor. [21] The microemulsion can also reduce the synthesis temperature by atomic-scale mixing and chemical

homogeneity. [25-27] The nano-size particles are expected to improve electrochemical performance and catalytic activity by the nano-size effect and the extended surface area. [13,25,28]

In this paper, we successfully synthesized a nano-size perovskite structured oxide, $Nd_{0.67}Sr_{0.33}CoO_{3-\delta}$ (NSC), as an air electrode catalyst of a Li-air battery through a simple inverse microemulsion (water-in-oil) route. The synthesized nano-size NSC particles achieved excellent catalytic activity for both ORR and OER. In this regard, nano-size NSC particles prepared *via* microemulsion process can be regarded as a promising catalyst for a Li-air battery application because of their excellent catalytic activity, electrochemical performance, and durability.

5.2. Experimental

5.2.1. Synthesis of powder

Nano-size NSC particles were prepared by a multi-step inverse microemulsion method (ME-NSC) using anodic surfactant cetyltrimethylammonium bromide (CTAB; 98 %, Alfa Aesar Co.). [13] As described in Fig. 5-1 (a), 30 mL of 2,2,4-trimethylpentane (99+ %, ACROS Co.) (oil phase) and 6 mL of 1-butanol (99 %, Alfa Aesar Co.) (co-surfactant) were mixed in a conical beaker by stirring for 30 minutes. 6 g of CTAB and a stoichiometrically calculated amount of 0.5 M $Nd(NO_3)_3 \cdot 6H_2O$ (99.9 %, Sigma-Aldrich Co.), 0.5 M $Sr(NO_3)_2$ (99+ %, Sigma-Aldrich Co.), and 0.5 M $Co(NO_3)_2 \cdot 6H_2O$ (98+ %, Sigma-Aldrich Co.) solutions were added to the mixture to form emulsion A.

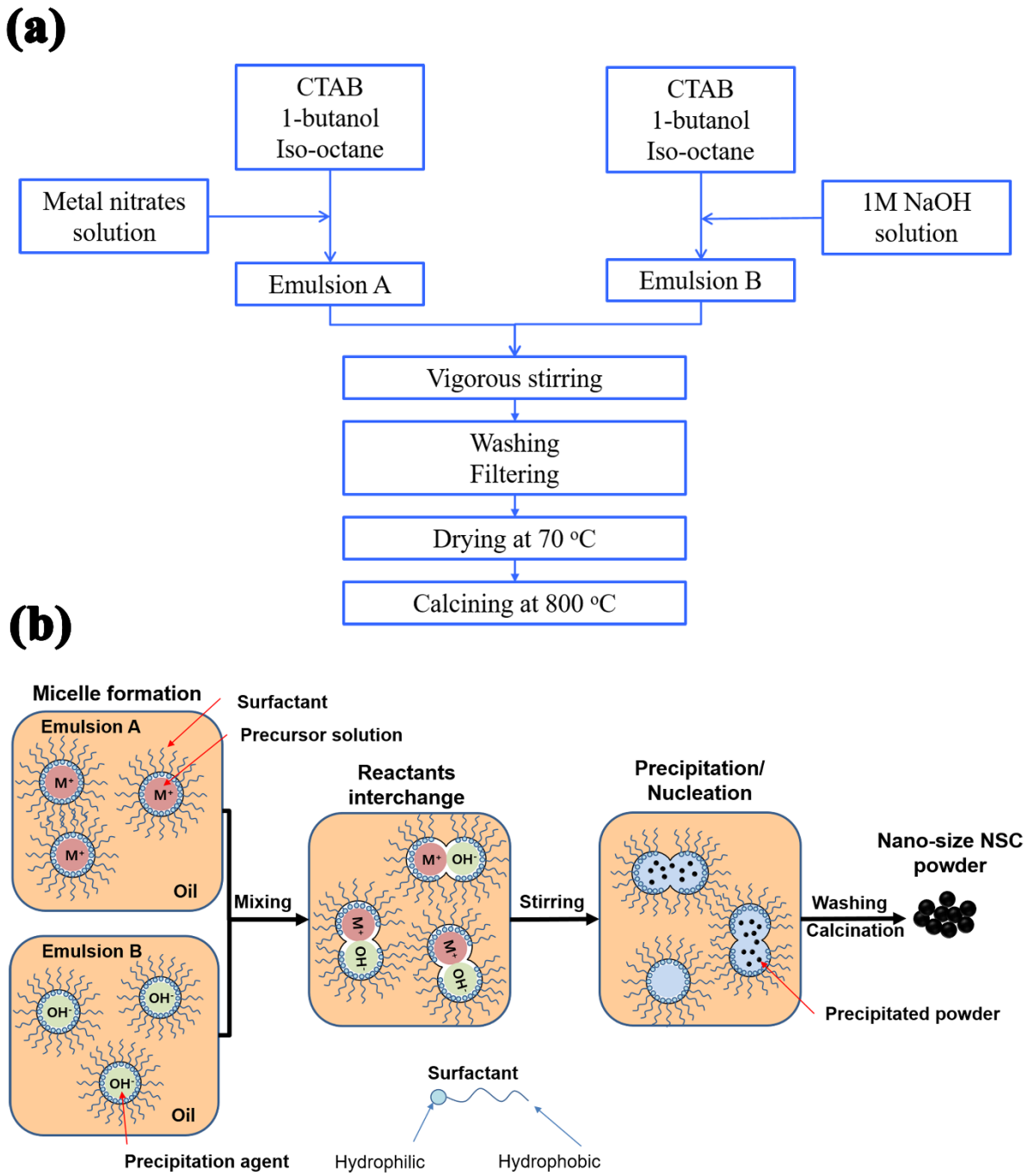

Fig. 5-1 (a) Schematic diagram of the synthesis method of ME-NSC and (b) schematic image of the inverse micro-emulsion (water-in-oil)

1 M NaOH solution (98+ %, Samchun Pure Chemical Co.) was added to another mixture composed of oil, a surfactant, and a co-surfactant to make emulsion B. The mixture of emulsions A and B was

vigorously stirred overnight to precipitate and nucleate the precursor. Sequentially, the precipitated precursor was collected by filtration and washed with ethanol, acetone, and deionized (DI) water to remove the residues of oil, surfactant, and precipitation agent. The collected powder was dried in an oven at 70 ºC for 2 h and calcined at 800 ºC for 4 h. Conventional NSC particles were also prepared by the Pechini method (P-NSC). [17] Calculated amounts of $Nd(NO_3)_3 \cdot 6H_2O$, $Sr(NO_3)_2$, and $Co(NO_3)_2 \cdot 6H_2O$ were dissolved in DI water to form an aqueous solution with the appropriate amounts of citric acid and ethylene glycol. The mixture was heated at 250 ºC until a viscous resin formed and was combusted thereafter. The combusted ash was calcined at 600 ºC for 4 h and ball-milled in acetone for 24 h after calcination. The ball-milled powder was heated at 950 ºC for 4 h and super-milled for 1 h.

5.2.2. Characterization of powder

The microstructure of the synthesized powder was observed by field emission scanning electron microscopy (FE-SEM; Nova NanoSEM, FEI Co.). The crystal structure of the synthesized powder was analyzed by high-resolution transmission electron microscopy (HR-TEM; JEM-2100F, JEOL Co.) and X-ray diffractometer (XRD; D/MAX2500V/PC, Rigaku Co.). N_2 adsorption and desorption isotherms measurement was carried out at -196 ºC (BELSORP-MiniII, BEL Co.) to evaluate the pore structure and specific surface area. Before measurement, the samples were degassed at 150 ºC for 12 h under N_2 flow. The specific surface area of the catalysts was calculated from the N_2 adsorption and desorption isotherms results by the Brunauer-Emmett-Teller (BET) method. The oxidation state of cobalt on the NSC surface was determined by an X-ray photoelectron spectroscopy (XPS) analysis (ESCALAB 250XI, ThermoFisher Co.) with a monochromated Al-Kα (ultraviolet He1, He2) X-ray source under an ultra-high vacuum (1 x 10^{-10} Torr).

5.2.3. Electrochemical performance by half-cell test

An electrochemical test was performed using a computer-controlled potentiostat (VMP3, Biologic Co.)

with a rotating ring disk electrode (RRDE) system (RRDE-3A, ALS Co.). The counter electrode was a platinum wire, and the reference electrode was a Hg/HgO (1 M NaOH filled) electrode. The working electrode was prepared by drop-coating a catalyst ink onto the pre-polished glassy carbon (GC) disk electrode. A catalyst ink was prepared by a previously reported method; a catalyst powder and the carbon (KB; Ketjen Black EC-600JD, AkzoNobel N. V.) were mixed with a weight ratio of 8 : 2 and then dispersed by bath ultrasonication in an ethanol/isopropyl mixture and Nafion stock solution for 10 minutes. [24] A small amount of additive, Nafion stock solution (5 wt%), could effectively improve the dispersity of the catalysts and enhance the adhesion to the GC electrode. A total of 10 μL of well-dispersed catalyst ink was applied onto the pre-polished GC disk electrode (5 mm in diameter). The prepared electrode was dried at room temperature before the electrochemical tests.

5.2.4. Preparation of a hybrid Li-air battery

A hybrid Li-air battery cell was prepared to evaluate the electrochemical property of the catalyst. [24] A lithium foil with a thickness of 0.2 mm was obtained from Honjo Metal. 1 M lithium hexafluorophosphate solution ($LiPF_6$; Sigma-Aldrich Co.) in tetraethylene glycol dimethyl ether (TEGDME; 99+ %, Sigma-Aldrich Co.) and 0.1 M lithium hydroxide (LiOH; 98+ %, Sigma-Aldrich Co.) in DI water were used as an organic liquid electrolyte and an aqueous liquid electrolyte, respectively. The organic liquid electrolyte and the aqueous liquid electrolyte were separated by a 0.15 mm thick $Li_{1+x+y}Ti_{2-x}Al_xP_{3-y}Si_yO_{12}$ (OHARA Inc.) solid Li-ion conducting ceramic glass. An air electrode was prepared by spraying a catalyst ink with 20 wt.% KB and PVdF-HFT binder (Sigma-Aldrich Co.) onto a gas-diffusion layer (TGP-H-090, Toray Co.). The loading density of the catalysts and the binder content in the air electrode were 1 mg cm^{-2} and 20 wt.%, respectively. Thus, the current density could be easily normalized with the loading density of the catalyst (0.8 mg cm^{-2}).

5.3. Results and Discussion

5.3.1. Characterization of samples

Fig. 5-2 (a) shows the XRD patterns of the ME-NSC and P-NSC, indicating that both samples have orthorhombic perovskite phase (space group: *pbnm*) without any detectable impurities or secondary phases.

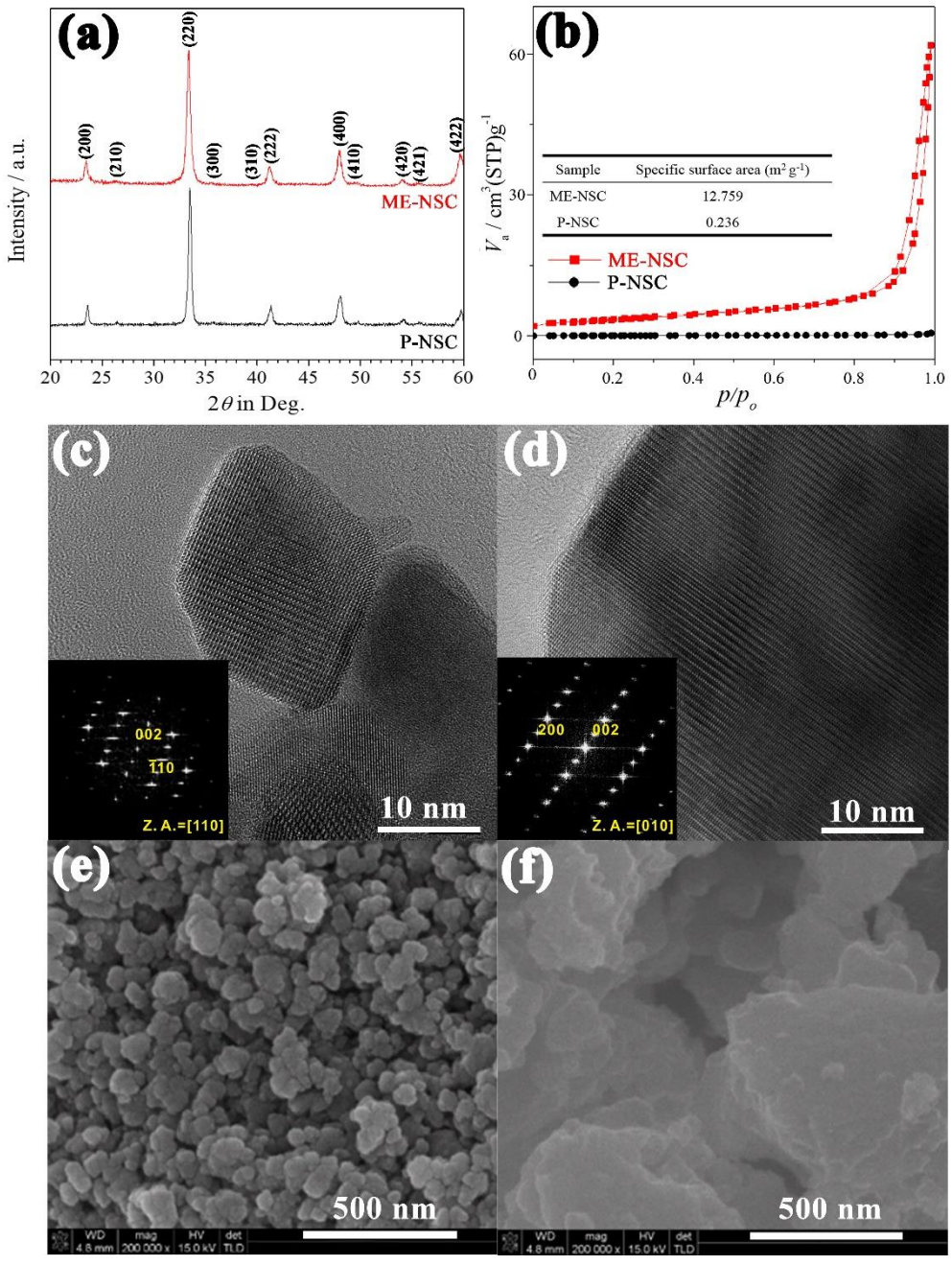

Fig. 5-2. (a) XRD patterns of ME-NSC and P-NSC, (b) N_2 adsorption and desorption isotherms curves of ME-NSC and P-NSC, HR-TEM images of (c) ME-NSC and (d) P-NSC (inset: SAED patterns), and FE-SEM images of (e) ME-NSC and (f) P-NSC

More detailed crystallographic information of ME-NSC and P-NSC can be obtained from TEM analysis, as shown in Fig. 5-2 (c) and (d). The *d*-space values in the (002) plane of ME-NSC and P-NSC from the selected area electron diffraction (SAED) patterns (inset of Fig. 5-2 (c) and (d)) are 0.3794 nm and 0.3774, respectively, which are well-matched with XRD results. As seen in the FE-SEM image (Fig. 5-2 (e) and (f)), ME-NSC shows uniform nano-size particles (average size: 16 ± 1.7 nm) while P-NSC shows large irregular particles (average particle size: 162 ± 30.1 nm). The nano-size ME-NSC particles are fabricated by the microemulsion consisting of three main components: an oil phase, an aqueous solution containing cations, and a surfactant. As described in Fig. 5-1 (b), the hydrophilic part of the amphipathic surfactant surrounds the aqueous solution containing cations, and the hydrophobic part combines with the oil phase to form spherical micelles. [29,30] Since these micelles act as nano-size reactors and the precipitation reaction occurs only in the micelles, the growth of primary particles is limited. Micelles charged negatively with an anodic surfactant, CTAB, increase the distance between the particles due to the repulsive force between the micelles, further inhibiting grain growth of particles. [21]

The specific surface area of ME-NSC and P-NSC can be quantified by N_2 adsorption and desorption isotherms with the Brunauer-Emmett-Teller (BET) method. While P-NSC shows type II hysteresis loops, ME-NSC exhibits type IV hysteresis loops with *meso*porous adsorbents, as shown in the N_2 adsorption and desorption isotherms curves (Fig. 5-2 (b)). In Type IV hysteresis loops, the difference in the adsorption and desorption isotherms at high partial pressure is due to the capillary condensation of the *meso*pores. [31] ME-NSC shows a much higher specific surface area (12.759 $m^2 g^{-1}$) than P-NSC (0.236 $m^2 g^{-1}$), confirming its small particle size and existence of *meso*pore. [32] We can expect favorable results because it is well known that the electrochemical performance improves with the increased surface area, i.e. catalytically active sites.

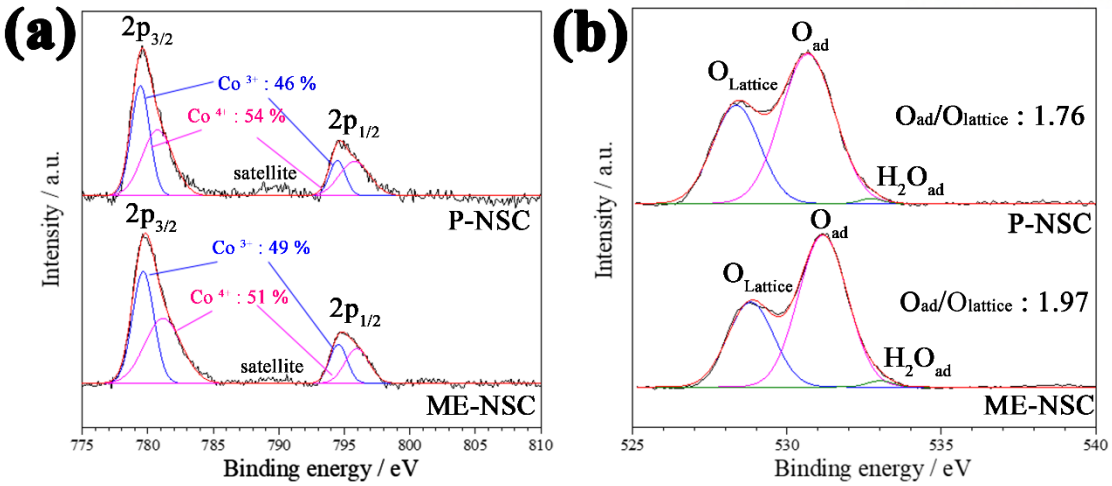

Fig. 5-3. XPS spectra of (a) Co_{2p} orbital and (b) O_{1s} orbital of ME-NSC and P-NSC

The oxidation state of cobalt on the surface of the NSC can affect catalytic activities for ORR and OER (Fig. 5-3 (a)). In the Co_{2p} spectra of ME-NSC and P-NSC, the main peaks are located at 779.7 eV and 794.7 eV, indicating a low-energy band ($Co_{2p3/2}$) and a high-energy band ($Co_{2p1/2}$), respectively. [33,34] A weak satellite shoulder peak located at around 790 eV also indicates the presence of low spin Co^{3+} on the surface of the catalyst. [11] The low-energy band peak can be deconvoluted into two peaks at 779.6 eV and 780.3 eV; the peak at 779.6 eV can be assigned to Co^{3+} and the peak at 780.3 eV can be ascribed to Co^{4+}. [33] Considering the intensity of the peaks, ME-NSC shows a higher amount of Co^{3+} (49 %) as compared with P-NSC (46 %). It is known that oxide powders synthesized by an inorganic-organic method with a low synthesis temperature increase the amounts of Co^{3+} and adsorbed oxygen species compared to the conventional sol-gel method. Since Co^{3+} acts as a donor-acceptor reduction site, it is closely related to the catalytically active site and the enhanced catalytic performance is expected with a larger amount of Co^{3+}. [34]

Fig. 5-3 (b) shows the XPS spectra of O_{1s} core levels obtained from ME-NSC and P-NSC. As reported in previous studies, oxygen on the oxide surface can exist in three forms: lattice oxygen, adsorbed oxygen species, and adsorbed OH^- molecules. [35] The deconvoluted O1s spectrum can be separated into three peaks: 528 ~ 529 eV, 530 ~531 eV, and 533 eV, representing lattice oxygen ($O_{lattice}$), adsorbed oxygen species (O_{ad}: O^- and O^{2-}), and adsorbed hydroxide (OH^-), respectively. [33] ME-NSC has more

adsorbed oxygen species ($O_{ad}/O_{lattice}$ = 1.97) than P-NSC (1.76). The adsorbed oxygen species are weakly bonded to the crystal lattice and easily released from the lattice, acting catalytic active site. In these regards, the catalytic activity for both the ORR and OER can be improved with increasing amounts of Co^{3+} and adsorbed oxygen species.

5.3.2. Electrochemical analysis

5.3.2.1. Half-cell test by RRDE

The catalytic activities of the catalysts were evaluated using a rotating ring-disk electrode (RRDE) in O_2 saturated 0.1 M KOH electrolyte.

Table 5-1 Summary of the RRDE results of ME-NSC, P-NSC, Pt/C, IrO_2 in this study and BSCF

Sample	Oxygen reduction reaction (ORR)		Oxygen evolution reaction (OER)	
	On-set potential *vs*. (Hg/HgO) / V	Current at -0.7 V *vs*. (Hg/HgO) / mA cm^{-2}	On-set potential *vs*. (Hg/HgO) / V	Current at 0.9 V *vs*. (Hg/HgO) / mA cm^{-2}
ME-NSC	-0.096	-5.52	0.542	33.68
P-NSC	-0.123	-5.16	0.598	18.83
Pt/C	0.045	-6.06	-	-
IrO_2	-	-	0.589	9.99
BSCF [36]	-0.180	-4.43	0.575	12.31

Table 5-1 summarizes the RRDE results including the current density and on-set potential of the catalysts. Fig. 5-4 (a) shows the linear sweep voltage (LSV) curves of ME-NSC, P-NSC, IrO_2, and BSCF [36] with a potential range of 0.38 V ~ 0.9 V *vs*. (Hg/HgO). The current density of ME-NSC (33.68 mA cm^{-2} at 0.9 V *vs*. (Hg/HgO)) is much higher than that of P-NSC (18.83 mA cm^{-2}), IrO_2 (9.99 mA cm^{-2}), and BSCF (12.31 mA cm^{-2}). The lower on-set potential generally means the fast electro-catalytic activity of the catalyst.

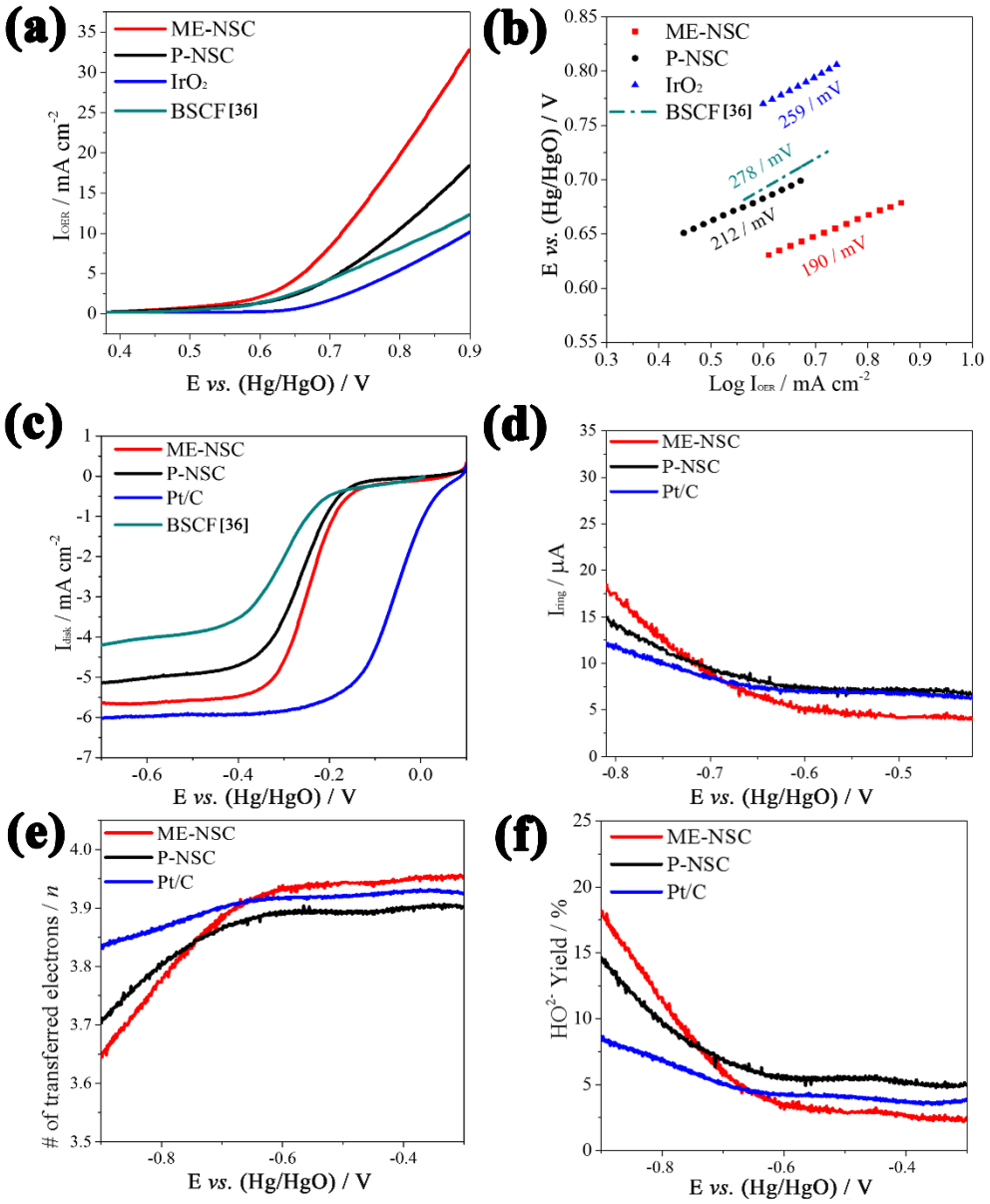

Fig. 5-4. (a) Linear sweeping voltammetry curves of ME-NSC, P-NSC, IrO_2, and BSCF [36], (b) Tafel plots of ME-NSC, P-NSC, IrO_2, and BSCF [36] in OER region, (c) ORR disk current of ME-NSC, P-NSC, Pt/C, and BSCF [36], (d) ring current, (e) number of transferred electrons, and (f) peroxide yield of ME-NSC, P-NSC, and Pt/C

On-set potential of ME-NSC (0.542 V *vs*. (Hg/HgO)) is significantly lower than that that of P-NSC (0.598 V *vs*. Hg/HgO), IrO_2 (0.589 V *vs*. (Hg/HgO)), and BSCF (0.575 V *vs*. (Hg/HgO)). The kinetics

of the catalysts were analyzed by Tafel plots, in which the low slope indicates fast kinetics of the catalyst. [37] Fitted Tafel slopes of ME-NSC, P-NSC, IrO_2, BSCF [36] for OER were 190 / mV, 212 / mV, 259 / mV, and 278 / mV, respectively (Fig. 5-4 (b)), suggesting outstanding OER kinetics of ME-NSC. These superior electrocatalytic activities for the OER seem to originate from the existence of Co^{3+} in the perovskite. The intermediate-spin state of Co^{3+} on the NSC catalyst surface can promote catalytic activity by forming a Co^{3+}/Co^{4+} redox couple on top of the O_{2p} bands. [12,24] The OER activity of ME-NSC appears to be significantly enhanced by the increased Co^{3+} and surface area through the microemulsion method. The extended surface area by microemulsion allows ME-NSC to have excellent ORR activity, as shown in the LSV curve of ME-NSC, P-NSC, Pt/C, and BSCF [36] with a potential range of -0.7 V ~ 0.1 V *vs*. (Hg/HgO) (Fig.5-4 (c)). The limiting current density at -0.7 V *vs*. (Hg/HgO) of ME-NSC (-5.52 mA cm^{-2}) is extraordinarily better than that of P-NSC (-5.16 mA cm^{-2}) and BSCF (-4.43 mA cm^{-2}). Moreover, on-set potential of ME-NSC (-0.096 V *vs*. (Hg/HgO)) is slightly better than P-NSC (-0.123 V *vs*. (Hg/HgO)) and significantly better than BSCF (-0.180 V *vs*. (Hg/HgO)). These superior ORR activities can be ascribed to the large surface area and the existence of Co^{3+}. It is well known that intermediate-spin Co^{3+} on the surface of cobaltite perovskite localizes e_g electrons which increase the rate of O_2^{2-}/OH^- displacement and OH^- regeneration, the rate-limiting step for the ORR in an alkaline solution. [14] In addition, the increase in adsorbed oxygen species by the microemulsion enhances the catalytic activity for ORR, as described in the XPS section.

The number of transferred electrons (n) is an important factor to evaluate the catalytic activity of the ORR. The ORR reaction *via* an alkaline medium occurs through two different pathways, 2 electrons transfer and 4 electrons transfer pathways. [38] The 4 electrons transfer pathway is preferred because they can prevent peroxide generation which adversely affects the stability of the catalyst. The number of transferred electrons and the peroxide yield during the ORR process are calculated from disk (Fig. 5-4 (c)) and ring (Fig. 5-4 (d)) currents according to Eq. 5-1 and 5-2, respectively. [13,24]

$$n = 4 \times \frac{I_{disk}}{I_{disk} + (\frac{I_{ring}}{N})} \qquad \text{Eq. 5-1}$$

$$\%HO_2^- = 200 \times \frac{(I_{ring}/N)}{I_{disk}+(\frac{I_{ring}}{N})} \qquad \text{Eq. 5-2}$$

The current collection efficiency of the Pt ring was determined from the reduction of $K_3Fe[CN]_6$ (N = 0.41). As shown in Fig. 5-4 (e), the numbers of transferred electrons of ME-NSC, P-NSC, Pt/C at -0.6 V *vs*. (Hg/HgO) are 3.93, 3.89, and 3.91, respectively, indicating that ME-NSC is more favorable to 4-electrons transfer than P-NSC. The corresponding peroxide yields (%) of ME-NSC and P-NSC are less than 10 % at -0.6 V *vs*. (Hg/HgO), as presented in Fig. 5-4 (f). In this regard, ME-NSC is viewed as a promising catalyst for air electrodes in Li-air batteries due to the excellent catalytic activity for the OER and the improved activity for the ORR.

5.3.2.2. Full-cell test *via* hybrid Li-air battery cell

The electrochemical behaviors of ME-NSC and Pt/C were evaluated using a hybrid Li-air battery as described in the previous report under ambient conditions. [24] As shown in Fig. 5-5 (a), the charge potential of ME-NSC (3.9 V *vs*. (Li/Li^+)) at 0.5 mA cm^{-2} is extremely smaller than that of Pt/C (4.2 V *vs*. (Li/Li^+)), indicating superior charging ability of ME-NSC catalyst from excellent OER properties.

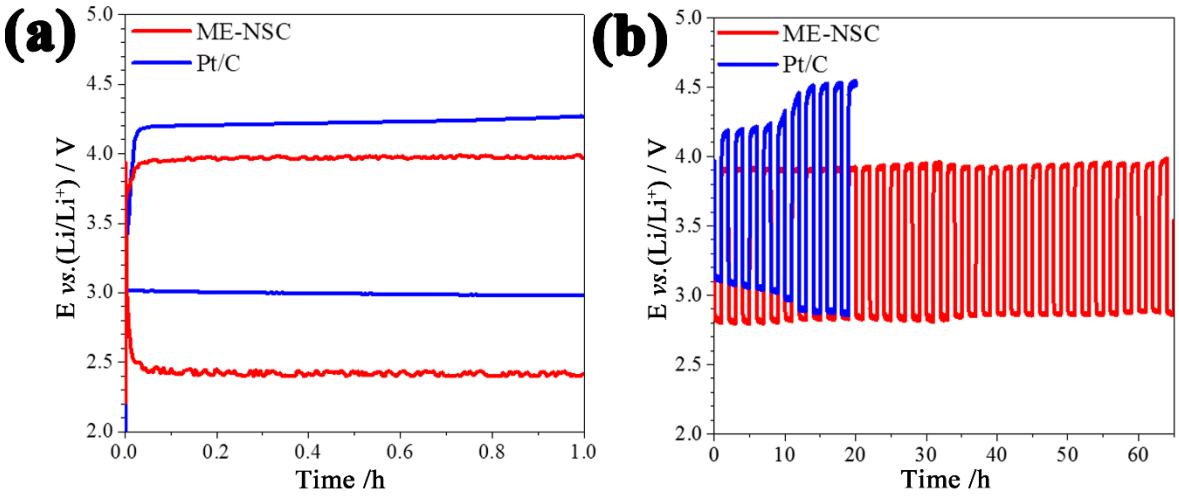

Fig. 5-5. (a) The first cycle of a hybrid Li-air battery cell at alternating current densities of 0.5 mA cm^{-2} and -0.5 mA cm^{-2} and (b) cycling performance of ME-NSC and Pt/C at alternating current densities of 0.1 mA cm^{-2} and -0.1 mA cm^{-2}

Fig.5-5 (b) presents cyclic discharge-charge curves for ME-NSC and Pt/C in 0.1 M LiOH at alternating current densities of 0.1 mA cm^{-2} and -0.1 mA cm^{-2}. A hybrid Li-air battery using the ME-NSC catalyst maintains a 1.1 V potential difference ($\Delta\eta$) between charge and discharge for more than 60 hours, but the potential difference increases significantly with Pt/C from 0.9 V to 1.6 V in 15 hours. These robust cyclability and stability make the nanostructured ME-NSC to be regarded as a promising air electrode catalyst of the hybrid Li-air batteries.

5.4. Conclusions

Nano-size NSC particles (ME-NSC) were successfully synthesized *via* a multi-step inverse microemulsion method by suppressing grain growth and retaining relatively low synthesis temperature. ME-NSC exhibits excellent OER performance (33.68 mA cm^{-2}) due to the high surface area and the existence of Co^{3+}. A hybrid Li-air battery using ME-NSC as a catalyst shows excellent cycle performance and stability over 60 hours with a potential difference of less than 1.1 V. Based on its superior electrochemical performance and stability, ME-NSC can be considered a promising electro-catalyst for Li-air batteries.

References

[1] G. Girishkumar, B. McCloskey, A. C. Luntz, S. Swanson, W. Wilcke, Lithium-air battery: Promise and challenges, J. Phys. Chem. Lett. 1 (2010) 2193-2203.

[2] K. M. Abraham, Z. Jiang, A polymer electrolyte-based rechargeable lithium/oxygen battery, J. Electrochem. Soc. 143 (1996) 1-5.

[3] B. Kumar, J. Kumar, R. Leese, J. P. Fellner, S. J. Rodrigues, K. M. Abraham, A solid-state, rechargeable, long cycle life lithium-air battery, J. Electrochem. Soc. 157 (2010) A50-A54.

[4] J. -S. Lee, S. T. Kim, R. Cao, N. -S. Choi, M. Liu, K. T. Lee, J. Cho, Metal-air batteries with high energy density: Li-air versus Zn-air, Adv. Energy. Mater. 1 (2011) 34-50.

[5] D. Zhang, Z. Fu, Z. Wei, T. Huang, A. Yu, Polarization of oxygen electrode in rechargeable lithium

oxygen batteries, J. Electrochem. Soc. 157 (2010) A362-A365.

[6] J. Christensen, P. Albertus, R. S. Sanchez-Carrera, T. Lohmann, B. Kozinsky, R. Liedtke, J. Ahmed, A. Kojic, A critical review of Li/air batteries, J. Electrochem. Soc. 159 (2012) R1-R30.

[7] H. Wang, R. Wang, H. Li, Q. Wang, J. Kang, Z. Lei, Facile synthesis of carbon-supported pseudo-core@shell PdCu@Pt nanoparticles for direct methanol fuel cells, Int. J. Hydrogen Energy 36 (2011) 839-848.

[8] Y. -C. Lu, Z. Xu, H. A. Gasteiger, S. Chen, K. Hamad-Schifferli, Y. Shao-Horn, Platinum-gold nanoparticles: A highly active bifunctional electrocatalyst for rechargeable lithium-air batteries, J. Am. Chem. Soc. 132 (2010) 12170-12171.

[9] Y. -W. Ju, S. Yoo, C. Kim, S. Kim, I. Y. Jeon, J. Shin, J. B. Baek, G. Kim. Fe@N-graphene nanoplatelet-embedded carbon nanofibers as efficient electrocatalysts for oxygen reduction reaction, Adv. Sci. 3 (2016) 1500205.

[10] Y. Liang, Y. Li, H. Wang, J. Zhou, J. Wang, T. Regier, H. Dai, Co_3O_4 nanocrystals on graphene as a synergistic catalyst for oxygen reduction reaction, Nat. Mater. 10 (2011) 780-786.

[11] O. Gwon, C. Kim, O. Kwon, H. Y. Jeong, H. -K. Park, J. Shin, Y. -W. Ju, G. Kim, An efficient oxygen evolution catalyst for hybrid lithium-air batteries: Almond stick type composite of perovskite and cobalt oxide, J. Electrochem. Soc. 163 (2016) A1893-A1897.

[12] J. Suntivich, K. J. May, H. A. Gasteiger, J. B. Goodenough, Y. Shao-Horn, A perovskite oxide optimized for oxygen evolution catalysis from molecular orbital principles, Science 334 (2011) 1383-1385.

[13] Y. Zhao, L. Xu, L. Mai, C. Han, Q. An, X. Xu, X. Liu, Q. Zhang, Hierarchical mesoporous perovskite $La_{0.5}Sr_{0.5}CoO_{2.91}$ nanowires with ultrahigh capacity for Li-air batteries, Proc. Natl. Acad. Sci. U.S.A. 109 (2012) 19569-19574.

[14] J. Suntivich, H. A. Gasteiger, N. Yabuuchi, H. Nakanishi, J. B. Goodenough, Y. Shao-Horn, Design principles for oxygen-reduction activity on perovskite oxide catalysts for fuel cells and metal-air batteries, Nat. Chem. 3 (2011) 546-550.

[15] Y. -W. Ju, S. Yoo, L. Guo, C. Kim, A. Inoishi, H. Y. Jeong, J. Shin, T. Ishihara, S. D. Yim, G. Kim,

Honeycomb-like perovskite oxide electrocatalyst for a hybrid Li-air battery, J. Electrochem. Soc. 162 (2015) A2651-A2655.

[16] C. Lim, A. Jun, H. Jo, K. M. Ok, J. Shin, Y. -W. Ju, G. Kim, Influence of Ca-doping in layered perovskite $PrBaCo_2O_{5+}$ on the phase transition and cathodic performance of a solid oxide fuel cell, J. Mater. Chem. A 4 (2016) 6479-6486.

[17] S. Choi, J. Shin, K. M. Ok, G. Kim, Chemical compatibility, redox behavior, and electrochemical performance of $Nd_{1-x}Sr_xCoO_{3-\delta}$ cathodes based on $Ce_{1.9}Gd_{0.1}O_{1.95}$ for intermediate-temperature solid oxide fuel cells, Electrochem. Acta 81 (2012) 217-223.

[18] S. Sengodan, S. Choi, A. Jun, T. H. Shin, Y. -W. Ju, H. Y. Jeong, J. Shin, J. T. S. Irvine, G. Kim, Layered oxygen-deficient double perovskite as an efficient and stable anode for direct hydrocarbon solid oxide fuel cells, Nat. Mater. 14 (2015) 205-209.

[19] S. Choi, S. Yoo, J. Kim, S. Park, A. Jun, S. Sengodan, J. Kim, J. Shin, H. Y. Jeong, Y. Choi, G. Kim, M. Liu, Highly efficient and robust cathode materials for low- temperature solid oxide fuel cells: $PrBa_{0.5}Sr_{0.5}Co_{2-x}Fe_xO_{5+}$, Sci. Rep. 3 (2013) 2426.

[20] D. -G. Lee, S. H. Kim, S. H. Joo, H. -I. Ji, H. Tavassol, Y. Jeon, S. Choi, M. -H. Lee, C. Kim, S. K. Kwak, G. Kim, H. -K. Song, Polypyrrole-assisted oxygen electrocatalysis on perovskite oxides, Energy Environ. Sci. 10 (2017) 523-527.

[21] A. K. Ganguli, T. Ahmad, S. Vaidya, J. Ahmed, Microemulsion route to the synthesis of nanoparticles, Pure Appl. Nanoparticles 80 (2008) 2451-2477.

[22] C. Chen, J. Cheng, S. Yu, L. Che, Z. Meng, Hydrothermal synthesis of perovskite bismuth ferrite crystallites, J. Cryst. Growth 291 (2006) 135-139.

[23] S. Nakayama, $LaFeO_3$ perovskite-type oxide prepared by oxide-mixing, co-precipitation, and complex synthesis methods, J. Mater. Sci. 36 (2001) 5643-5648.

[24] C. Kim, O. Gwon, I. Y. Jeon, Y. Kim, J. Shin, Y. -W. Ju, J. B. Baek, G. Kim, Cloud-like graphene nanoplatelets on $Nd_{0.5}Sr_{0.5}CoO_{3-\delta}$ nanorod as an efficient bifunctional electrocatalyst for hybrid Li-air batteries, J. Mater. Chem. A 4 (2016) 2022-2127.

[25] C. -H. Lu, H. -C. Wang, Reverse-microemulsion preparation and characterization of ultrafine

orthorhombic $LiMnO_2$ powders for lithium-ion secondary batteries, J. Eur. Ceram. Soc. 24 (2004) 206-214.

[26] A. J. Zarur, J. Y. Ying, Reverse microemulsion synthesis of nanostructured complex oxides for catalytic combustion, Nature 403 (2000) 65-67.

[27] M. H. Lee, S. G. Oh, S. C. Yi, D. S. Seo, J. P. Hong, C. O. Kim, Y. K. Yoo, J. S. Yoo, Characterization of Eu-doped Y_2O_3 nanoparticles prepared in nonionic reverse microemulsions in relation to their application for field emission display, J. Electrochem. Soc. 147 (2000) 3139-3142.

[28] C. Hwang, O. Gwon, H. Jo, K. M. Ok, G. Kim, Major role of surface area in perovskite electrocatalysts for alkaline systems, ChemSusChem 4 (2017) 468-471.

[29] A. Grimaud, K.J. May, C.E. Carlton, Y. Lee, M. Risch, W.T. Hong, J. Zhou, Y. ShaoHorn, Nat. Commun. 4 (2013) 2439.

[30] S. H. Wu, D. H. Chen, Synthesis of high-concentration Cu nanoparticles in aqueous CTAB solutions, J. Colloid Interface Sci. 273 (2004) 165-169.

[31] H. Watarai, Microemulsion capillary electrophoresis, Chem. Lett. 20 (1991) 391-394.

[32] S. Kim, S. Choi, A. Jun, J. Shin, G. Kim, Scale-down and Sr-doping effects on $La_4Ni_3O_{10-}$ - YSZ nanocomposite cathodes for IT-SOFCs, J. Electrochem. Soc. 161 (2014) F1468-F1473.

[33] G. LeoFanti, M. Padovan, G. Tozzola, B. Venturelli, Surface area and pore texture of catalysts, Catal. Today 41 (1998) 207-219.

[34] B. Liu, Y. Zhang, L. Tang, X-ray photoelectron spectroscopic studies of $Ba_{0.5}Sr_{0.5}Co_{0.8}Fe_{0.2}O_{3-}$ cathode for solid oxide fuel cells, Int. J. Hydrogen Energy 34 (2009) 435-439.

[35] J. Xu, P. Gao, T. S. Zhao, Non-precious Co_3O_4 nano-rod electrocatalyst for oxygen reduction reaction in anion-exchange membrane fuel cells, Energy Environ. Sci. 5 (2012) 5333-5339.

[36] N. A. Merino, B. P. barber, P. Eloy, L. E. Cadus, $La_{1-x}Ca_xCoO_3$ perovskite-type oxides: Identification of the surface oxygen species by XPS, Appl. Surf. Sci. 253 (2006) 1489-1493.

[37] J. -I. Jung, S. Park, M. -G. Kim, J. Cho, Tunable internal and surface structures of the bifunctional oxygen perovskite catalysts, Adv. Energy Mater. 5 (2015) 1501560

[38] X. Liu, W. Liu, M. Ko, M. Park, M. G. Kim, P. Oh, S. Chae, S. Park, A. Casimir, G. Wu, J. Cho,

Metal (Ni, Co)-metal oxides/graphene nanocomposites as multifunctional electrocatalysts, Adv. Funct. Mater. 25 (2015) 5799-5808.

[39] D. G. Lee, O. Gwon, H. -S. Park, S. H. Kim, J. Yang, S. K. Kwak, G. Kim, H. -K. Song, Conductivity-dependent completion of oxygen reduction ono catalysts, Angew. Chemie Int. Ed. 54 (2015) 15730-15733.

List of Publications

1. C. Lim, A. Jun, H. Jo, K. M. Ok, J. Shin, Y. -W. Ju*, and G. Kim*, Influence of Ca-doping in layered perovskite $PrBaCo_2O_{5+\delta}$ on the phase transition and cathodic performance of a solid oxide fuel cell, *J. Mater. Chem. A*, **4**, 2016, 6479-6486.

2. O. Kwon, S. Sengodan, C. Lim, H. Y. Jeong, J. Shin, Y. -W. Ju*, and G. Kim*, In Situ Surface Modification of Ni-YSZ with BaZrO3 for Enhancing the Sulfur Tolerance of Ni-YSZ Anode, *J. Electrochem. Soc.*, **163**, 2016, F1055-F1058.

3. C. Lim, C. Kim, O. Gwon, H. Y. Jeong, H. K. Song, Y. -W. Ju, J. Shin, and G. Kim*, Nano-perovskite oxide prepared via inverse microemulsion mediated synthesis for catalyst of lithium-air batteries, *Electrochim. Acta*, **275**, 2018, 248-255.

4. D. Jeong, J. Kim, O. Kwon, C. Lim, S. Sengodan*, J. Shin*, and G. Kim*, Scandium Doping Effect on a Layered Perovskite Cathode for Low-Temperature Solid Oxide Fuel Cells (LT-SOFCs), *Appl. Sci.*, **8**, 2018, 2217.

5. C. Lim, S. Sengodan, D. Jeong, J. Shin, and G. Kim*, Investigation of the Fe doping effect on the B-site of the layered perovskite $PrBa_{0.8}Ca_{0.2}Co_2O_{5+\delta}$ for a promising cathode material of the intermediate-temperature solid oxide fuel cells, *Int. J. Hydrogen and Energy*, **44**, 2019, 1088-1095.

6. H. Lee, O. Gwon, C. Lim, J. Kim, O. Galindev*, and G. Kim*, Advanced electrochemical properties of $PrBa_{0.5}Sr_{0.5}Co_{1.9}Ni_{0.1}O_{5+\delta}$ as a bifunctional catalyst for rechargeable zinc-air batteries, *ChemElectroChem,* **6**, 2019, 3154-3159.

Acknowledgments

I would like to express my gratitude to all of you who helped until I completed my dissertation through this acknowledgmetns. As a little sincerity, I would like to write down their names and remember the gratitude for a long time. First of all, I am proud and fortunate to express my deepest gratitude to my advisor, professor Guntae Kim, for giving me the opportunity to generous support, encouragement with patience, and guidance for my research work. Without his support, this dissertation would not have had the present quality and consistency.

Besides my advisor, I would like to thank all my committee members: Professor Jong-Beom Baek, Professor Hu Young Jeong, Professor Ikwhang Chang, and Professor Sihyuk Choi for very gracious and generous with their time, ideas, their encouragement, and insightful comments.

I thanks to our group members, who helped me during my doctoral course: Dr. Seonyoung Yoo, Prof. Sivaprakash Sengodan, Prof. Sihyuk Choi, Prof. Young-Wan Ju, Prof. Yunfei Bu, Dr. Aruem Jun, Dr. Junyoung Kim, Dr. Arunchander Asokan, Dr. Ohhun Gwon, Dr. Ohhun Kwon, Dr. Seona Kim, Dr. Changmin Kim, Donghwi Jeong, Sangwook Ju, Jeongwon Kim, Seungtae Lee, Hyunmin Kim, Hansol Lee, Arim Seong, Yejin Yang. Studying for years would have been impossible without them. I wish you all be the best for your work and would be always be happy.

And I wish to express deep thank and love to my family, friends, and my church people.